Development of high-performance, cost-effective quantum dot lasers for data-centre and Si photonics applications

Ying Lu

A thesis submitted to University College London for degree of

Doctor of Philosophy

Department of Electronic and Electrical Engineering

University College London

Sep 2022

Statement of originality

I, Ying Lu, confirm that the work presented in this thesis is my own. Where information has been derived from other sources, I confirm that this has been indicated in the thesis.

Signed:

_____

Date:

_____

Abstract

Photonic technologies have been considered new methods to achieve high bandwidth data communication and transmission. Si-photonics was proposed to address the discrepancy between bulky photonic devices and advanced electronics and create high-density integrated photonics. One of the challenges is integrating all the components necessary for full-functionality photonic integrated circuits (PIC). Great efforts have been devoted to overcoming the inherent limitations of Group-IV materials to provide sufficient gain, efficient modulation and sensitive detections. Making Si the host material for efficient light emission poses the most stringent requirements and is the primary missing component in the Si-photonics platform. Incorporating III-V materials with the Si photonics platform and quantum dot (QD) structure is a promising solution to the problem of a fully-integrated and high-functioning PIC.

High-performance QD lasers on III-V substrate or epitaxially on silicon have been developed in the last few decades with low threshold current density, low-temperature sensitivity, great reliability and large injection efficiency. Moreover, from the dynamic aspect, the intrinsic frequency of direct modulated laser and noise intensity is important for its applications in a data centre. QD is considered an alternative to quantum wells (QWs); however, the demonstrated QD laser has not fulfilled initial expectations, mainly due to its high gain compression and low differential gain. Another feature that needs to be noticed is feedback sensitivity, as the properties of semiconductor lasers are greatly degraded by reflection from external reflectors, such as the fibre connects and facets of integrated devices. QD devices are predicted to have stronger feedback resistance due to their large damping and small linewidth enhancement factor (LEF).

These properties have attracted much research, and high-performance QD devices have been developed. In this thesis, we comprehensively investigated QD laser performance and applied our QD laser in the optical module instead of the commercial QW distributed feedback (DFB) laser.

The background of Si photonics, the development of QD devices, and the fundamentals of QD lasers are presented in Chapter 1. The basic static and dynamic performances are demonstrated in Chapters 2 and 3. The GaAs-based QD laser provides a low threshold, high-temperature stability, and low noise operation with a limited small signal bandwidth. Chapter 4 provides a comprehensive study of the feedback resistance of the QD laser. The onset of coherence collapse is determined as -14 dB, verified by the static optical and electrical spectra and small signal response. Based on previous measurements, the QD laser is proven to be a high-performance, low-cost candidate for the Si-photonics module. In Chapter 5, the QD laser is used in practical applications, including a large signal transmission system with and without feedback and a commercial optical module. Although the intrinsic bandwidth of the QD laser is limited to around 5GHz due to the large damping and unoptimised capacitance, 30 Gbps data transmission has been demonstrated by a directly modulated QD laser. Large, high-speed signal modulation is achieved due to its high gain compression factor. Regarding the laser with intentional feedback, there is little degradation in the eye diagram under the whole feedback level up to -8dB. We also replaced the commercial QW DFB laser in 100G data-centre reach (DR)-1 optical module with our QD Fabry Perot (FP) laser without an isolator which gives a clear eye diagram under 53 Gbps 4-level pulse amplitude modulation (PAM4) with an extinction ratio (ER) of 4.7 dB.

In conclusion, this thesis verifies the feasibility of adopting the QD laser as a light source for the Si-photonics module. The QD laser is selected over other lasers because of its low threshold, high-temperature stability and maximum operating temperature, and strong tolerance to unintentional feedback. This is the first project to measure critical feedback levels with different characteristics and to theoretically analyse the inconsistent value. More importantly, this thesis' most original contribution is investigating the commercial applications of QD lasers in a Si-photonics module in an isolator-free state. In summary, the QD laser has been proven to be a feasible solution for the next-generation optical system.

Impact statement

Over the last half-century, the ever-growing increase in global internet traffic has imposed significant challenges on data centres. Extensive improvements have been demonstrated in the performance and functionality of Si microelectronics. The integration density of the logic transistor has increased exponentially, while the electrical connects do not scale at the same rate. Thus, optical interconnects are proposed as an alternative to traditional copper cabling. However, optical modules are usually bulky and expensive. Si photonics is proposed to address this problem and create large-scale photonic integrated circuits (PICs) utilising the existing mature complementary metal oxide semiconductor (CMOS) platforms.

Early studies have focused on passive devices, and recently, other components with full functionalities for PICs, including a light source, modulator, and detector, have been developed. Lasers have attracted the most attention due to their high requirements. The quantum dot (QD) laser is considered the most promising alternative to quantum well (QW) devices as the reduced quantum confined dimension provides the benefits of lower threshold current, high-temperature stability, less sensitivity to defects and smaller linewidth enhancement factor (LEF). The QD laser's dynamic performance and feedback tolerance need to be considered for further application and integration. Optical feedback from the external facets degrades the performance of devices and becomes the main obstacle, thwarting photonic integration. As fabricating optical isolators on chips remains extremely challenging and expensive, developing lasers with intrinsic insensitivity to feedback is an appealing solution.

This PhD research focuses on the comprehensive measurement of the GaAs-based QD laser, which is essential for applying QD lasers in Si-photonics modules. First, it researches its low threshold and high-temperature characteristics and the related properties of materials and devices. There is no doubt that the QD laser offers a stable and satisfying performance. More importantly,

the strong feedback tolerance of the QD laser is emphasised. The critical feedback level under statical operation and small signal modulation of 600 μm length QD laser are -14 dB, exceeding the feedback resistance of most QW counterparts. An even stronger tolerance of -8 dB is observed in more practical applications under large signal modulation. Together with the high gain compression factor, a Gbps feedback-resistant back-to-back operation under a feedback level of -8 dB is realised. Thus, a QD laser is a promising solution for most optical systems, with a reflection of around 13.2%. The most attractive finding of this thesis is the successful demonstration of the first isolator-free commercial QD laser-based Si-photonics 100G data-centre reach (DR1) module, which has commercial and industrial value.

Acknowledgements

The PhD studying period is really challenging and meaningful for me. It is impossible to achieve without the help from many people in both life and spirit. I would really appreciate them for their accompany and support.

Firstly, I would express my sincere thanks to my primary supervisor, Dr Siming Chen, for his guidance and encouragement. He is not only a great supervisor, but also an ambitious talent and a good friend. Wish him all the best henceforth. I also would thanks to my secondary supervisor Prof Huiyun Liu for his guidance and support from the beginning to the end of my study. It is really lucky for me to study at the MBE group and gain the systematic training from him. Their wisdom in both research and life affect inspired me a lot.

I would like to acknowledge my colleagues from the MBE group of UCL: Dr Mingchu Tang, Dr Jiang Wu, Dr Dongyoung Kim, Dr Jae-Seong Park, Mr Kevin Lee, Dr Hao Xu, Dr Mengya Liao, Dr Shun Chan, Dr Zizhuo Liu, Dr Junjie Yang, Dr Keshuang Li, Dr Xiao Li, Miss Shujie Pan, Miss Victoria Cao, Miss Hui Jia and Mr Huiwen Deng, for their great collaboration. I also would appreciate Prof Fengqi Liu, Dr Jingchuan Zhang, Mrs Ping Liang, Dr Zenghui Gu, Dr Huan Wang, Dr Chao Ning and Mr Yongqiang Sun for the help during my visit in Institute of Semiconductors CAS and Dr Xi Xiao,Dr Xiao Hu, Mr Jie Yan, Mr Dingyi Wu, and Mrs Jing Yang for hosting and assistance in NOEIC.

Moreover, I would express my gratitude for my friends Miss Lu Li, Miss Li Sun, Mr Bin Li, Mr Shengdi Liu, Mr Sunny Wang, Mr Qi Huang, Miss Tianyao Zhang, Mr GuoJian Chen, and sister-in-law Mrs Tingyu Luo. Thanks for your patience and care.

Finally, I would thank my family for their inclusive and trust in my whole life. No matter how depressed am I, no matter what a bad mood do I have, you are always by me side and there for me. You are the iron bastion inside my heart.

Content

List of abbreviations

AFM	atomic force microscope
APB	antiphase boundary
AR	anti-reflection
ASIC	application specific integrated circuit
BER	bit error rate
BH	buried heterostructure
CATV	community antenna television
CB	conduction band
CMOS	complementary metal-oxide-semiconductor
CW	continuous wave
CWDM	coarse wavelength division multiplexing
DBR	distributed Bragg reflector
DEQE	differential external quantum efficiency
DFB	distributed feedback
DFL	dislocation filter layer
DH	double heterostructure
DML	directly modulated laser
DR	data-centre reach
DUT	device under test
DWELL	dot-in-a-well
EA	electro-absorption

EAM	electro-absorption modulator
EBL	electron beam lithography
EO	electro-optic
EOM	electro-optic modulator
ER	extinction ratio
FP	Fabry-Perot
FWHM	full width at half maximum
HR	high reflection
ICP	inductive coupled plasma
IQE	internal quantum efficiency
IR	infrared
LEF	linewidth enhancement factor
LI	light current
LIV	light current voltage
MBE	molecular beam epitaxy
OMA	optical modulation amplitude
PIC	photonic integrated circuit
PL	photoluminescence
PSM	pulse slope modulation
QD	quantum dot
QCSE	quantum confined Stark effect
QSFP	quad small form-factor pluggable
QW	quantum well
RC	resistance capacitance
RIE	reactive ion etching
RIN	relative intensity noise
RF	radio frequency

SE	slope efficiency
SEM	scanning electron microscope
SK	Stranski-Krastanov
SNR	signal to noise ratio
SOI	silicon-on-insulator
TDECQ	transmitter and dispersion eye closure
UV	ultraviolet
VB	valence band
VI	voltage current
VOA	variable optical attenuator
WPE	wall plug efficiency

List of symbols

a	differential gain
a_0	nominal differential gain
α_H	linewidth enhancement factor
α_i	internal loss
α_{mir}	mirror loss
β	propagation constant
β_{sp}	spontaneous emission coupling rate
E_{conf}	confinement energy
ε	gain compression factor
f_{3dB}	3 dB bandwidth
f_{crit}	critical feedback level
f_R	resonance frequency
g	gain
g_{0N}	gain coefficient
G	modal gain
G_{gen}	generation term
γ	damping factor
γ_0	damping factor offset
η_d	differential external quantum efficiency
η_i	injection efficiency
η_{int}	internal quantum efficiency

I	injection current
I_{th}	threshold current
I_{tr}	transparency current
J_{th}	threshold current density
J_{tr}	transparency current density
K	k factor
κ	coupling rate of feedback light
L	length
λ	wavelength
m	mass
n	refractive index
N_e	carrier concentration
N_p	photon concentration
ν	frequency
$\Delta\nu$	linewidth
$\Delta\nu_{SE}$	linewidth due to spontaneous emission fluctuations
P_{out}	output power
Δp	uncertainty in momentum
R	reflectivity
R_{eff}	effective reflectivity
R_l	current leakage rate
R_{nr}	nonradiative recombination rate
R_{rec}	consumption term
R_{sp}	spontaneous emission rate
R_{st}	stimulated emission rate
T	temperature
T_0	characteristic temperature

τ	decay time
τ_{int}	round-trip time in lase cavity
τ_e	carrier lifetime
τ_e'	differential carrier lifetime
τ_{ext}	round-trip time in the external cavity
τ_p	photon lifetime
τ_p'	differential photon lifetime
Γ	confinement factor
v_g	group velocity
ν	frequency
V	volume of active region
V_e	volume of electrical mode
V_p	volume of optical mode
ω	angular frequency
ω_R	resonance angular frequency
Δx	confinement distance

List of figures

19

List of tables

List of publications

Journal of publications:

[1] Y. Lu, X. Hu, M. Tang, V. Cao, J. Yan, D. Wu, J. Park, H. Liu, X. Xiao and S. Chen. "Analysis of the regimes of feedback effects in quantum dot laser." Journal of Physics D

[2] Y, Lu., V. Cao, M. Liao, W. Li, M. Tang, A. Li, P. Smowton, A. Seeds, H. Liu and S. Chen (2020). "Electrically pumped continuous-wave O-band quantum-dot superluminescent diode on silicon." Optics Letters 45(19): 5468-5471.

[3] Li, K., J. Yang, Y. Lu, M. Tang, P. Jurczak, Z. Liu, X. Yu, J.-S. Park, H. Deng, H. Jia, M. Dang, A. M. Sanchez, R. Beanland, W. Li, X. Han, J.-C. Zhang, H. Wang, F. Liu, S. Chen, A. Seeds, P. Smowton and H. Liu (2020). "Inversion Boundary Annihilation in GaAs Monolithically Grown on On-Axis Silicon (001)." Advanced Optical Materials 8(22): 2000970.

[4] Liu, Z., C. Hantschmann, M. Tang, Y. Lu, J. Park, M. Liao, S. Pan, A. Sanchez, R. Beanland, M. Martin, T. Baron, S. Chen, A. Seeds, R. Penty, I. White and H. Liu (2020). "Origin of Defect Tolerance in InAs/GaAs Quantum Dot Lasers Grown on Silicon." Journal of Lightwave Technology 38(2): 240-248

[5] Pan, S., V. Cao, M. Liao, Y. Lu, Z. Liu, M. Tang, S. Chen, A. Seeds and H. Liu (2019). "Recent progress in epitaxial growth of III–V quantum-dot lasers on silicon substrate." Journal of Semiconductors 40(10): 101302.

[6] Zhou, T., M. Tang, G. Xiang, X. Fang, X. Liu, B. Xiang, S. Hark, M. Martin, M.-L. Touraton, T. Baron, Y. Lu, S. Chen, H. Liu and Z. Zhang (2019). "Ultra-low threshold InAs/GaAs quantum dot microdisk lasers on planar on-axis Si (001) substrates." Optica 6(4): 430-435.0

Conference publications:

[1] Xiang, G., M. Tang, T. Zhou, B. Xiang, S. Hark, M. Martin, T. Baron, Y. Lu, V. Cao, S.

Chen, H. Liu and Z. Zhang (2019). InAs/GaAs Quantum-Dot Photonic Crystal Bandedge Lasers Monolithically Grown on On-Axis Si (001) Substrates. 2019 Asia Communications and Photonics Conference (ACP).

[2] Dang, M., Z. Liu, Y. Lu, J.-S. Park, M. Liao, M. Tang, S. Chen and H. Liu (2019). Silicon-based III-V quantum-dot laser for silicon photonics. Asia Communications and Photonics Conference (ACPC) 2019, Chengdu, Optica Publishing Group.

[3] Deng, H., K. Li, M. Tang, J. Wu, M. Liao, Y. Lu, S. Pan, S. Chen, A. Seeds and H. Liu (2019). III-V Quantum Dot Lasers Monolithically Grown on Silicon. Optical Fiber Communication Conference (OFC) 2019, San Diego, California, Optica Publishing Group.

[4] Pan, S., M. Liao, Z. Liu, Y. Lu, V. Cao, M. Tang, J.-S. Park, J. Wu, S. Chen, A. Seeds and H. Liu (2018). O-band InAs Quantum Dot Light Sources Monolithically Grown on Si. CLEO Pacific Rim Conference 2018, Hong Kong, Optica Publishing Group

1 Introduction

Si photonics is a technique that manipulates light in the Si, which involves generating, routing, modulating, processing and detecting light. It brings advantages of integration and photonics and is now widely accepted as a key technology in next-generation communications systems and data interconnects. This section will first provide the background and challenges of electronics and discuss the benefits and motivations for photonic integrated circuits (PICs). Then, each component and integration technology of Si photonics will be covered. Afterwards, the basic theory of lasers and quantum dot (QD) will be discussed, emphasising the fundamentals of its strong feedback resistance. Finally, an outline of this thesis and its original contributions will be given.

1.1 Si photonics

Over the past few decades, Si has served as the foundation on which the multi-billion-dollar electronics industry has been built. The Si semiconductor device processing is considered a mature, low-cost, high-yield and robust process. Si is also a good optical material, with transparency in commercially important infrared (IR) wavelength bands, and is a suitable platform for large-scale PICs. Si-photonics attempts to leverage the maturity and know-how of Si complementary metal oxide semiconductor (CMOS) processing techniques and apply them to the realm of photonics and optoelectronics. In doing so, researchers hope to achieve an order-of-magnitude improvement in yield, cost, and time-to-market with less additional investment.

1.1.1 Background

The performance and functionality of Si microelectronics have been extensively improved while the integration density of the logic transistors has increased at an exponential pace from less than 200/mm^2 (Intel 4004 in 1971) to 100.8 million/mm^2 in Intel's 10 nm technology node [1]. Recently, Samsung Electronics planned to produce the 5 nm node [2], and IBM announced the world's first 2 nm node chip [3].
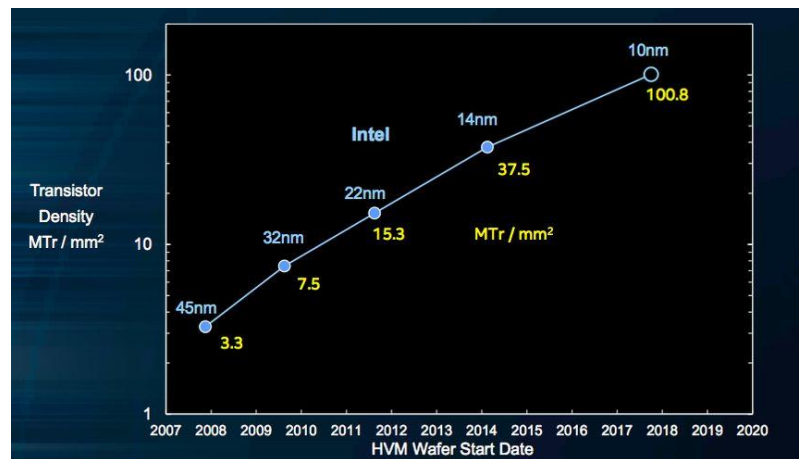
Figure 1.1: The development of logic transistor density for Intel [4].

From Figure 1.1, it can be seen that the transistor density jumped by a factor of 2.7 from the 14 nm to 10 nm node technique. Delivering more transistors in the same area means that the circuitry can be made smaller, saving costs. In addition, more functionalities can be added to a chip. Together with shrinking the components' dimensions, developing a manufacturing infrastructure capable of churning out wafers with a large diameter further lowers the cost of the electronic integrated circuits (EICs) [5]. This unprecedented level of commercial development revolutionised information technology on a global scale.

However, the electrical interconnect does not scale up at the same rate as the increased transistor density. Firstly, conventional electrical interconnections possess resistance which limits the rise time of signals and restricts the signal rate down the line. It is already the case for electrical transmission that the performance is dominated by the interconnection medium rather than the devices at either end. Optical interconnects show great promise because, at high data speeds, an optical channel has much lower loss and lower dispersion than copper traces. Additionally, optical

24

interconnection has the advantage of cost-efficiency. A typical optical fibre and coaxial cable cost $1 and $3 per meter, respectively [6]. Nowadays, optical links are used to connect racks of equipment that span 1-100 m and will continue to be adopted at distances of 1 m and below if the link power falls below 1 pJ/bit/m.

However, Si-based optical modules are usually bulky and expensive compared with versatile Si-based electronics. Over the last few decades, hundreds of billions of dollars have been invested in the electronics industry to scale Si chips' manufacturing capabilities. Photonics had no justification unless manufactured based on this existing, inexpensive, robust platform. To address the previous discrepancy, Si-photonics are proposed to create a large-scale PIC utilising mature CMOS platform space [7, 8]. Many breakthroughs have occurred over the past few years. Si-based devices' performance is advancing rapidly, including high-speed modulators and PDs, amplification and wavelength conversion at 40 Gbps in Si, and electrically pumped hybrid Si lasers. Although Si photonic-based optical interconnects show significant promise for low-cost bandwidth-scalable and high-volume manufacturability, this technology is not yet mature, and there are many challenges ahead. The development of Si photonics and details about each component are given in the following section.

1.1.2   Development of Si photonics

Si-photonics' roots can be traced back to pioneering studies of waveguides in silicon on insulator (SOI) wafer structures in 1985, and the early works were mostly stimulated by passive devices [9]. The cross-section of the Si-photonics waveguide is shown in the Figure 1.2 below. Owing to the high refractive index contrast between Si and SiO_2, planar waveguides with low scattering for a wide range of wavelengths from ultra-violet (UV) to IR can be achieved [10, 11]. Si waveguides' high refractive index contrast greatly enhances scattering loss at the core-cladding boundary.
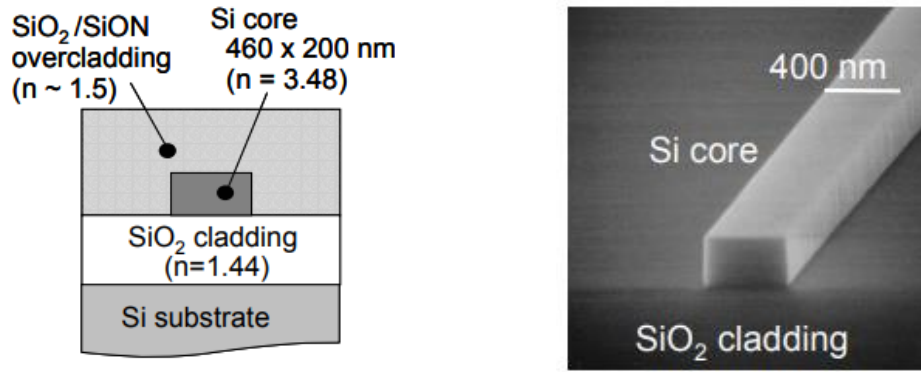
Figure 1.2: Si photonics wire waveguide (a) Shematic diagram and (b) scanning electron microscopy (SEM) figure [12].

Low propagation losses in waveguides and cavities are considered the most basic requirement for virtually all integrated optical devices. The typical loss of sub-micron Si waveguides is around 2 dB/cm. One can minimise the optical overlap with the boundary to achieve much lower loss or eliminate the etched sidewall by using selective oxidation to form the waveguide [13-15]. Both approaches have achieved Si waveguides with a loss of 0.1-0.5 dB/cm [7, 16, 17]. To further lower waveguide loss, one can use silica or SiN waveguide deposited on the Si substrate [18].

Small fibre-waveguide coupling loss is another requirement for creating efficient real-estate devices. Despite the severe modal mismatch, an enhanced coupling could be achieved using the inverse taper approach and surface gratings [19-22]. Other important passive device applications are the optical filters used for wavelength multiplexing and demultiplexing. The arrayed waveguide grating was demonstrated using SOI as early as 1997, while recently, the extinction ratio (ER) of the add-drop filter was improved to 50 dB with only 2 dB drop loss [23].

The practicality and promise of data communications advanced further with the realisation of modulators and photodetectors (PDs). An optical modulator that writes data onto an optical carrier constitutes an essential element in Si-photonics, decreasing the channel bandwidth limitations and reducing power consumption. Research into Si optical modulators dates back to the mid-1980s. The most common approach for commercialisation is the Mach-Zehnder modulator (MZM). This modulator is noted for its temperature insensitivity, high bandwidth and high-contrast optical transmission without deterioration due to spectral broadening and frequency chirping [24, 25]. Theoretically, Si is not an ideal material for modulators because of the inversion symmetry of a

non-strained Si crystal, which prohibits linear electro-optic (EO) effects [26, 27]. In Si MZMs, the modulation method relies on high-speed refractive index modulation via free carrier plasma dispersion, where changes in free electron and hole concentrations in the waveguide result in changes in the material's refractive index and absorption. However, MZMs tend to require a long interaction length of around millimetres which hinders higher-speed performance and results in greater insertion loss, power consumption and cost. Extensive work has also been done using ring resonators to modulate the light, providing lower power consumption, smaller footprints, and better modulation efficiency [28, 29]. These micro-ring modulators (MRMs) are also advantageous with multi-wavelength laser sources, which can help address scalability issues [29]. The challenges of Si MRM stem from its nonlinear effects and temperature sensitivity [30]. To further extend the bandwidth of optical modulators, heterogeneous integration can introduce other materials with strong EO effects to the Si platform, including SiGe [31], graphene[32], organics [28], III-V compounds [28] and lithium niobate [33, 34]. Thin-film lithium niobate on SOI waveguides has enabled over 100 Gbps modulators that are on par with state-of-the-art modulator performance using lithium niobate on insulators [35, 36]. Whilst impressive performances have been demonstrated in each case, a disadvantage is that CMOS compatibility and fabrication simplicity are compromised.

Alternatively, high-speed modulators can be achieved by III-V compound semiconductors, such as GaAs and InP, based on the electro-absorption (EA) [37, 38]. EA modulators generally offer low drive voltages (-2 V) and are cost-effective in volume production. Unfortunately, the indirect bandgap of Si makes it incredibly challenging to create an effective Si EA modulator. On the other hand, Ge exhibits comparable strong quantum-confined Stark effect (QCSE) and offers an alternative approach without heterogeneous modulator integration [39, 40].

A PD is another well-developed semiconductor device that converts an optical signal to an electrical signal, such as a voltage or current pulse. As a crucial optical building block in Si PICs, high-performance PDs are choired with high responsivity, low dark current, large bandwidth, and CMOS compatibility. Si is a rather poor optical absorber in the IR due to its low absorption coefficient in the wavelength range $\lambda > 1100\ nm$. The Figure 1.3 shows that the absorption coefficient depends on both the materials and light wavelength. III-V-based materials and Ge-on-Si are typically considered the solution for IR PD on Si for Si-photonics[41, 42].
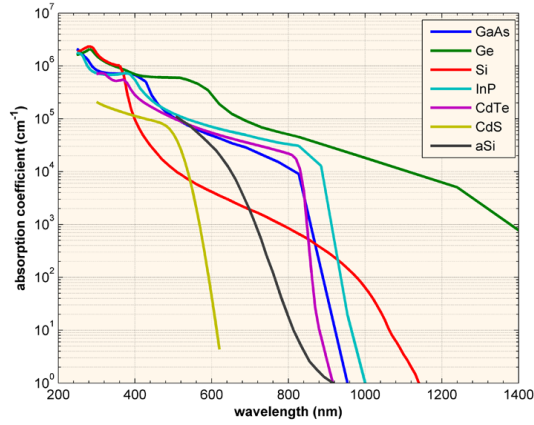
Figure 1.3:The absorption coefficient in various semiconductor at 300 K as a function of wavelength [43].

Waveguide PDs on Si broadly fall into two categories: Ge-based and hybrid III/V-silicon. Ge is an appealing absorbing material for use in silicon-based PICs because it can be integrated into a CMOS pilot line relatively easily (Si/Ge alloyed contacts are already used in CMOS electronics) and because the bulk material absorbs the entire 1310 nm window and much of the C and L bands. Comprehensive work has been conducted on the hetero-epitaxial Ge PD on the Si-photonics platform due to its strong linear absorption, high throughput and mature fabrication technology based on the CMOS pilot line [44-46]. The first comprehensive performance of practical Ge-PD was demonstrated in 2007 with an optical bandwidth of 31.3 GHz, 0.89 A/W responsivity and 169 nA dark current for 1550 nm [45]. More recently, an ultra-fast PD was demonstrated with optoelectrical bandwidth of 265 GHz and responsivity of 0.3 A/W, indicating the great potential of high-speed Ge-PD [47]. The waveguide-integrated efficient and high-speed CMOS-drivable PDs have been successfully commercially demonstrated with Ge-in-SOI.

Nowadays, most optical components based on IV materials, except light source, are well established in a single chip [48]. However, the inherent indirect bandgap properties of group IV materials hinder efficient photon generation of IV-based optical devices. A Si-based light source is the only missing component in Si-photonics and is considered the most explored component [49]. The III-V-based light sources have superior optical properties owing to the direct bandgap of III-V semiconductors and thus are incorporated in Si-photonics to overcome the inherent limitations of Si-based light sources. Then, the challenge became the monolithic growth of III-Vs on Si with a significant material dissimilarity. The mismatches in lattice constants and thermal expansion

coefficients induce high densities of crystalline defects, such as threading dislocations (TDs), and micro-cracks, which are detrimental to the device's performance.

Additionally, antiphase domain (APB) is formed in the epitaxy of polar semiconductors such as GaAs on nonpolar Si substrate. To fully realise the benefits of all epitaxial processes, the mismatch between several aspects of these semiconductor materials (lattice constants mismatch [50], thermal expansion coefficients mismatch [51], and APBs [52]) must be overcome. Fortunately, by using strained interlayers, thermal cycling, and dislocation filter layers (DFLs) [53-57], defects and cracks can be minimised by a few orders of magnitude, while the issue of APBs is eliminated through utilising miscut Si substrates[58]. Recently, devices with APB-free CMOS compatible on-axis Si have been developed through carefully optimised growth conditions, such as GaP/Si and GaAs-on-V-groove-Si templates or Si patterning [59-61].

QD lasers are regarded as an ideal light source for Si photonics [5]. Carrier confinement plays a pivotal role in the superior performance of self-assembled QD lasers [62-66]. Firstly, the QD structure offers the advantage of stronger tolerance to crystalline defects than quantum well (QW). As mentioned before, monolithic growth generates large amounts of dislocations which will act as non-radiative recombination centres. Each QD will trap carriers, thus effectively reducing sensitivity to the sidewall and defects-related non-radiative recombination [67]. Its insensitivity allows the fabrication of high-quality and long-lived (extrapolated lifetimes > 10 billion hours) QD lasers on Si despite the presence of many defects [68]. Secondly, as the density of states is further discretised, the subbands collapse into delta-function-like energy levels with atom-like degeneration, meaning that there will be less Fermi-level pinning at the band edge. Thus, it will be easier to achieve population inversion, and the threshold current density for the QD laser will be lower than its QW counterpart. Another significant merit of QD lasers is their high-temperature performance. The commercially available QD laser on the GaAs substrate operates up to 220 °C, while the QW laser can operate above 100 °C [69-71]. Temperature stability is highly desirable as it reduces the overhead needed to adjust laser drive currents due to temperature fluctuations on-chip. An infinite characteristic temperature was theorised and realised over a limited range of temperature due to the unfavourable offsets. The absolute temperature invariance can hardly be accomplished due to the small hole energy spacing in common InAs QD of only a few meV[72, 73]. Several techniques are used to increase the energy separation, including adjustments of the dot

size, composition and doping [74].

QD lasers also offer better dynamic properties than their QW counterparts regarding the linewidth and feedback sensitivity [75]. For QWs, the typical values of the linewidth enhancement factor (LEF) are 2-5, whereas, for QDs, a zero or even negative LEF is theoretically demonstrated, and a small value as low as 0.25 is derived from experimental measurements [65, 76, 77]. Lower LEF usually means narrower linewidth, lower noise, and higher feedback tolerance [78-80]. The low noise characteristic of QD lasers also originates from their higher damping rates and large K-factor (1 ns for QD while 0.265 ns for QW) [80, 81].

1.1.3   Si photonics module and integration

With each separate device well developed, the challenge became combining all the components with full functionality to form a small footprint and low-cost PICs. Integrated Si-photonics provides a pathway for all the key building blocks for communications and interconnects using optical channels. With more and more photonic devices integrated into a single chip, the PICs' complexity and functionalities have been greatly improved. The Figure 1.4 shows the number of photonic components integrated on a single waveguide over time for InP substrate with integrated lasers and Si substrate with and without integrated lasers. Si photonic integration is now catching up with InP-based III-V photonic integration, with over 4000 devices integrated in the large-scale silicon phase tuning array chip in 2013.
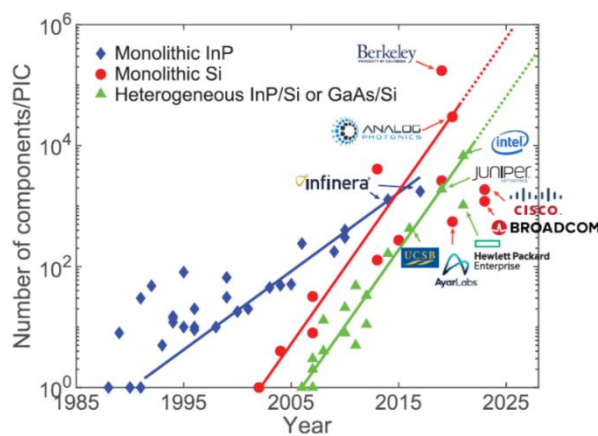
Figure 1.4. The number of photonic components integrated on a single waveguide over time for InP and Si substrate.

In particular, Si-photonics with fully integrated optics have been successfully deployed in 100 G pulsed slope modulation (PSM) and coarse wavelength division multiplexing (CWDM) quad small form-factor pluggable (QSFP). The $4\lambda \times 25$ Gbps CWDM4 transmitter is produced for datacentre applications, with heterogeneous integration of distributed feedback (DFB) lasers array, MZMs, and wavelength multiplexer [82]. The superior performance of the laser chip, up to 95 °C and the large bandwidth of the multiplexer contribute to the operation of the CWDM4 transmitter with low-intensity noise and a high side-mode-suppression ratio of up to 85 °C without temperature control. Datacentre networks are expected to scale from 100 G to 400 G. Several other multi-source agreements have been specified for the 400 G transceiver, depending on the link media and transmission distance[83]. In particular, the DR4 module with single-mode fibre packaged in a quad small form-factor pluggable direct detection (QSFP-DD) form has shown quite promising performance[84-86]. Real-time transmitter results, such as transmitter and dispersion eye closure, ER, optical modulation amplitudes and receiver sensitivity, are better than IEEE specifications.

The evolution of Si-photonics in the next decade will require implementing several new processes and packaging techniques. The Figure 1.5 shows the generational progression of optics and the co-packaging technologies used in a data centre. Over the last 20 years, the optical ports have been deployed as independent optical sub-systems physically plugged into a front panel of a host system which has been mass produced. However, as the density and speed of optical links increased manifold, the power and cost of the interconnect between electronics and optics have not scaled effectively.
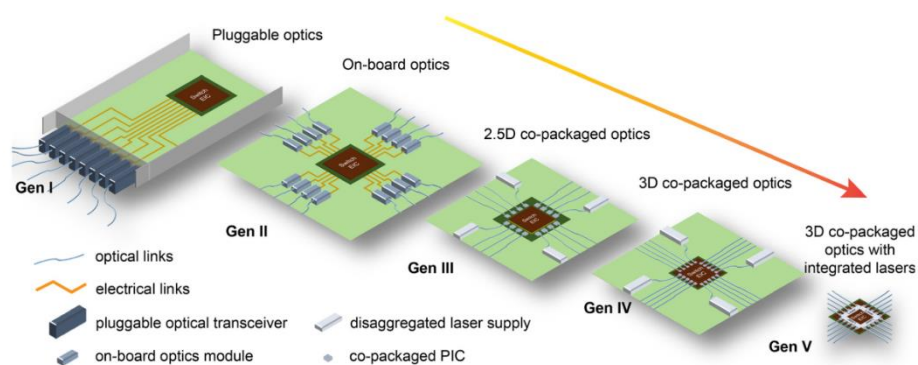
Figure 1.5. The generation of optics and corresponding evolution of co-packaging techniques [87].

There are some challenges in accomplishing a new paradigm of packaging optics directly with application-specific integrated circuits. First, optical components' physical area and volume are traditionally larger than could fit within a semiconductor package. Second, the reliability standard of co-packaged optics is expected to be consistent with core integrated circuit (IC). Finally, the optical fibre attached to a chip poses a unique challenge in optical components. Si photonics addresses these challenges based on its high-density, integrated solutions and direct connector to waveguides. Concurrently, PICs are evolving from pluggable transceivers at the board's periphery to co-packaged optics and electronics to 3D-integrated PICs and EICs.

1.2 Laser theory

A widely discussed challenge of Si-photonics is the lack of a monolithically integrated light source. To understand the EO transformation in lasers, we need to consider the generation of energy level electrons can occupy beforehand. When the distance between atoms is relatively large, the energy level distribution is only perturbed slightly by its neighbouring atoms, and its electron levels are thus discrete, similar to the isolated atom. The wave functions of the electrons will start to overlap as the spacing between atoms decreases. Due to the Pauli exclusive principle, the energy levels begin to split. In semiconductors, atoms are arranged in a crystal lattice. The number of neighbouring atoms increases, and the distance between them becomes quite small. Due to the enhanced splitting of energy levels, the valence band (VB) is simply the outermost electron orbital that electrons can occupy, while the next high-lying atomic level splits apart into the conduction band (CB). In semiconductors, the energy of the emitted photons should be exactly equal to the bandgap. Basically, there are three types of electron transition mechanisms: absorption, spontaneous recombination, and stimulated recombination.
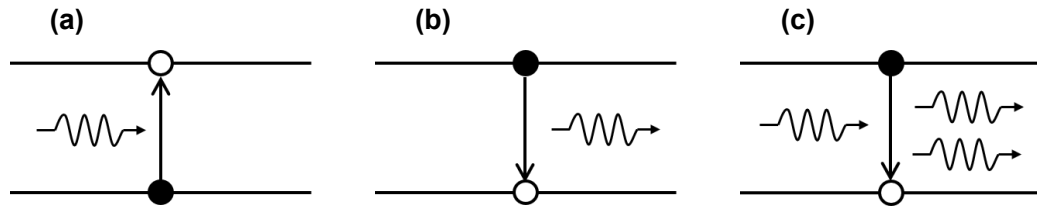
Figure 1.6 Electron transition between the CB and VB: (a) absorption, (b) spontaneous emission, and (c) stimulated emission. The solid circles represent electrons and the open circles represent holes

If the incident photon has an energy that coincides with the energy difference, $E_g = E_c - E_v$ (where E_c is the CB energy and E_v is the VB energy), the photon can be absorbed by the promotion of an electron to a higher energy level while leaving a hole in the VB, as shown in the Figure 1.6. However, the electrons excited to higher energy levels are unstable and will eventually relax to lower energy states in a certain lifetime. There are two processes to realise this relaxation: radiative and non-radiative recombination.

The spontaneous emission depicted in the figure shows a radiative recombination, in which an excited electron decays from CB to VB with a photon emission corresponding to E_g. The generated light by spontaneous emission is incoherent, as the photons are emitted in random directions. Another radiative emission process is stimulated emission. Unlike spontaneous emission, an existing photon initiates this radiative transition. As an incident photon perturbs the system, namely the excited electron, two photons with the same energy and the consistent direction of propagation with the incident photon are emitted.

The recombination between electrons and holes can also happen in non-radiative ways: recombination in non-radiative centres and Auger recombination. The basic radiative and non-radiative processes discussed here happen simultaneously in the semiconductor material. The lasing is initiated by the photons emitted through spontaneous emission. These generated photons are then further amplified through the stimulated emission. As the fundamental mechanism to generate a positive gain stimulated emission is the first necessary condition for lasers to operate. Non-radiative recombination and absorption are basically two mechanisms hindering the lasing, as non-radiative recombination contributes to the loss of carriers and absorption results in an optical loss. The optical gain generated by stimulated emission alone cannot accomplish the lasing. The absorption will dominate in thermal equilibrium, and the number of electrons that remain in lower

states far exceeds the holes. Population inversion is necessary to achieve the gain, in which the number of electrons in excited state (ES) is higher than in ground state (GS). Therefore, several pumping methods are developed to inject carriers in the active region and make the number of electrons in CB larger than in the VB. Once the electron in CB reaches a certain value, population inversion, the second necessity, could be realised.

By creating the population inversion in the gain medium, coherent light is initiated by spontaneous emission and amplified by stimulated recombination. The resonant cavity, which provides the optical feedback, is the last necessary ingredient of lasers. A portion of the light penetrates the facet and forms the output of the laser, while the rest of the light is reflected back to the cavity and further enhances the stimulated emission. Except for the multiple amplification, the resonant cavity also provides the mode selection mechanism, which will be discussed later. Three conditions compulsory for lasing are discussed above: stimulated emission, population inversion and resonant cavity.
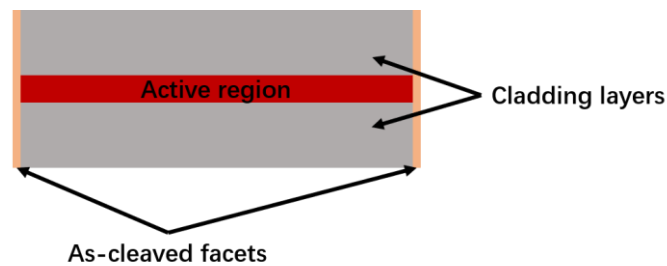
Figure 1.7: Schematic of Fabry-Perot FP cavity

As shown in the Figure 1.7, one of the most fundamental structures is the Fabry Perot (FP) cavity, in which the gain medium is placed inside the cavity with two cleaved facets as mirrors. The light of a range of wavelengths generated through spontaneous emission will bounce back and forth between the facets. However, only the wavelength that has undergone constructive interference is maintained in the cavity. The mode's amplitude and phase profiles should be maintained in a steady state after one closed loop path inside the resonator. For example, assume that the initial amplitude of the mode is A_0 and the constant propagation $\beta = 2n\pi v/c$, where n is the mode index, v is the frequency. In the one round trip process in the FP cavity with gain g and length L, the mode becomes,

$$A_0 R_1 R_2 \exp(2GL - 2\alpha_i L) \exp(i2\beta L) = A_1 \qquad \qquad \textit{Equation 1.1}$$

R_1 and R_2 are the facet reflectivity, depending on the coating conditions. The amplitude increases by $\exp(2GL)$ because of the gain and decreases by $R_1 R_2 \exp(2\alpha_i L)$ due to the internal loss α_i and reflection on the facets while its phase experiences a change of $\exp(i2\beta L)$.
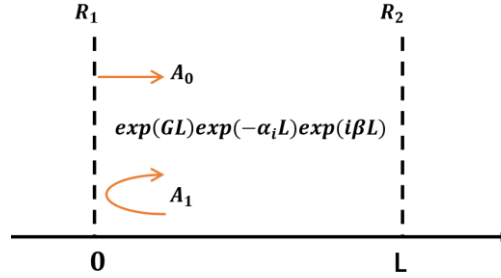
Figure 1.8: Transmission line section of length L.

By equating the gain and the frequency conditions on two sides, we obtain

$$G = \alpha_i + \frac{1}{2L} \ln \left(\frac{1}{R_1 R_2} \right) \qquad \qquad \textit{Equation 1.2}$$

$$v = \frac{mc}{2nL} \ (m \ is \ an \ integer) \qquad \qquad \textit{Equation 1.3}$$

From the results calculated above, the modal gain $(G = \Gamma g)$ equals the sum of total cavity loss, α_i and mirror loss $\alpha_m = \frac{1}{2L} \ln \left(\frac{1}{R_1 R_2} \right)$ at the threshold. Although the main carriers are confined in the active region, the field of the photons penetrates the cladding layers. Light will thus see additional optical losses during the propagation. The confinement factor Γ, defined as the volume overlap between the electrical mode and optical mode V_e/V_p, is employed when considering the entire optical gain.

As shown in the Equation 1.3, for resonance to occur, the phase shift of the longitudinal mode over a round trip should be equal to an integer multiple of 2π. The optical path determines the longitudinal mode, corresponding to the standing wave patterns confined in the FP cavity. Only the mode satisfying these two conditions could lase. The resultant lasing spectrum of the FP laser is shown below.
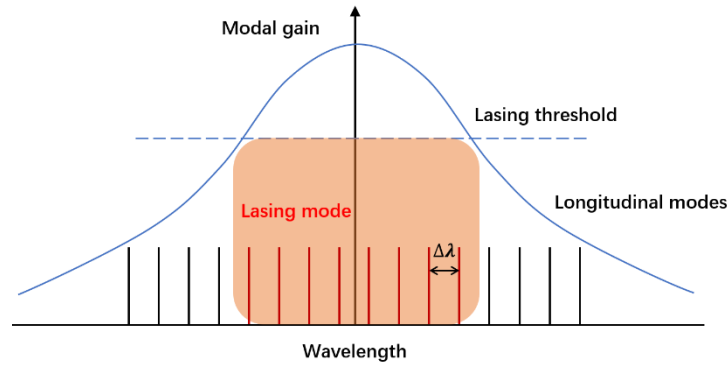
Figure 1.9: Schematic of gain and loss profiles in semiconductor lasers.

Generally, several longitudinal modes will simultaneously lase in the FP cavity, while the modes closest to the gain peak will dominate the lasing. During the transmission in optical fibres, the propagation speed of each mode is different as their refractive indexes depend on the wavelengths. Accordingly, the original optical pulses are broadened during transmission in the time domain. Multimode FP lasers can be used for simple applications, such as compact discs and short-haul communication systems. However, in long-haul, large-capacity optical fibre communication systems, the multimode nature of FP laser will limit system transmission performance. With higher modulation speed and longer transmission distance, the pulse spacing becomes shorter, and dispersion in fibre becomes more severe, making it difficult for a receiver to resolve sequentially transmitted optical pulses. 1.3 and 1.55 μm are often chosen as the wavelength window for optical communications to address the transmission challenge. The value of the attenuation of optical fibre greatly depends on its material and manufacturing tolerances. In fibre optics made of SiO_2, there are various resonant frequencies of glass relating to energies resonant with electron transition to a higher state and lattice vibration. Absorption of light around these resonances causes the refractive index to increase or decrease. As shown in the Figure 1.10, the refractive index reduces around the UV absorption tail and increases at the infrared absorption tail, and thus a resultant zero dispersion occurs at a wavelength of around 1.3 μm. The maxima of optical transparency of silica fibres occur at 1.3 and 1.55 μm.
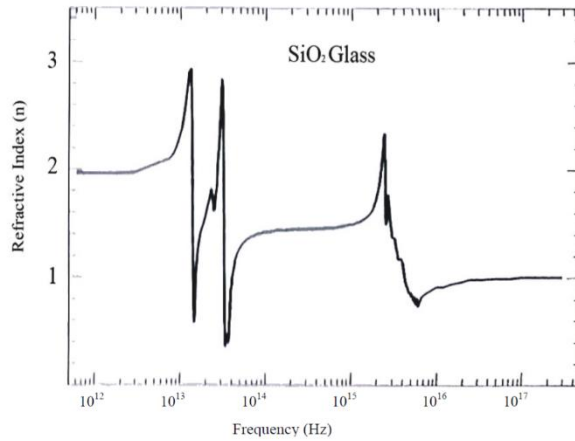
Figure 1.10: Real refractive index as a function of photon energy for Si0₂ fiber optic [88].

The major part of the optical link cost is the laser. Although operating at 1.55 μm provides the best performance, the 1.55 μm laser is usually employed only in longer link distances due to its high cost. For short links (up to 10 m) in the local area and enterprise optical network transmission, in which amplification is not necessary, the 1.3 μm laser is chosen due to its good performance and low cost.

III-V semiconductor lasers operating at these wavelengths have been developed since the 1980s, and nowadays, they are exclusively used in optical communication systems. Basically, the constituent elements and compositions determine the bandgap of semiconductor materials, namely the emission wavelength.
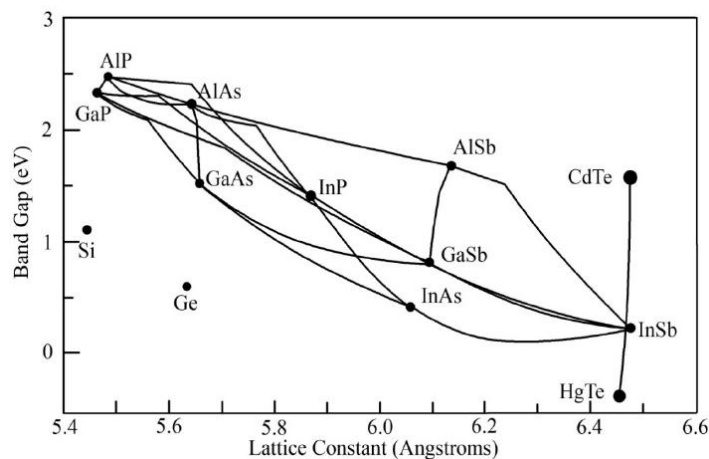
Figure 1.11: Plot of bandgap energies versus lattice parameters for selected III-V materials [89].

To realise the 1.3 μm wavelength emission, at least two compatible materials with same crystal structure and similar lattice constant must be found. It is required that the bandgap of the material

consisting of the active layer of semiconductor laser should correspond to the oscillation wavelength. Figure 1.11 plots the bandgap versus lattice constant for several families of III-V compounds. The combination of these compound semiconductors enables a wide range of emission from 0.7 to 1.6 μm. To maintain high crystal quality, the lattice mismatch between the lasing material and substrate should be less than <0.1%.

To realise the 1.3 μm wavelength emission, at least two compatible materials with the same crystal structure and similar lattice constant must be found. It is required that the bandgap of the material consisting of the active layer of the semiconductor laser should correspond to the oscillation wavelength. The figure below plots the bandgap versus lattice constant for several families of III-V compounds. The combination of these compound semiconductors enables a wide emission range from 0.7 to 1.6 μm. To maintain high crystal quality, the lattice mismatch between the lasing material and substrate should be less than <0.1%.

Typical compound semiconductors that meet these conditions for 1.3 and 1.55 μm are GaInAsP and AlGaInAs grown on the InP substrate [90]. However, the T_0 of conventional InGaAsP/InP lasers is typically low (between 50K and 70K) due to the small band offsets (1.34 eV for InP cladding and 0.95 eV for 1.3μm InGaAsP QW and the small difference in refractive indexes [91-93]. Temperature-insensitive characteristics are required to realise colourless, low-cost, low-power consumption optical interconnections. In this regard, using GaAs-based lasers has the potential advantage of realising a stable temperature operation in the 1.3μm range due to its large band offsets combined with the high optical confinement factor.

As shown in Figure 1.12, InGaAs ternary can be used to form 1.3 μm lasers. However, the growth of two-dimensional InGaAs QW is limited by the formation of dislocations and three-dimensional islands [94].
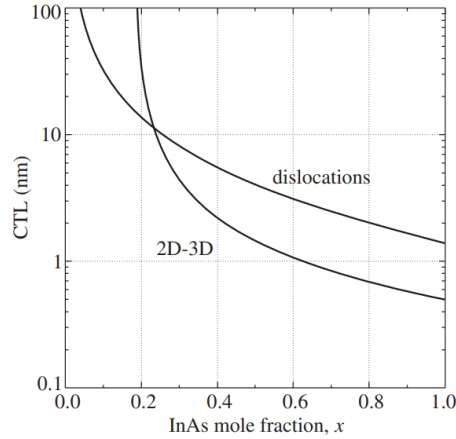
Figure 1.12: The relationship between the InAs mole fraction in In$_x$Ga$_{1-x}$As and critical thickness for the onset of dislocation and three-dimensional islands formation [95].

The emission wavelength boundary of QW is mainly limited by the fraction of the In content. However, a large mole fraction brings high dislocation density, leading to a three-island transition at a relatively small critical thickness. As a result, a pseudomorphic strained InGaAs QW is unlikely to achieve 1.3 μm emission. Alternatively, a plane of coherently strained QDs of InAs grown on GaAs substrates can provide 1.3 μm lasers on GaAs, as the island formation results in a redshift of the luminescence line [96, 97]. Nowadays, 1.3 μm InAs QD lasers can be grown using several techniques, particularly molecular beam epitaxyMBE, to form QDs with uniform size and high density [98-101].

1.3 Quantum dot lasers

It is pointed out that QD is an ideal light source for Si-photonics applications. This section provides a detailed analysis of the QD laser and its development. Carrier confinement within the active region is crucial for improving the performance of semiconductor devices. Initially, most common bulk-like materials were used with heterostructure layers. The carriers within the structure were only confined by the height of their band offset and could potentially have any energy within this band structure. Although the room temperature oscillation of the laser was achieved, as an increase in temperature and additional thermal energy $k_B T$ makes the emission energy higher than the expected bandgap energy, the output wavelength will shift, corresponding to the new photon energy $(E_g + k_B T)$, and thus the linewidth of the whole laser emission increases. Even worse,

an electron with energy higher than the band offset will escape from the confinement potential. In the early stage, double heterostructure (DH) was proposed, leading to the realisation of room-temperature laser oscillation [102, 103].

The quantum-structured laser's success with the active region's reduced dimensionality soon triggered much attention. Then, very thin layers called QW were utilised in the active region [104]. In quantum theory, due to uncertainty regarding its momentum (Δp) , the confinement energy(E_{conf}) of a confined particle increases with a reduced spatial confinement distance (Δx) [105]

$$E_{conf} = \frac{(\Delta p)^2}{2m^*} \sim \frac{\hbar^2}{2m^*(\Delta x)^2} \qquad \textit{Equation 1.4}$$

Considerable attention has been paid to the one-dimension confined structure, namely the QW lasers, with ultrathin active layers [106]. They have superior characteristics, such as extremely low threshold current, less temperature dependence, and a narrow gain spectrum [107-109]. The improved temperature stability made QW lasers a standard active layer employed in semiconductor lasers in the 1980s. Before QW became the typical structure of the active region, the innovation of QD as an extension of the conventional QW was theoretically proposed in 1982 [110]. This idea can be taken further if the confinement width in all 3 spatial directions is small enough (namely, several tens of nanometer-scale) to entirely confine the particle with its energy state.

$$E_{conf}(n_x, n_y, n_z) = \frac{\pi^2 \hbar^2}{2m} (\frac{n_x^2}{\Delta x^2} + \frac{n_y^2}{\Delta y^2} + \frac{n_z^2}{\Delta z^2}) \qquad \textit{Equation 1.5}$$

It can then be seen that, in quantum dot structure, the particle can have only discrete energies depending on n_x, n_y, n_z . The calculated density of states of materials with different carrier confinement dimensions is shown in Figure 1.13. The zero dimensionality of QDs leads to the presence of fully quantised discrete energy levels like an artificial atom, and the density of states is similar to the delta function at each allowed energy level [111, 112]. This merit, along with a further reduction in confined dimensionality and improved energetical distribution of carriers, makes QD lasers less temperature-sensitive than QW lasers.
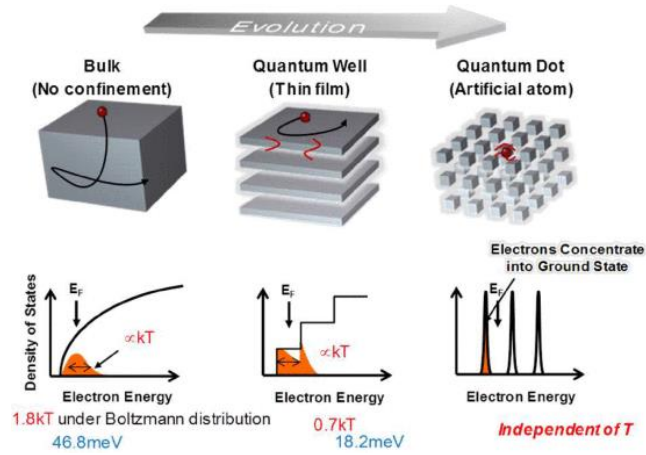
Figure 1.13: Evolution of semiconductor layers for light emission [111].

Theoretical predictions concerning the improved characteristics of QD are widely recognised, but the realisation of high-quality QDs has proven elusive in the initial stage. The first experimentally realised QD was fabricated by wet etching after the advantages of QDs had been recognised for over a decade [113]. Soon after, the fabrication methods of QDs, etching and regrowth techniques, gas phase nucleation, applying a strong magnetic field to QW systems and several other ex-situ processing techniques [114, 115]. Many of these suffer from a poor surface quality and nonuniformity. The advent of the self-organisation technique has opened an ideal way to realise QD lasers [116]. Based on the Stranski-Krastanov (SK) growth, highly uniform, high-density QDs can be achieved with high crystalline quality and without many dislocations [101].
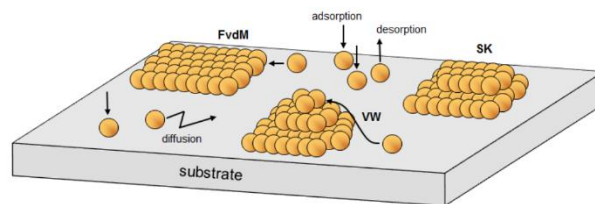
Figure 1.14: Schematic representation of three known film growth modes[117].

Three growth modes exist in the film epitaxial: Frank-van der Merwe (FM), SK, and Volmer-Weber (VW) growth modes are listed in the Figure 1.14, based on different interactions between materials. In the FM growth mode, there is a strong interaction between the depositing atoms and the substrate; thus, layer-by-layer growth is formed. VW growth of polycrystalline films involves the nucleation of 3D islands on a substrate surface and the impingement and coalescence of islands

to form continuous films. The SK growth mode is considered an intermediate combination of these two modes.

Two-dimensional planar growth is preferred in a few initial layers during the SK mode growth. The material is spontaneously re-distributed to relax the accumulated strain into a three-dimensional island after the deposited material exceeds a certain critical coverage and QDs become self-organised. Quantum-sized dots are obtained based on the 2D-3D growth mode transition. It is known that InAs QDs can be formed on GaAs. During the initial stage, when the growth of InAs is interrupted exactly at the onset of the 2D-3D transitions (about 1.8monolayers), 3D growth starts and dense InAs islands are formed. Uniform, high-density and high-quality crystalline QD was realised with the advent of the self-assembling technique, which contributes much to high-performance QD lasers [118, 119].

For lasers with QDs in the active region, theoretical calculations predict a high differential gain, an ultralow threshold current density and an ultrahigh temperature stability. Due to the size quantisation in QDs, the injected non-equilibrium carriers concentrate in a narrow energy band range near the band edge. The increase in the state's density leads to a much steeper dependence of optical gain on the injection current, and the deep confinement potentials lead to efficient GS emission [120-123]. All of these factors contribute to the lower threshold current density of the QD laser. In addition, due to the rapid filling of the charge carriers into the working states, population inversion is achieved with fewer injected carriers and, thus, lower transparency current density is realised. To this day, the threshold of QD lasers now approaches its theoretical limits and suppresses state-of-the-art QW lasers by improving the QD epitaxy layer quality together with the design of laser structures.

Another fundamental merit of the QD laser is its capacity to operate at high temperatures and temperature insensitivity [124, 125]. At relatively high temperatures, the temperature-dependent operation of lasers mainly originates from the parasitic transition of the thermally activated carriers [126]. As the dimension of confinement increases, the degree of freedom in the free-electron motion decreases, leading to a change in electrons' state density. The rate of the total spontaneous emission can be uniquely determined when the density of states and Fermi levels are given. It is derived that the analytical expressions of QD are independent of temperature. Such a feature could make QD laser commercially viable in a system operating over a large range of temperatures as, in

real applications, the surrounding ambient temperature is relatively high and unstable[127-129]. Additionally, a thermoelectric cooler is usually a prerequisite with relatively high-power consumption and a bulky power supply system to keep the active components within their operating temperature range.

Despite very high T_0 in QD lasers being expected in the early stage, QD devices still did not give the predicted temperature insensitivity. At relatively high temperatures, a significant amount of heat is generated at the junction, leading to a thermally activated carrier residing in layers adjacent to the active medium. The recombination of these thermally distributed electrons and holes does not primarily contribute to the lasing, giving rise to an increment in threshold current and reducing efficiency. Further possible improvements include increased optical gain through increasing the QD density, reducing the inhomogeneous broadening, improving the room temperature spontaneous emission efficiency and p-type modulation doping [130].

Defect tolerance is another pivotal superiority of QD over QW materials. In the epitaxial deposition between lattice-mismatched materials, the strain energy is built up and released by elastic relaxation [131-133]. Once up to a certain critical thickness, the introduction of dislocations is necessary to accommodate the structural mismatch [134]. This marks the plastic relaxation transformation, and several defects will be formed [135]. The threading dislocations caused by lattice mismatch act as non-radiative recombination and scattering centres, while macroscopic cracks originating from the thermal expansion mismatch limit heteroepitaxy films' thickness [136-138]. As growth proceeds, these defects eventually propagate upward and climb into the active zone. They can act as non-radiative recombination centres, reducing the photon emission efficiency and minority carrier lifetime [139]. Most early devices suffered from poor reliability and short lifetime, which impedes their practical applications [140-143].

To overcome this fundamental challenge, QDs are used as a gain material due to their inherent property of carrier confinement and reduced interaction with defects [144-146]. In principle, the strong Peach-Koehler strain field is introduced around the QD array, which can bend over the propagation of threading dislocations or propel them away from the QDs. Such bending increases the chance of destruction of the threading dislocation as they encounter or transport to the edge [147]. The self-organised QDs are assumed to be pyramidal in shape, as shown in Figure 1.15 (a). As the threading dislocations penetrate into the active region, their propagation is directed toward

the island's base [148, 149]. If the released strain energy exceeds the dislocation's energy, a segment of misfit dislocation will be generated and glides down into the dots. The dislocation under this area is bent.
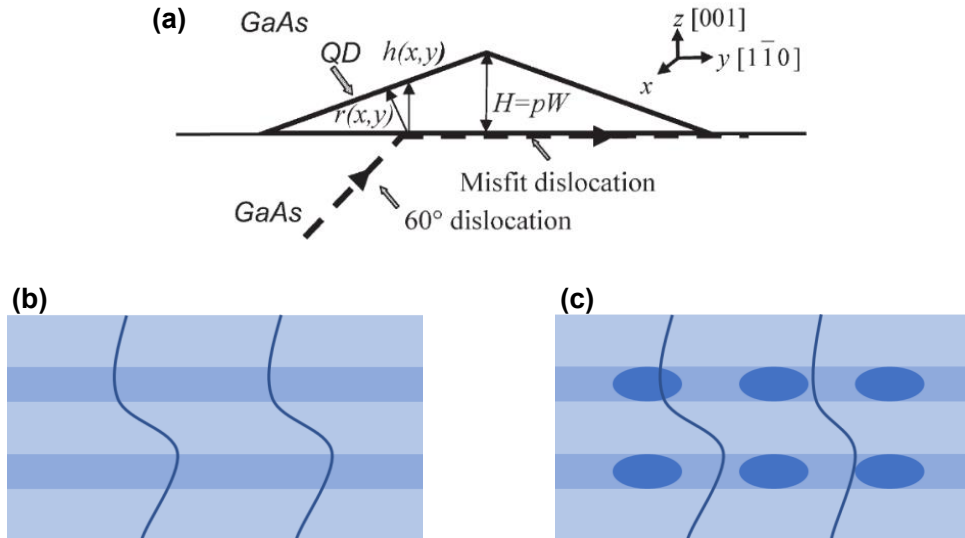
Figure 1.15: The mechanisms about the high defect tolerance of the QD laser. (a) Schematic of the cross-section of the dislocation by QD [150] and schematic of the interaction of TD between (b)QW and (c)QD.

In fact, self-organised QDs have been developed as dislocation filters for monolithic III-V/Si materials [150, 151]. It is also expected that multiple QD layers can achieve enhanced bending of the dislocations while the maximum layer numbers are limited by the kink generated in misfit loops[152]. Moreover, the very small ratio between the active dot and the total volume of the active region suggests that optoelectronic devices incorporating QDs could be more tolerant to defects. As shown in Figure 1.15 (b) and (c), one threading dislocation can damage the entire QW layers as it propagates through the active region, while, in QD lasers, it can only kill one or a very limited number of dots.

1.4 Optical feedback resistance of lasers

After briefly introducing the main advantages of the QD structure, we can identify another superiority, namely, its strong feedback tolerance. In an integrated photonic system, a portion of the output power is usually reflected back into the cavity from an external reflecting facet, such as

the fibre end and device facets. The weak external feedback can sometimes enhance the longitudinal mode selection and reduce the distortion in modulation [153-155]. However, the useful range of feedback effects is very narrow and restricted. In most general situations, serious problems arise from unintentional reflection, such as increased noise intensity and frequency and modulation degradation [156-159]. The inclusion of optical isolators is thus indispensable to blocking the reflections from each on-chip component and keeping the transmitter working in a stable condition and low noise state. However, the cost of an isolator is usually equivalent to or even higher than the laser chip itself [160]. Even worse, optical isolators are sometimes unavailable in specific circumstances. Until now, a suitable integrated isolator with strong isolation and negligible insertion loss has not been demonstrated. Therefore, an isolator-free transmitter with stable performance remains a major objective that could revolutionise the core technology of the physical layer.

In optical fibre communication systems, optical connectors act as a periodic reflector with a maximum value of as much as 13.2% [161]. Under such high-level feedback, the performance of the widely used QW lasers is severely destabilised. QD lasers demonstrate better performance mainly due to their symmetric gain curves and the resultant small coupling between phase and amplitude. Based on the extra insensitivity of the QD laser, it is possible to design directly modulated lasers that operate without an isolator.

The practical issue caused by facet reflection in the integrated circuits and metrics of the QD laser will be discussed in the following section. Firstly, it analyses and calculates the mechanism behind the fluctuation caused by feedback noise and the critical level. Then, it details the origin of the outstanding reflection resistance of QD material and its related physical parameters. Finally, it reviews the development of QD laser's improved feedback tolerance as it appears in the literature.

1.4.1   Critical feedback level

Optical feedback noise is generated when some light emitted from the cavity is unintentionally reflected back to the cavity due to external reflection [162]. When the optical field is perturbed with the light reflected back into the cavity, the carrier density and the gain profile will be affected

due to the fluctuation in photon density. As a result, various significant changes occur even with a minute fraction of reflection, including threshold current change, excess noise, linewidth broadening, high and low-frequency components of the intensity noise, un-damped relaxation in oscillation, or even a collapse of coherence accompanying an abrupt increase in noise and linewidth [163-168]. Even with a relatively low feedback ratio of -40 to -60 dB, the impact is noticeable, causing a drastic reduction in the coherence length of the laser, often termed as coherence collapse [169, 170].

Many researchers have provided a detailed understanding of the mechanism of the fluctuation [167, 171]. A multi-mirror cavity equivalent model is used to quantitatively analyse the effects of feedback noise. A laser plus the external reflected system is usually considered a compound cavity system. An effective mirror is used to fold the effects of mutual coupling between the laser cavity and external cavity through the partially transparent facets.
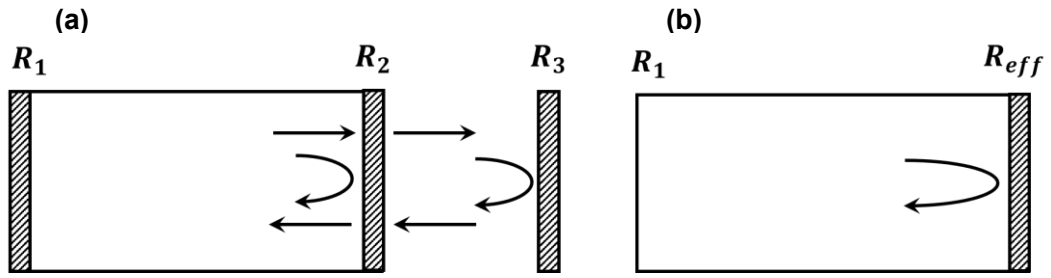
Figure 1.16: (a)Laser with external reflective facet. and (b) Equivalent model.

R_1, R_2 are the power reflectivities for the laser facets: R_3 denotes the reflectivity of the whole external cavity system, and $R_{eff} = |r_{eff}|^2$ is defined as the effective reflectivity of the whole external cavity system. Various factors intricately affect changes in the light output, including the distance between refractive objects and laser facets, the reflected ratio, and operating conditions.

$$r_{eff} = \frac{E_r}{E_i} = \sqrt{R_2}[1 + (1 - R_2)\sqrt{\frac{R_3}{R_2}}e^{-j\omega\tau_{ext}}] \qquad \text{Equation 1.6}$$

where ω is the angular frequency of the laser and τ_{ext} is the round-trip time in the external cavity. The change in effective reflectivity gives rise to a shift in the mirror loss and modifies the photon's lifetime. A further impact on the threshold gain and performance, such as threshold current

and spectrum distribution, is also introduced [172]. Regarding dynamic characteristics, according to the phase shift caused by the feedback, noise level and relaxation oscillation are altered [173, 174]. By considering the decay time, the coupling rate κ of feedback light is derived [175, 176].

$$\kappa = \frac{c}{2nL}(1 - R_2)\sqrt{\frac{R_3}{R_2}}$$ *Equation 1.7*

The numerical analysis of the effects of feedback noise is usually evaluated based on κ. Due to the high reflectivity and short cavity length of semiconductor lasers, the impact of the reflected light is usually severer in laser diodes than in lasers based on other materials. Another factor, LEF quantifying the coupling between amplitude and phase, affects the performance of diode lasers under external optical feedback, as semiconductor lasers with lower α_H are less sensitive to feedback noise. A parameter indicating the instrumental role of all the factors mentioned above due to external optical feedback is given below [177].

$$C = \kappa\tau_{ext}\sqrt{1 + \alpha_H^2}$$ *Equation 1.8*

Various regimes can be classified based on the C factor [169]. For the single-mode laser, in the region of $C < 1$, both line narrowing and broadening have been predicted and observed [178]. For $1 < C \leq 2$, mode hopping and hysteresis effects involving two external cavity modes were presented. In the range above 2, relaxation oscillation became undamped, giving rise to satellite and external-cavity peaks. Since the critical optical feedback condition often attracts more interest, the criterion for where the transition to coherence collapse can be expected is further derived. The feedback level is defined as the ratio between the power reflected into and out of the laser cavity. A general theoretical expression of the predicted coherence collapse level is

$$f_{crit} = \frac{\tau_L^2\Gamma^2 R(1 + \alpha_H^2)}{4(1 - R)^2\alpha_H^4}$$ *Equation 1.9*

This expression involves the damping rate Γ, LEF α, internal round-trip time τ_L, and facet reflectivity. Examining the equation, a higher damping factor, smaller LEF, longer cavity length and higher facet reflectivity lead to an increased critical level.

1.4.2 High feedback resistance of quantum dot laser

Among all the types of laser, QD lasers are predicted to have a low threshold and high-

temperature stability and show superior performance in optical feedback tolerance because of their large damping and small LEF. This section presents detailed theories on the impact factors of the parameters relevant to QD lasers' strong reflection resistance. Among various properties of QD lasers, LEF is regarded as a critical gain medium parameter that can distinguish their behaviour from other types of materials. Based on the Schawlow-Townes relation, it is predicted that the linewidth of the conventional laser is inversely proportional to power [179]. However, in semiconductor lasers, the measured width value decreases linearly with reciprocal mode power at a rate much greater than that predicted by the modified Schawlow-Townes formula,

$$\Delta v_{laser} = \frac{4\pi h v (\Delta v_0)^2}{P_{out}} \qquad \qquad \textit{Equation 1.10}$$

$$\Delta v_{laser}{}' = \frac{4\pi h v (\Delta v_0)^2}{P_{out}} (1 + \alpha_H^2) \qquad \textit{Equation 1.11}$$

$h v$ is the photon energy, Δv_0 is the resonator bandwidth and P_{out} is the output power.

For semiconductor lasers, any change in gain is accompanied by a corresponding change in its refractive index [180]. The coupling between the carrier-induced refractive index and intensity gain is described by the ratio of their derivative concerning carrier density and can be derived via the Kramers-Kronig relations. Generally, the broadened linewidth of the laser is thought to result from the phase fluctuations in the optical field. The linewidth broadening and further impact on the dynamical properties of semiconductor lasers due to the effect of the changed refractive index with carrier density can be quantitatively evaluated by the LEF [181]. The LEF serves as a key parameter in semiconductor materials as this factor not only determines the spectral linewidth and chirping but also affects the performance of feedback tolerance and high-speed modulations in lasers and amplifiers [182-184].

Typical values of LEF in QW lasers are around 2-5, causing a significant linewidth broadening and a weak feedback tolerance. By optimising the active region's composition and improving the waveguide design, a lower value of 0.5 can be achieved. A reduction in active region dimensionality from two-dimensional QW to zero-dimensional QD lasers is an effective way to reduce the LEF. In atom-like active regions, the carriers are confined in spatially separated potential dots, which localize both the variations in index and gain. Several models predict a near-zero LEF in QD material at its early stages [185, 186]. In addition, the symmetric gain spectrum in QD plays an important role in reducing the LEF. It is reported that a value as low as 0.1 is achieved in GaAs-

based QD devices, and even a negative value has been reported [187, 188]. The non-zero linewidth enhancement and shift of gain peak wavelength are a direct consequence of plasma, band filling, and many-body effects [185, 189], while the inhomogeneous size grown by the SK mechanism further broadened the gain spectrum and thus degraded the linewidth [190]. Since the critical coherence collapse feedback ratio is inversely proportional to the fourth power of the LEF, QD lasers have the potential for high external feedback resistance.

Another important parameter affecting the QD laser's feedback resistance is the damping factor. The high-relaxation oscillation damping rate caused by large gain compression is thought to originate in finite capture time from the wetting layer to the dots and the burning of the dot wetting layer's holes [191]. An increase in the relaxation oscillation damping will increase the threshold for instability. A sample with a LEF of 2 exhibited a highly suppressed relative intensity noise (RIN) peak and the critical level increased by as much as 15dB compared to the QW laser [192].

1.4.3   Literature review

The influences on the semiconductor laser properties of external optical feedback were examined as early as 1978 [157, 175]. Five distinct regimes of feedback effects were identified in 1986, depending on the optical feedback level and the distance to the reflection [165]. The feedback regimes defined the coherence collapse state, in which the optical power field's spectral density exhibits a very large broadening, which is particularly important since it is likely to be encountered in an optical communication system. It was observed that the transition to the coherence collapse occurs at optical feedback levels in the order of about 10^{-4} [177, 193]. Theoretical analysis can describe the stable region of the laser using small signal theory [172], RIN [194], rate equations [195] and nonlinear dynamics [174]. These numerical expressions and simulations for the critical feedback level were proposed and met with strong consensus. The phenomena occurring in semiconductor lasers due to optical feedback have been well studied, including variation of the threshold current as a function of feedback [196], mode-hopping [197], and chaotic behaviour [169].

The InAs/GaAs QD, laser feedback characteristics, were first reported with a threshold for coherence collapse of -8 dB [198]. This high reflection tolerance has been explained as a consequence of low value for LEF, a long laser cavity of 1.5 mm and a very high relaxation oscillation damping rate of 6 GHz caused by large gain compression. QD lasers on Si with high feedback tolerance are further demonstrated to meet techno-economic requirements of low cost, high device density and low power consumption for high-volume applications. The measurements of RIN versus various levels of optical reflection for QD laser epitaxially grown on Si were first carried out in 2017 [79]. A systematic comparison was made between monolithically grown 1.3 μm QD laser and heterogeneously integrated 1.55 μm QD lasers on Si regarding their RIN at a low frequency of around 100 MHz and a high frequency of up to 10 GHz. The results indicated that the QD laser showed 20 dB higher insensitivity than its QW counterpart.

Recently, a penalty-free operation with a QD laser on Si operating up to -7.4 dB optical feedback was performed at 10G Hz under external modulation [63]. Such remarkable resistance under modulation could definitely satisfy the maximum value of the optical feedback caused by the end-face reflection of as much as 13.2%. However, the circumstance becomes more complicated in the directly modulated laser and in most isolator-free applications, a major portion of the reflections comes from the facets or connectors outside of the transmitter, where the back-travelling modulated signal is the actual source of injection to the laser source. It was demonstrated in [160] that under 10 Gbps direct modulation speed, error-free back-to-back operation of QD laser was performed under up to -12 dB feedback level. The 20 km transmission was achieved under a maximum optical feedback level of -9 dB with a power penalty of less than 1d B at a bit error rate (BER) of 10^{-3}.

Several methods have been employed to promote feedback resistance, such as the corrugated waveguide and gain-coupling structures [199-201], to implement gain or loss coupling and take advantage of the consequential standing-wave effect. The 300 μm laterally loss-coupled QD DFB with absorptive metal gratings and high reflection was expected to improve tolerance with a -14 dB critical level and 2.5 Gbps modulation [198]. It has been suggested that the p-type doping technique can improve thermal resistance. It can lower the LEF and thus increase the critical feedback level. The comparison of tolerance to optical perturbations of epitaxial undoped and doped QD lasers was explored in [202, 203]. Based on the strong feedback tolerance of QD lasers,

optical transmitters for optical I/O cores using QD lasers without isolators were developed. The signal degradation by optical feedback reflected within the transmitter was negligible, and an error-free transmission was demonstrated at 25 Gbps with an estimated BER of less than 10^{-12} [204].

1.5 Objective and outline

This thesis aims to investigate the QD laser's basic static characteristics, dynamical performance, optical feedback performance and integration with the Si photonic module. The research is presented in six chapters, briefly described below.

In Chapter 1, the development of Si-photonics and related devices are briefly introduced. Then, the fundamental laser theories are shown. After that, the concept of QD and the advanced properties of the QD laser were discussed. At last, the fundaments of feedback sensitivity are given, and the development of the feedback-resistant laser is reviewed.

Chapter 2 presents the static results of the QD FP lasers. Before the data is presented, basic principles of the MBE, wafer characterisation and fabrication processes and facilities are introduced. Then the experimental setup is given. First, the basic light-current curves of different cavity-length QD lasers with identical wafers are measured. Based on these results, the related efficiencies and physical parameters are derived. The temperature characteristics of lasers with different cavity lengths are also provided. From these data, the design of the laser can be optimised based on the requirements of specific applications.

In Chapter 3, the measurement of the RIN of a 200 μm high-reflection coated laser is first demonstrated under different injection currents. The relevant parameters, such as the damping factor and D-value, are estimated. Then, a small signal modulation is posed on both 200 μm and 600 μm devices, followed by a large signal transmission performance.

Chapter 4 describes the feedback resistance of QD lasers. It was theoretically analysed that the feedback sensitivity relates to the intrinsic parameters of materials and the cavity and system structures. The experiments are divided into groups with various cavity lengths and injection currents. The static and dynamic properties with reflected light are presented and compared.

Based on previous results, QD laser shows an impressive performance in all aspects ranging

from static, dynamic, noise and feedback resistance. Chapter 5 evaluates practical applications regarding data transmission and optical modules. The eye diagrams under different large signal modulations are derived. A relatively high-quality 25 Gbps transmission is achieved under large optical feedback as high as -8 dB. Then the 1000 μm QD FP laser is adopted in the commercial Si photonics DR1 module instead of the QW DFB laser, and a comparative performance is achieved.

The first time using the QD laser was the light source in an isolator-free commercial Si-photonics module. The high performance of the QD laser is verified by its low threshold, high-temperature stability, low noise and strong reflection resistance. From an industrial view, QD material has the potential to be a low-cost solution without an isolator, controlling temperatures under quite a low injection current. The final chapter discusses the challenges in improving the performance of directly modulated light sources in Si photonics modules and co-packaging techniques.

1.6 Original of contributions

This thesis is a comprehensive study of the challenges and advantages of applying QD lasers in Si-photonics modules. Firstly, the QD sample was developed by my colleague Dr Mingchu Tang in the MBE group at UCL, while I conducted the related material characterisations myself. The fabrication processes were mainly carried out with the help of the engineers in LCN, while Dr Suguo Huo executed the dry etching due to its high requirements. Regarding the static characteristics, including length dependence and temperature variation LIV measurement, the related experiments were designed and performed by myself. For the RIN, small signal and large signal measurement, the tests were operated by engineers from NOEIC. The data test and the feedback sensitivity testbed were designed and constructed with help from NOEIC. The commercial module-based test was performed in the packaged test system and operated by Accelink Technologies Co., Ltd.

Reference

1. Max Roser, H.R., *Moore's Law Transistor Count 1970-2020*. 2020.
2. https://en.wikipedia.org/wiki/Moore%27s_law#cite_note-Samsung_5nm_in_2020-40. 2019.
3. https://spectrum.ieee.org/ibm-introduces-the-worlds-first-2nm-node-chip. 2021.
4. https://newsroom.intel.com/editorials/lets-clear-up-node-naming-mess/#gs.p1lvt5. 2017.
5. Norman, J.C., et al., *Perspective: The future of quantum dot photonic integrated circuits*. APL Photonics, 2018. **3**(3): p. 030901.
6. Meyer, M., *The compound semiconductor industry in the 1990s.* Compound Semiconductor, 1999. **5**(9): p. 26-28.
7. Li, G., et al., *Ultralow-loss, high-density SOI optical waveguide routing for macrochip interconnects.* Optics Express, 2012. **20**(11): p. 12035-12039.
8. Stanton, E.J., et al., *Multi-octave spectral beam combiner on ultra-broadband photonic integrated circuit platform.* Optics Express, 2015. **23**(9): p. 11272-11283.
9. Soref, R.A. and J.P. Lorenzo *Single-crystal silicon: a new material for 1.3 and 1.6 μm integrated-optical components.* Electronics Letters, 1985. **21**, 953-954.
10. Soref, R.A., S.J. Emelett, and W.R. Buchwald, *Silicon waveguided components for the long-wave infrared region.* Journal of Optics A: Pure and Applied Optics, 2006. **8**(10): p. 840-848.
11. Shen, L., et al., *Mid-infrared all-optical modulation in low-loss germanium-on-silicon waveguides.* Optics Letters, 2015. **40**(2): p. 268-271.
12. Yamada, K., et al. *All-Optical Wavelength Conversion using Silicon Photonic Wire Waveguide.* in *3rd IEEE International Conference on Group IV Photonics, 2006.* 2006.
13. Alduino, A. and M. Paniccia, *Interconnects: Wiring electronics with light.* Nature Photonics, 2007. **1**: p. 153-155.
14. Nezhad, M.P., et al., *Etch-free low loss silicon waveguides using hydrogen silsesquioxane oxidation masks.* Optics Express, 2011. **19**(20): p. 18827-18832.
15. Sparacin, D.K., S.J. Spector, and L.C. Kimerling, *Silicon waveguide sidewall smoothing by wet chemical oxidation.* Journal of Lightwave Technology, 2005. **23**(8): p. 2455-2461.
16. Dong, P., et al., *Low loss shallow-ridge silicon waveguides.* Optics Express, 2010. **18**(14): p. 14474-14479.
17. Fischer, U., et al., *0.1 dB/cm waveguide losses in single-mode SOI rib waveguides.* IEEE Photonics Technology Letters, 1996. **8**(5): p. 647-648.
18. Bauters, J.F., et al., *Planar waveguides with less than 0.1 dB/m propagation loss fabricated with wafer bonding.* Optics Express, 2011. **19**(24): p. 24090-24101.
19. Roelkens, G., et al., *Efficient fiber to SOI photonic wire coupler fabricated using standard CMOS technology.* 2005. 214-215.

20. Almeida, V., R. Panepucci, and M. Lipson, *Nanotaper for compact mode conversion.* Optics letters, 2003. **28**: p. 1302-4.

21. Narasimha, A., *Low dispersion, high spectral efficiency, RF photonic transmission systems and low loss grating couplers for silicon-on-insulator nanophotonic integrated circuits.* 2004: University of California, Los Angeles.

22. Taillaert, D., et al., *An out-of-plane grating coupler for efficient butt-coupling between compact planar waveguides and single-mode fibers.* IEEE Journal of Quantum Electronics, 2002. **38**(7): p. 949-955.

23. Popovic, M., et al., *Multistage high-order microring-resonator add-drop filters.* Optics letters, 2006. **31**: p. 2571-3.

24. Amiralizadeh, S., et al. *System Optimization of High-efficiency 400 Gb/s PAM4 Silicon Photonics Transmitter for Data Center Applications.* in *Optical Fiber Communication Conference (OFC) 2021.* 2021. Washington, DC: Optica Publishing Group.

25. Koyama, F. and K. Iga, *Frequency chirping in external modulators.* Journal of Lightwave Technology, 1988. **6**(1): p. 87-93.

26. Liu, A., et al., *A high-speed silicon optical modulator based on a metal–oxide–semiconductor capacitor.* Nature, 2004. **427**(6975): p. 615-618.

27. Soref, R. and B. Bennett, *Electrooptical effects in silicon.* IEEE Journal of Quantum Electronics, 1987. **23**(1): p. 123-129.

28. Koos, C., et al. *Terabit/s optical transmission using chip-scale frequency comb sources.* in *2014 The European Conference on Optical Communication (ECOC).* 2014.

29. Preston, K., et al. *Performance guidelines for WDM interconnects based on silicon microring resonators.* in *CLEO: 2011 - Laser Science to Photonic Applications.* 2011.

30. Li, H., et al., *A 3-D-integrated silicon photonic microring-based 112-Gb/s PAM-4 transmitter with nonlinear equalization and thermal control.* IEEE Journal of Solid-State Circuits, 2020. **56**(1): p. 19-29.

31. Feng, D., et al., *High speed GeSi electro-absorption modulator at 1550 nm wavelength on SOI waveguide.* Optics Express, 2012. **20**(20): p. 22224-22232.

32. Liu, M., et al., *A graphene-based broadband optical modulator.* Nature, 2011. **474**(7349): p. 64-67.

33. He, M., et al., *High-performance hybrid silicon and lithium niobate Mach–Zehnder modulators for 100 Gbit s^{-1} and beyond.* Nature Photonics, 2019. **13**(5): p. 359-364.

34. Wang, C., et al., *Integrated lithium niobate electro-optic modulators operating at CMOS-compatible voltages.* Nature, 2018. **562**(7725): p. 101-104.

35. Wang, C., et al., *Integrated lithium niobate electro-optic modulators operating at CMOS-compatible voltages.* Nature, 2018. **562**: p. 101-104.

36. He, M., et al. *High-Performance Hybrid Silicon and Lithium Niobate Mach-Zehnder Modulators.* in *2019 Asia Communications and Photonics Conference (ACP).* 2019.

37. Miller, D.A.B., et al., *Band-Edge Electroabsorption in Quantum Well Structures: The Quantum-Confined Stark Effect.* Physical Review Letters, 1984. **53**(22): p. 2173-2176.

38. Tang, Y., J.D. Peters, and J.E. Bowers, *Over 67 GHz bandwidth hybrid silicon electroabsorption modulator with asymmetric segmented electrode for 1.3 µm*

transmission. Optics Express, 2012. **20**(10): p. 11529-11535.

39.   Kuo, Y.-H., et al., *Strong quantum-confined Stark effect in germanium quantum-well structures on silicon.* Nature, 2005. **437**(7063): p. 1334-1336.

40.   Feng, D., et al., *High speed GeSi electro-absorption modulator at 1550 nm wavelength on SOI waveguide.* Optics express, 2012. **20**(20): p. 22224-22232.

41.   Kim, E.-T., et al., *High detectivity InAs quantum dot infrared photodetectors.* Applied Physics Letters, 2004. **84**(17): p. 3277-3279.

42.   Kim, S., et al., *Growth and characterization of InGaAs/InGaP quantum dots for midinfrared photoconductive detector.* Applied Physics Letters, 1998. **73**(7): p. 963-965.

43.   https://www.pveducation.org/pvcdrom/pn-junctions/absorption-coefficient.

44.   Vivien, L., et al., *Zero-bias 40Gbit/s germanium waveguide photodetector on silicon.* Optics Express, 2012. **20**(2): p. 1096-1101.

45.   Yin, T., et al., *31GHz Ge n-i-p waveguide photodetectors on Silicon-on-Insulator substrate.* Optics Express, 2007. **15**(21): p. 13965-13971.

46.   Chen, H., et al., *-1 V bias 67 GHz bandwidth Si-contacted germanium waveguide p-i-n photodetector for optical links at 56 Gbps and beyond.* Optics Express, 2016. **24**(5): p. 4622-4631.

47.   Lischke, S., et al., *Ultra-fast germanium photodiode with 3-dB bandwidth of 265 GHz.* Nature Photonics, 2021. **15**(12): p. 925-931.

48.   Lentine, A.L., et al., *Optoelectronic VLSI switching chip with greater than 1 Tbit/s potential optical I/O bandwidth.* Electronics Letters, 1997. **33**(10): p. 894.

49.   Camacho-Aguilera, R.E., et al., *An electrically pumped germanium laser.* Optics Express, 2012. **20**(10): p. 11316-11320.

50.   Liu, A.Y., et al., *Reliability of InAs/GaAs Quantum Dot Lasers Epitaxially Grown on Silicon.* IEEE Journal of Selected Topics in Quantum Electronics, 2015. **21**(6): p. 690-697.

51.   Grenning, D.A. and A.H. Herzog, *Dislocations and their Relation to Irregularities in Zinc-Diffused GaAsP p-n Junctions.* Journal of Applied Physics, 1968. **39**(6): p. 2783-2790.

52.   Chu, S.N.G., et al., *Antiphase domains in GaAs grown by metalorganic chemical vapor deposition on silicon-on-insulator.* Journal of Applied Physics, 1988. **64**(6): p. 2981-2989.

53.   Tang, M., et al., *Optimizations of Defect Filter Layers for 1.3-μm InAs/GaAs Quantum-Dot Lasers Monolithically Grown on Si Substrates.* IEEE Journal of Selected Topics in Quantum Electronics, 2016. **22**(6): p. 50-56.

54.   Tachikawa, M. and M. Yamaguchi, *Film thickness dependence of dislocation density reduction in GaAs-on-Si substrates.* Applied Physics Letters, 1990. **56**(5): p. 484-486.

55.   Matthews, J.W. and E. Klokholm, *Fracture of brittle epitaxial films under the influence of misfit stress.* Materials Research Bulletin, 1972. **7**(3): p. 213-221.

56.   Bolkhovityanov, Y.B. and O.P. Pchelyakov, *GaAs epitaxy on Si substrates: modern status of research and engineering.* Physics-Uspekhi, 2008. **51**(5): p. 437-456.

57.   Hull, R., et al., *Role of strained layer superlattices in misfit dislocation reduction in growth of epitaxial $Ge_{0.5}Si_{0.5}$ alloys on Si(100) substrates.* Journal of Applied Physics, 1989. **65**(12): p. 4723-4729.

58. Jung, D., et al., *Low threading dislocation density GaAs growth on on-axis GaP/Si (001).* Journal of Applied Physics, 2017. **122**(22): p. 225703.

59. Kwoen, J., et al., *All MBE grown InAs/GaAs quantum dot lasers on on-axis Si (001).* Optics Express, 2018. **26**(9): p. 11568-11576.

60. Alcotte, R., et al., *Epitaxial growth of antiphase boundary free GaAs layer on 300 mm Si(001) substrate by metalorganic chemical vapour deposition with high mobility.* APL Materials, 2016. **4**(4): p. 046101.

61. Li, Q., K.W. Ng, and K.M. Lau, *Growing antiphase-domain-free GaAs thin films out of highly ordered planar nanowire arrays on exact (001) silicon.* Applied Physics Letters, 2015. **106**(7): p. 072105.

62. Gupta, N., et al., *Temperature-Independent Performance of an 8-Layer λ ~1.3 μm InAs/GaAs Quantum-Dot Laser.* Journal of Russian Laser Research, 2020. **41**(1): p. 86-93.

63. Duan, J., et al., *1.3 μm Reflection Insensitive InAs/GaAs Quantum Dot Lasers Directly Grown on Silicon.* IEEE Photonics Technology Letters, 2019. **31**(5): p. 345-348.

64. Zhang, Z., et al., *Effects of modulation p doping in InAs quantum dot lasers on silicon.* Applied Physics Letters, 2018. **113**(6): p. 061105.

65. Jung, D., et al., *High efficiency low threshold current 1.3 μm InAs quantum dot lasers on on-axis (001) GaP/Si.* Applied Physics Letters, 2017. **111**(12): p. 122107.

66. Chen, S., et al., *Electrically pumped continuous-wave 1.3 μm InAs/GaAs quantum dot lasers monolithically grown on on-axis Si (001) substrates.* Optics Express, 2017. **25**(5): p. 4632-4639.

67. Liu, Z., et al., *Origin of Defect Tolerance in InAs/GaAs Quantum Dot Lasers Grown on Silicon.* Journal of Lightwave Technology, 2020. **38**(2): p. 240-248.

68. Jung, D., et al., *Highly Reliable Low-Threshold InAs Quantum Dot Lasers on On-Axis (001) Si with 87% Injection Efficiency.* ACS Photonics, 2018. **5**(3): p. 1094-1100.

69. Kageyama, T., et al., *Long-wavelength quantum dot FP and DFB lasers for high temperature applications.* SPIE OPTO. Vol. 8277. 2012: SPIE.

70. Urino, Y., et al., *First Demonstration of Athermal Silicon Optical Interposers With Quantum Dot Lasers Operating up to 125 °C.* Journal of Lightwave Technology, 2015. **33**(6): p. 1223-1229.

71. Kurczveil, G., et al., *Robust hybrid quantum dot laser for integrated silicon photonics.* Optics Express, 2016. **24**(14): p. 16167-16174.

72. Kageyama, T., et al. *Extremely high temperature (220°C) continuous-wave operation of 1300-nm-range quantum-dot lasers.* in *2011 Conference on Lasers and Electro-Optics Europe and 12th European Quantum Electronics Conference (CLEO EUROPE/EQEC).* 2011.

73. Tong, C.Z., et al., *Rate Equations for 1.3μm Dots-Under-a-Well and Dots-in-a-Well Self-Assembled InAs–GaAs Quantum-Dot Lasers.* IEEE Journal of Quantum Electronics, 2006. **42**(11): p. 1175-1183.

74. Shchekin, O.B., et al., *Discrete energy level separation and the threshold temperature dependence of quantum dot lasers.* Applied Physics Letters, 2000. **77**(4): p. 466-468.

75. Chow, W.W. and F. Jahnke, *On the physics of semiconductor quantum dots for*

applications in lasers and quantum optics. Progress in Quantum Electronics, 2013. **37**(3): p. 109-184.

76.   Kondratko, P.K., et al., *Observations of near-zero linewidth enhancement factor in a quantum-well coupled quantum-dot laser.* Applied Physics Letters, 2003. **83**(23): p. 4818-4820.

77.   Bhowmick, S., et al., *High Performance InAs/In$_{0.53}$Ga$_{0.23}$Al$_{0.24}$As /InP Quantum Dot 1.55μm Tunnel Injection Laser.* IEEE Journal of Quantum Electronics, 2014. **50**(1): p. 7-14.

78.   O, D., et al. *Feedback sensitivity of 1.3 μm InAs/GaAs quantum dot lasers.* Electronics Letters, 2003. **39**, 1819-1820.

79.   Liu, A.Y., et al., *Reflection sensitivity of 1.3μm quantum dot lasers epitaxially grown on silicon.* Optics Express, 2017. **25**(9): p. 9535-9543.

80.   Urino, Y., et al. *High-density Optical Interconnects with Integrated Quantum Dot Lasers.* in *Advanced Photonics 2016 (IPR, NOMA, Sensors, Networks, SPPCom, SOF).* 2016. Vancouver: Optica Publishing Group.

81.   Zhukov, A.E., M.V. Maksimov, and A.R. Kovsh, *Device characteristics of long-wavelength lasers based on self-organized quantum dots.* Semiconductors, 2012. **46**(10): p. 1225-1250.

82.   Yu, H., et al. *100Gbps CWDM4 Silicon Photonics Transmitter for 5G Applications.* in *2019 Optical Fiber Communications Conference and Exhibition (OFC).* 2019.

83.   802.3bm, I. *400 Gb/s over Multimode Fiber Task Force.* Available from: http://www.ieee802.org/3/cm/.

84.   Dong, P., et al., *Four-channel 100-Gb/s per channel discrete multitone modulation using silicon photonic integrated circuits.* Journal of Lightwave Technology, 2016. **34**(1): p. 79-84.

85.   *The QSFP-DD Multi-Source Agreement,* . Available from: www.qsfp-dd.com.

86.   Xie, C., et al. *Real-Time Demonstration of Silicon-Photonics-Based QSFP-DD 400GBASE-DR4 Transceivers for Datacenter Applications.* in *2020 Optical Fiber Communications Conference and Exhibition (OFC).* 2020.

87.   Margalit, N., et al., *Perspective on the future of silicon photonics and electronics.* Applied Physics Letters, 2021. **118**(22): p. 220501.

88.   Alterovitz, S.A., et al., in *Handbook of Optical Constants of Solids*, E.D. Palik, Editor. 1998, Academic Press: Boston.

89.   Downs, C. and T. Vandervelde, *Progress in Infrared Photodetectors Since 2000.* Sensors (Basel, Switzerland), 2013. **13**.

90.   Katsuyama, T., *Development of semiconductor laser for optical communication.* SEI Technical Review, 2009: p. 13-20.

91.   Agrawal, G.P., *Fiber-Optic Communication Systems.* 2012: Wiley.

92.   Takemasa, K., et al. *High-temperature operation of 1.3 μm AlGaInAs strained multiple quantum well lasers.* Electronics Letters, 1998. **34**, 1231-1233.

93.   Ishikawa, T., et al., *Well-thickness dependence of high-temperature characteristics in 1.3-μm AlGaInAs-InP strained-multiple-quantum-well lasers.*

94.   Kondow, M., et al., *GaInNAs: A Novel Material for Long-Wavelength-Range Laser Diodes with Excellent High-Temperature Performance.* Japanese Journal of Applied Physics, 1996. **35**(Part 1, No. 2B): p. 1273-1275.

95.   Ustinov, V.M. and A.E. Zhukov, *GaAs-based long-wavelength lasers.* Semiconductor Science and Technology, 2000. **15**(8): p. R41-R54.

96.   Mirin, R.P., et al., *1.3 μm photoluminescence from InGaAs quantum dots on GaAs.* Applied Physics Letters, 1995. **67**(25): p. 3795-3797.

97.   Ustinov, V.M. and A.E. Zhukov, *GaAs-based long-wavelength lasers.*

98.   Ledentsov, N.N., et al., *Direct formation of vertically coupled quantum dots in Stranski-Krastanow growth.* Physical Review B, 1996. **54**(12): p. 8743-8750.

99.   Schmidt, O.G., et al., *Prevention of gain saturation by multi-layer quantum dot lasers.* Electronics Letters, 1996. **32**: p. 1302-1304.

100.   Heinrichsdorff, F., et al., *Self-organization processes of InGaAs/GaAs quantum dots grown by metalorganic chemical vapor deposition.* Applied Physics Letters, 1996. **68**(23): p. 3284-3286.

101.   Leonard, D., et al., *Direct formation of quantum-sized dots from uniform coherent islands of InGaAs on GaAs surfaces.* Applied Physics Letters, 1993. **63**(23): p. 3203-3205.

102.   Hsieh, J.J., J.A. Rossi, and J.P. Donnelly, *Room-temperature cw operation of GaInAsP/InP double-heterostructure diode lasers emitting at 1.1 μ m.* Applied Physics Letters, 1976. **28**(12): p. 709-711.

103.   Panish, M.B., I. Hayashi, and S. Sumski, *Double-heterostructure injection lasers with room-temperature threshold as low as 2300 A/cm^2.* Applied Physics Letters, 1970. **16**(8): p. 326-327.

104.   Dingle, R., W. Wiegmann, and C.H. Henry, *Quantum States of Confined Carriers in Very Thin Al$_x$Ga$_{1-x}$As-GaAs-Al$_x$Ga$_{1-x}$As Heterostructures.* Physical Review Letters, 1974. **33**(14): p. 827-830.

105.   Griffiths, D.J. and D.F. Schroeter, *Introduction to Quantum Mechanics.* 3 ed. 2018, Cambridge: Cambridge University Press.

106.   Holonyak, N., et al., *Quantum-well heterostructure lasers.* IEEE Journal of Quantum Electronics, 1980. **16**(2): p. 170-186.

107.   Burnham, R.D., et al. *Low-threshold single quantum well (60 Å) GaAlAs lasers grown by MO-CVD with Mg as p-type dopant.* Electronics Letters, 1982. **18**, 1095-1097.

108.   Iwamura, H., et al. *Dynamic behaviour of a GaAs-AlGaAs MQW laser diode.* Electronics Letters, 1983. **19**, 180-181.

109.   Chin, R., et al., *Temperature dependence of threshold current for quantum-well AlxGa1−xAs-GaAs heterostructure laser diodes.* Applied Physics Letters, 1980. **36**(1): p. 19-21.

110.   Arakawa and Y., *Multidimensional quantum well laser and temperature dependence of its threshold current.* Applied Physics Letters, 1982. **40**(11): p. 939-941.

111.   Nishi, K., et al., *Development of Quantum Dot Lasers for Data-Com and Silicon Photonics Applications.* IEEE Journal of Selected Topics in Quantum Electronics, 2017. **23**(6): p. 1-7.

112.   Fox, A.M. and D.P.A.M. Fox, *Optical Properties of Solids.* 2001: Oxford University Press.

113.   Hirayama, H., et al. *Lasing action of Ga$_{0.67}$In$_{0.33}$As/GaInAsP/InP tensile-strained*

quantum-box laser. Electronics Letters, 1994. **30**, 142-143.

114.   Kash, K., et al., *Optical spectroscopy of ultrasmall structures etched from quantum wells*. Applied Physics Letters, 1986. **49**(16): p. 1043-1045.

115.   Fukui, T., et al., *GaAs tetrahedral quantum dot structures fabricated using selective area metalorganic chemical vapor deposition*. Applied physics letters, 1991. **58**(18): p. 2018-2020.

116.   Tolbert, S.H., et al., *Magnetic field alignment of ordered silicate-surfactant composites and mesoporous silica*. Science, 1997. **278**(5336): p. 264-268.

117.   Mishra, D., et al., *Growth modes of nanoparticle superlattice thin films*. Nanotechnology, 2014. **25**(20): p. 205602.

118.   Nabetani, Y., et al., *Initial growth stage and optical properties of a three-dimensional InAs structure on GaAs*. Journal of Applied Physics, 1994. **76**(1): p. 347-351.

119.   Leonard, D., et al., *Structural and optical properties of self-assembled InGaAs quantum dots*. Journal of Vacuum Science & Technology B: Microelectronics and Nanometer Structures Processing, Measurement, and Phenomena, 1994. **12**(4): p. 2516-2520.

120.   Asada, M., Y. Miyamoto, and Y. Suematsu, *Gain and the threshold of three-dimensional quantum-box lasers*. IEEE Journal of Quantum Electronics, 1986. **22**(9): p. 1915-1921.

121.   Asada, M., Y. Miyamoto, and Y. Suematsu, *Gain and the threshold of three-dimensional quantum-box lasers*.

122.   Asada, M., Y. Miyamoto, and Y. Suematsu, *Theoretical Gain of Quantum-Well Wire Lasers*. Japanese Journal of Applied Physics, 1985. **24**(Part 2, No. 2): p. L95-L97.

123.   Kim, J.K., et al., *Design parameters for lateral carrier confinement in quantum-dot lasers*. Applied Physics Letters, 1999. **74**(19): p. 2752-2754.

124.   Kirstaedter, N., et al., *Low threshold, large T/sub o/injection laser emission from (InGa) As quantum dots*. Electronics Letters, 1994. **30**(17): p. 1416-1417.

125.   Mirin, R., A. Gossard, and J. Bowers, *Room temperature lasing from InGaAs quantum dots*. Electronics Letters, 1996. **32**(18): p. 1732.

126.   Dingle, R. and C.H. Henry, *Quantum effects in heterostructure lasers*. 1976, Google Patents.

127.   Bhattacharya, P., et al., *High-speed modulation and switching characteristics of In (Ga) As-Al (Ga) As self-organized quantum-dot lasers*. IEEE Journal of Selected Topics in Quantum Electronics, 2000. **6**(3): p. 426-438.

128.   Huffaker, D.L., et al., *Continuous-wave low-threshold performance of 1.3-/spl mu/m InGaAs-GaAs quantum-dot lasers*. IEEE Journal of Selected Topics in Quantum Electronics, 2000. **6**(3): p. 452-461.

129.   Kim, J.K., R.L. Naone, and L.A. Coldren, *Lateral carrier confinement in miniature lasers using quantum dots*. IEEE Journal of Selected Topics in Quantum Electronics, 2000. **6**(3): p. 504-510.

130.   Nguyen, L., *Properties and applications of InP-based modulation doped heterostructures*. EMIS DATAREVIEWS SERIES, 1996. **15**: p. 328-331.

131.   Lourdudoss, S., *Heteroepitaxy and selective area heteroepitaxy for silicon photonics*. Current Opinion in Solid State and Materials Science, 2012. **16**(2): p. 91-99.

132.   Li, Q. and K.M. Lau, *Epitaxial growth of highly mismatched III-V materials on (001) silicon for electronics and optoelectronics.* Progress in Crystal Growth and Characterization of Materials, 2017. **63**(4): p. 105-120.

133.   Liebich, S., et al., *Laser operation of Ga(NAsP) lattice-matched to (001) silicon substrate.* Applied Physics Letters, 2011. **99**(7): p. 071109.

134.   *Critical dimensions for the plastic relaxation of strained axial heterostructures in free-standing nanowires.*

135.   Holt, D.B. and B.G. Yacobi, *Extended Defects in Semiconductors: Electronic Properties, Device Effects and Structures.* 2007, Cambridge: Cambridge University Press.

136.   Waters, R.G., *Diode laser degradation mechanisms: A review.* Progress in Quantum Electronics, 1991. **15**(3): p. 153-174.

137.   Sugo, M., et al., *1.5 μm-long-wavelength multiple quantum well laser on a Si substrate.* Japanese journal of applied physics, 1991. **30**(12S): p. 3876.

138.   Yang, V., et al., *Crack formation in GaAs heteroepitaxial films on Si and SiGe virtual substrates.* Journal of applied physics, 2003. **93**(7): p. 3859-3865.

139.   Ueda, O. and S. Pearton, *Materials and Reliability Handbook for Semiconductor Optical and Electron Devices.* 2013.

140.   Yamada, T., et al., *7000 h continuous wave operation of multiple quantum well laser on Si at 50 C.* Applied physics letters, 1997. **70**(12): p. 1614-1615.

141.   Chen, H., et al., *Continuous-wave operation of extremely low-threshold GaAs/AlGaAs broad-area injection lasers on (100) Si substrates at room temperature.* Optics letters, 1987. **12**(10): p. 812-813.

142.   Sugo, M., et al., *Stable cw operation at room temperature of a 1.5-μm wavelength multiple quantum well laser on a Si substrate.* Applied physics letters, 1992. **60**(4): p. 472-473.

143.   Groenert, M.E., et al., *Monolithic integration of room-temperature cw GaAs/AlGaAs lasers on Si substrates via relaxed graded GeSi buffer layers.* Journal of applied physics, 2003. **93**(1): p. 362-367.

144.   Mi, Z., et al., *High-performance quantum dot lasers and integrated optoelectronics on Si.* Proceedings of the IEEE, 2009. **97**(7): p. 1239-1249.

145.   Lacombe, D., et al., *Structural study of InAs quantum boxes grown by molecular beam epitaxy on a (001) GaAs-on-Si substrate.* Applied physics letters, 1997. **70**(18): p. 2398-2400.

146.   Chen, S., et al., *Electrically pumped continuous-wave III–V quantum dot lasers on silicon.* Nature Photonics, 2016. **10**(5): p. 307-311.

147.   Ovid'Ko, I., *Relaxation mechanisms in strained nanoislands.* Physical review letters, 2002. **88**(4): p. 046103.

148.   Yang, J., P. Bhattacharya, and Z. Mi, *High-Performance In$_{0.5}$Ga$_{0.5}$As Quantum-Dot Lasers on Silicon With Multiple-Layer Quantum-Dot Dislocation Filters.* IEEE Transactions on Electron Devices, 2007. **54**(11): p. 2849-2855.

149.   Tillmann, K. and A. Förster, *Critical dimensions for the formation of interfacial misfit dislocations of In0. 6Ga0. 4As islands on GaAs (001).* Thin Solid Films, 2000. **368**(1): p. 93-104.

150.   Yang, J., P. Bhattacharya, and Z. Mi, *High-Performance <formula*

formulatype="inline"><tex>$\hbox{In}_{0.5}\hbox{Ga}_{0.5} \hbox{As/GaAs}$</tex></formula> *Quantum-Dot Lasers on Silicon With Multiple-Layer Quantum-Dot Dislocation Filters.* IEEE Transactions on Electron Devices, 2007. **54**(11): p. 2849-2855.

151. Mi, Z., et al., *Self-organised quantum dots as dislocation filters: the case of GaAs-based lasers on silicon.* Electronics Letters, 2006. **42**(2): p. 121-123.

152. Tsao, J. and B. Dodson, *Excess stress and the stability of strained heterostructures.* Applied physics letters, 1988. **53**(10): p. 848-850.

153. Bogatov, A., et al., *Study of the single-mode injection laser.* IEEE Journal of Quantum Electronics, 1973. **9**(2): p. 392-394.

154. Voumard, C., R. Salathé, and H. Weber, *Resonance amplifier model describing diode lasers coupled to short external resonators.* Applied physics, 1977. **12**(4): p. 369-378.

155. KOBAYASHI, K., *Improvements in direct pulse code modulation of semiconductor lasers by optical feedback.* IEICE TRANSACTIONS (1976-1990), 1976. **59**(12): p. 8-14.

156. Broom, R., et al., *Microwave self-modulation of a diode laser coupled to an external cavity.* IEEE Journal of Quantum Electronics, 1970. **6**(6): p. 328-334.

157. Chinone, N., K. Aiki, and R. Ito, *Stabilization of semiconductor laser outputs by a mirror close to a laser facet.* Applied Physics Letters, 1978. **33**(12): p. 990-992.

158. Ikushima, I. and M. Maeda, *Self-coupled phenomena of semiconductor lasers caused by an optical fiber.* IEEE Journal of Quantum Electronics, 1978. **14**(5): p. 331-332.

159. Morikawa, T., et al., *Return-beam-induced oscillations in self-coupled semiconductor lasers.* Electronics Letters, 1976. **12**(17): p. 435-436.

160. He, Y., et al., *10-Gbps 20-km Feedback-Resistant Transmission Using Directly Modulated Quantum-Dot Lasers.* IEEE Photonics Technology Letters, 2020. **32**(21): p. 1353-1356.

161. Park, K.H., et al., *The effects of external optical feedback on the power penalty of DFB-LD modules for 2.5Gbs−1 optical transmission systems.* Optical and Quantum Electronics, 1998. **30**(1): p. 23-31.

162. Petermann, K., *External optical feedback phenomena in semiconductor lasers.* IEEE Journal of Selected Topics in Quantum Electronics, 1995. **1**(2): p. 480-489.

163. Alam, M.F. and M.A. Karim, *External Optical Feedback Effects in Distributed Feedback Semiconductor Lasers*, in *Advances in Imaging and Electron Physics*, P.W. Hawkes, Editor. 1999, Elsevier. p. 73-120.

164. Sigg, J., *Effects of optical feedback on the light-current characteristics of semiconductor lasers.* IEEE journal of quantum electronics, 1993. **29**(5): p. 1262-1270.

165. Tkach, R. and A. Chraplyvy, *Regimes of feedback effects in 1.5-μm distributed feedback lasers.* Journal of Lightwave Technology, 1986. **4**(11): p. 1655-1661.

166. Temkin, H., et al., *Reflection noise in index-guided InGaAsP lasers.* IEEE journal of quantum electronics, 1986. **22**(2): p. 286-293.

167. Fujiwara, M., K. Kubota, and R. Lang, *Low-frequency intensity fluctuation in laser diodes with external optical feedback.* Applied Physics Letters, 1981. **38**(4): p. 217-220.

168. Li, H., J. Ye, and J.G. McInerney, *Detailed analysis of coherence collapse in*

semiconductor lasers. IEEE journal of quantum electronics, 1993. **29**(9): p. 2421-2432.

169.   Lenstra, D., B. Verbeek, and A.D. Boef, *Coherence collapse in single-mode semiconductor lasers due to optical feedback.* IEEE Journal of Quantum Electronics, 1985. **21**(6): p. 674-679.

170.   Cohen, J.S. and D. Lenstra, *The critical amount of optical feedback, for coherence collapse in semiconductor lasers.* IEEE Journal of Quantum Electronics, 1991. **27**(1): p. 10-12.

171.   Hirota, O. and Y. Suematsu, *Noise properties of injection lasers due to reflected waves.* IEEE Journal of Quantum Electronics, 1979. **15**(3): p. 142-149.

172.   Spano, P., S. Piazzolla, and M. Tamburrini, *Theory of noise in semiconductor lasers in the presence of optical feedback.* IEEE Journal of Quantum Electronics, 1984. **20**(4): p. 350-357.

173.   Wieczorek, S., et al., *The dynamical complexity of optically injected semiconductor lasers.* Physics Reports, 2005. **416**(1): p. 1-128.

174.   Mork, J., B. Tromborg, and J. Mark, *Chaos in semiconductor lasers with optical feedback: theory and experiment.* IEEE Journal of Quantum Electronics, 1992. **28**(1): p. 93-108.

175.   Lang, R. and K. Kobayashi, *External optical feedback effects on semiconductor injection laser properties.* IEEE Journal of Quantum Electronics, 1980. **16**(3): p. 347-355.

176.   Acket, G., et al., *The influence of feedback intensity on longitudinal mode properties and optical noise in index-guided semiconductor lasers.* IEEE Journal of Quantum Electronics, 1984. **20**(10): p. 1163-1169.

177.   Helms, J. and K. Petermann, *A simple analytic expression for the stable operation range of laser diodes with optical feedback.* IEEE Journal of Quantum Electronics, 1990. **26**(5): p. 833-836.

178.   Patzak, E., et al. *Spectral linewidth reduction in semiconductor lasers by an external cavity with weak optical feedback.* Electronics Letters, 1983. **19**, 938-940.

179.   Lax, M., P. Kelley, and P. Tannenwald, *Physics of quantum electronics.* New York, 1966: p. 735.

180.   de L. Kronig, R., *On the Theory of Dispersion of X-Rays.* Journal of the Optical Society of America, 1926. **12**(6): p. 547-557.

181.   Henry, C., *Theory of the linewidth of semiconductor lasers.* IEEE Journal of Quantum Electronics, 1982. **18**(2): p. 259-264.

182.   Osinski, M. and J. Buus, *Linewidth broadening factor in semiconductor lasers-- An overview.*

183.   Koch, T.L. and J.E. Bowers *Nature of wavelength chirping in directly modulated semiconductor lasers.* Electronics Letters, 1984. **20**, 1038-1040.

184.   Su, H., et al., *High external feedback resistance of laterally loss-coupled distributed feedback quantum dot semiconductor lasers.* IEEE Photonics Technology Letters, 2003. **15**(11): p. 1504-1506.

185.   Uskov, A.V., et al., *Carrier-induced refractive index in quantum dot structures due to transitions from discrete quantum dot levels to continuum states.* Applied Physics Letters, 2004. **84**(2): p. 272-274.

186.   Newell, T., et al., *Gain and linewidth enhancement factor in InAs quantum-dot*

laser diodes. IEEE Photonics Technology Letters, 1999. **11**(12): p. 1527-1529.

187.   Ukhanov, A.A., *Study of the Carrier-induced optical properties in III-V quantum confined laser nano-structures.* 2004: The University of New Mexico.

188.   Smowton, P.M., et al., *Filamentation and linewidth enhancement factor in InGaAs quantum dot lasers.* Applied physics letters, 2002. **81**(17): p. 3251-3253.

189.   Oksanen, J. and J. Tulkki, *Linewidth enhancement factor and chirp in quantum dot lasers.* Journal of Applied Physics, 2003. **94**(3): p. 1983-1989.

190.   Grillot, F., et al., *Gain Compression and Above-Threshold Linewidth Enhancement Factor in 1.3-$\mu\hbox{m}$ InAs–GaAs Quantum-Dot Lasers.*

191.   O'Brien, D., *Sensitivity of Quantum Dot Lasers to External Optical Feedback Supervisors.* 2004.

192.   Kuntz, M., et al., *Spectrotemporal response of 1.3 μm quantum-dot lasers.* Applied Physics Letters, 2002. **81**(20): p. 3846-3848.

193.   Schunk, N. and K. Petermann *Measured feedback-induced intensity noise for 1.3 μm DFB laser diodes.* Electronics Letters, 1989. **25**, 63-64.

194.   Schunk, N. and K. Petermann, *Numerical analysis of the feedback regimes for a single-mode semiconductor laser with external feedback.* IEEE Journal of Quantum Electronics, 1988. **24**(7): p. 1242-1247.

195.   Henry, C. and R. Kazarinov, *Instability of semiconductor lasers due to optical feedback from distant reflectors.* IEEE Journal of Quantum Electronics, 1986. **22**(2): p. 294-301.

196.   Sigg, J., *Effects of optical feedback on the light-current characteristics of semiconductor lasers.* IEEE Journal of Quantum Electronics, 1993. **29**: p. 1262-1270.

197.   Biesterbos, J., et al., *Low-frequency mode-hopping optical noise in AlGaAs channeled substrate lasers induced by optical feedback.* IEEE Journal of Quantum Electronics, 1983. **19**(6): p. 986-990.

198.   O'Brien, D., et al., *Feedback sensitivity of 1.3 μm InAs/GaAs quantum dot lasers.* Electronics Letters, 2004. **39**: p. 1819-1820.

199.   Huang, Y., et al. *External optical feedback resistant characteristics in partially corrugated-waveguide laser diodes.* Electronics Letters, 1996. **32**, 1008-1009.

200.   Yidong, H., et al., *External optical feedback resistant 2.5-Gb/s transmission of partially corrugated waveguide laser diodes over a -40℃ to 80℃ temperature range.* IEEE Photonics Technology Letters, 1999. **11**(11): p. 1482-1484.

201.   Favre, F. *Sensitivity to external feedback for gain-coupled DFB semiconductor lasers.* Electronics Letters, 1991. **27**, 433-435.

202.   Huang, H., et al., *Epitaxial quantum dot lasers on silicon with high thermal stability and strong resistance to optical feedback.* APL Photonics, 2020. **5**(1): p. 016103.

203.   Dong, B., et al. *P-doping effect on external optical feedback dynamics in 1.3-μm InAs/GaAs quantum dot laser epitaxially grown on silicon.* in *Photonics Europe.* 2020.

204.   Mizutani, K., et al. *Isolator free optical I/O core transmitter by using quantum dot laser.* in *2015 IEEE 12th International Conference on Group IV Photonics (GFP).* 2015.

2   Static characteristics

In this chapter, a systematic study of the static characteristics of narrow ridge quantum dot (QD) lasers is performed. Before the measurement start, the fundamentals of QD epitaxial are first discussed. The molecular beam epitaxy (MBE) techniques and equipment are provided. Then the grown QD material is characteristic using atomic force microscopy (AFM) and photoluminescence (PL). The device structure and fabrication methods are also provided later. After the material growth and fabrication is introduced, the static characteristic measurements are carried out, mainly based on the light-current-voltage (LIV) curve. Further characteristics such as efficiency and loss can be extracted experimentally by subsequently cleaving lasers to different cavity lengths and measuring the corresponding threshold current densities. The metrics of QD laser regarding the low threshold and high temperature stability are verified in the testbed.

2.1 Material growth, characterisation and device fabrication

Firstly, a description of the working principles of MBE and epitaxy structure of the wafer are given. In essence, MBE is material deposition technique based on ultra-high vacuum evaporation method [1]. The composition and doping of the impurity level can be precisely tailored and controlled below the accuracy of ten parts per billion. The schematic process of MBE is shown in Figure 2.1. During the growth, the molecular beam is generated by fluxes of constituent matrix and doping species, which will be deposited on the substrate with an average rate on the order of around one monolayer per second.
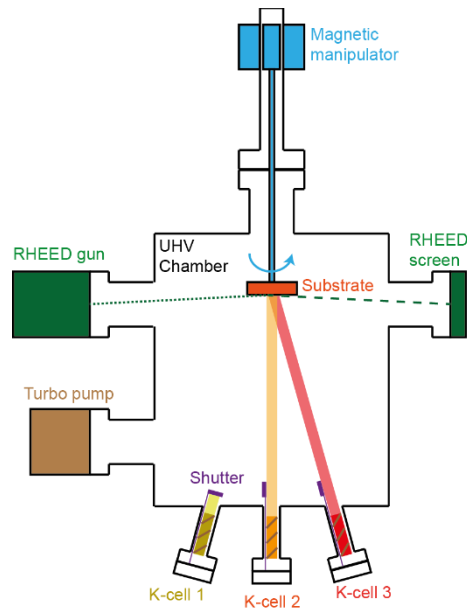
Figure 2.1: Schematic representation of the MBE processes and control interface [1].

The sources are heated and transferred from the flux generators to the substrate. By altering the evaporation condition or controlling the mechanical shutters, the constituents of deposited material can be temporarily controlled. QD samples used in this thesis were grown in UCL using solid-source MBE reactor epitaxy on an n-doped GaAs substrate.
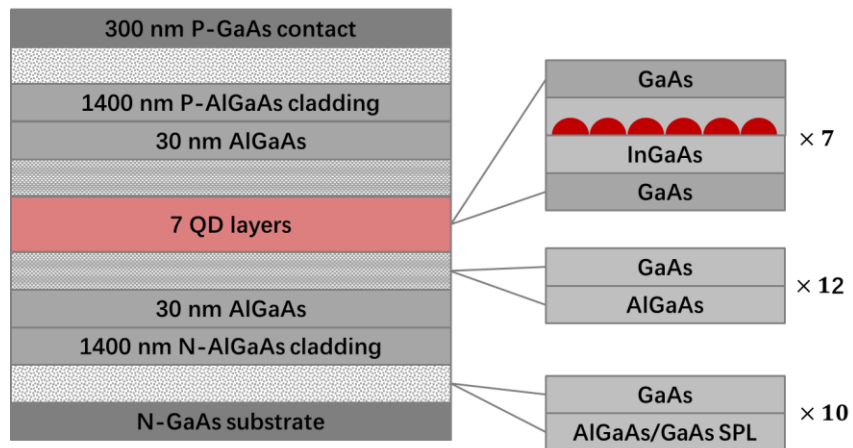
Figure 2.2:Shematic diagram of InAs/GaAs QD wafer.

The QD wafer is designed based on the previous optimised structures used in [2, 3] and the layer structure is shown in Figure 2.2. It is composed of two1400 nm-thick AlGaAs cladding layers

and active region of seven stacked layers of InAs/GaAs QDs. The upper and lower cladding layers were doped with Be and Si, respectively. The self-organisation of nanoscale 3D clusters due to the strain-induced transformation of the pseudomorphic layers has emerged as one of the most promising ways for in situ QD fabrication. Each QD layer consists of 3 monolayers of InAs grown on 2 nm InGaAs before capping with 5 nm of InGaAs. This dot-in-a-well (DWELL) method is based on capping the self-assembled InAs QD with the less strained InGaAs. One of the main merits of DWELL structure is the improved surface dot density per layer. A 42.5 nm GaAs spacer layer, in which the 6 nm-thick p-modulation doping with Be is applied, is inserted between each DWELL layer.

Then relative characteristics are measured, AFM and PL. AFM is a mechanical profilometer with the capability to image almost all types of surfaces, including conductor, semiconductor and even insulator. It gives a straightforward topography of QD structure in three dimensionalities. In force microscopy, the sample is fixed on a holder positioned accurately in lateral and vertical directions, and the probing tip is attached to a cantilever, which is mounted on another holder. Most of the scanning probe microscopes is based on piezoelectric element which is made of crystals that create electrical polarisation when deformed mechanically. The basic components and relation between the distance and force are shown below.
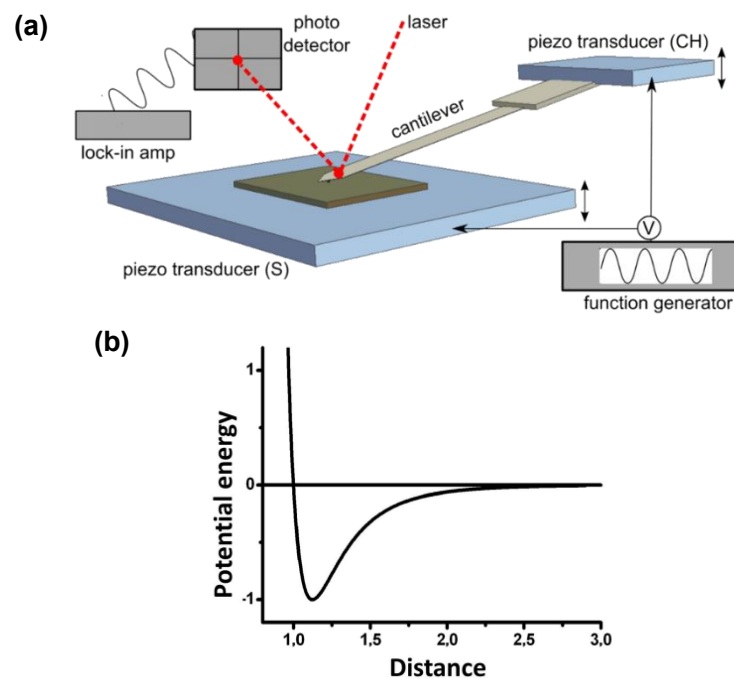
Figure 2.3(a) Basic principle of AFM [4] and (b) Force-distance curve [5].

As the cantilever is approaching the sample, it is bent due to the interaction between tip and sample. In the detection system, a laser beam is directed onto the cantilever and reflected onto photodiodes. The generated force depends on the distance and is determined by the deflection of the cantilever. Morphology of the sample, including its roughness and height distributions, is taken quantitively through digitizing the reflection as a function of distance. In addition to deflection sensor and force measurement circuit, traditional positioning and feedback loop control are included in the basic AFM system. The AFM image of InAs/GaAs QD of our sample is shown in Figure 2.4, which indicates a high dot density of $3 \times 10^{10}/cm^2$ with good uniformity.
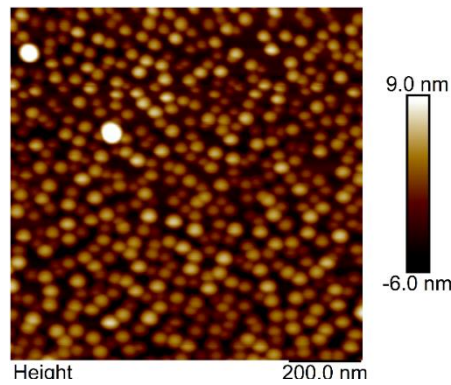
Figure 2.4:AFM of the QD wafer used in this thesis. The right bar gives the color map corresponding different height of wafer.

PL spectroscopy is a non-contact, non-destructive method to characterize the optical properties of samples. From the extracted information, sample composition, crystal defects, and even the internal stresses can be identified. In the case of QD samples, PL spectrum provides the information about the QD monodispersity that can facilitate sample analysis. PL is a spontaneous emission by the optical excitation. When the light directed onto a sample is absorbed, photon-excitation occurs. The electron in the lower energy state (valence band (VB) for semiconductor) is excited to higher energy state (conduction band (CB) for semiconductor). Photon is released when the excited electron returns back to the lower energy level.
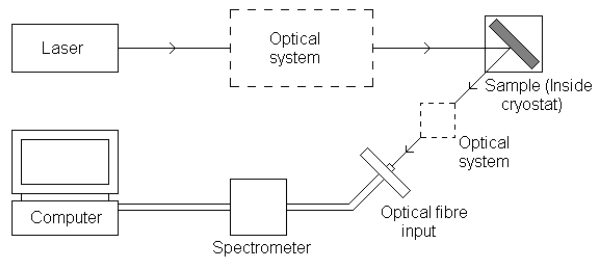
Figure 2.5:Shematic diagram of PL setup.

The PL spectral characterisation is obtained by an automated spectrofluorometer system in Figure 2.5. In our measurement, a laser beam generated by 532 nm source is directed onto the surface at room temperature. Under the optical excitation, PL occurs with the photon emission corresponding the bandgap of sample. The reflected beam is directed into the monochromator, in which a diffraction grating is used to diffract different wavelengths separately toward an array of detector. The intensity of corresponding wavelengths is interpreted by the digital information to form a PL spectrum.
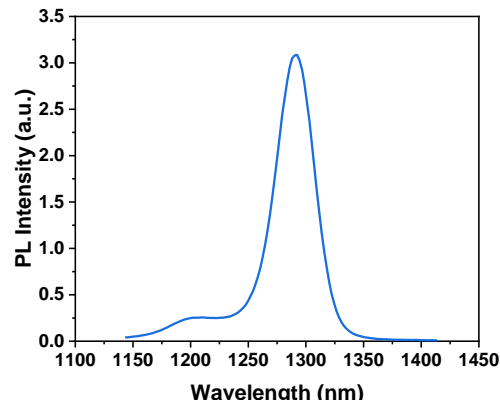
Figure 2.6:PL of the QD sample.

The displayed spectrum indicates the distribution of relative PL intensities measured by the detector. PL spectrum of our QD sample is shown in Figure 2.6. The intense peak appears at 1290 nm with a full width at half maximum (FWHM) around 31 meV. The broadening of PL spectrum results from the inhomogeneity of QD distribution. This notable peak and narrow width of the PL spectrum also indicates good dot uniformity. An additional shoulder exists at 1205 nm, corresponding to the excited state (ES) emission.

With the QD material is verified with high density and great uniformity based on AFM and

PL results, the wafer is then fabricated to laser device. Figure 2.7 gives the brief processes of the fabrication flow chart. Prior to the structure fabrication, sample cleaning is the first crucial process. The contaminants formed during the growth can severely degrade the device performance and yield. During the cleaning, acetone and isopropyl alcohol are usually employed with the ultrasonic vibration. Then, the wafer is blown dry by a nitrogen gun. Processes are repeated until there are no obvious particles on the wafer surface under the microscope of view at 50x magnification.
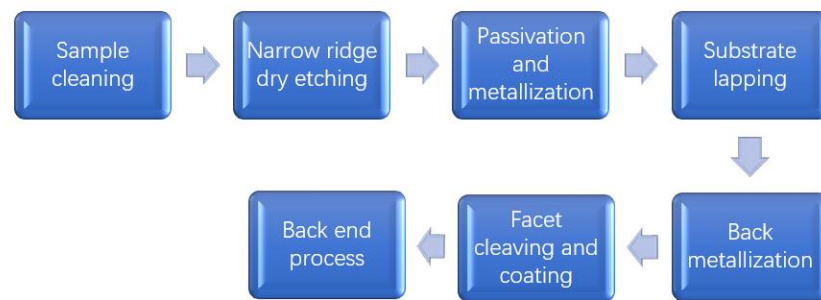
Figure 2.7: Flow chart of laser fabrication processes.

In the following processes, several critical techniques, including photolithography, chemical wet/dry etching, passivation, metallisation, and facet coating, are carried out. Photolithography, also called as ultra-violet (UV) lithography, is one of the most basic techniques for forming accurate and precise patterns in semiconductor manufacturing. The patterns are transferred on the substrate under the UV light exposure by using photosensitive chemical known as photoresist. Typically, the UV light is in the range of 350 to 430 nm wavelength. After which the photoresist is selectively dissolved in the corresponding developer. These delineated areas are subsequently used for etching, deposition or doping. The main advantage of photolithography is the ability for mass production and high efficiency. However, the limiting size of the individual elements is about 1 μm due to the diffraction of the optical systems. Advanced photolithographic strategies provide precise control of the shape and size down to few tens of nanometers with the expense of high cost and long writing-time. Another problem that needs to be addressed is the task of designing optics to form precise image over the wafer with growing size.

Several strategies have been pursued to achieve the dimensions and overlay accuracies required for next generation devices, including short wavelength lithography, electron beam lithography (EBL), x-ray lithography, and ion beam lithography. An EBL system is comprised of

several subsystems, including electron optical column, analog/digital electronics, high-precision mechanical stage, and high vacuum system. By scanning focused electron beams onto a sample surface covered by organic polymer film, similar to the physical mechanism of photolithography, the solubility of the resist in developer is altered by the passage of electrons. The ultimate resolution is typically in the range of few nanometers. Another advantage of EBL over the photolithography is that any arbitrary pattern can be directly written without the pre-existing photo-mask. EBL is currently used by many companies to manufacture high-resolution devices and try out a large number of different patterns in development phase. In our fabrication, the 5 μm narrow ridge is defined by the EBL and wide contact metal area is exposed by photolithography.

Once the ridge width of laser is defined, the stripe structure is then fabricated using etching techniques which removes layers or slices of material There are two basic types of etching agents: liquid or plasma phase. Removing material by using liquid chemical is called wet etching while the plasma etching process by the plasmas or gases is referred as dry etching. Several considerations are needed to be taken into account for deciding the etchant type.

In the wet etching process, the substrate is partially protected by the resist. Chemicals such as hydrofluoric acids, nitric acids, phosphoric acids, and hydrochloric acids are usually employed as the etchant due to the corrosive properties. The wafer is laid into a tank full of liquid solution or sprayed by etchant while rotating. The unprotected part is removed as the wafer immersed in chemical solution. It is easy to implement wet etching with simple equipment and related chemicals and the etch rate is particularly high with good material selectivity. However, the matter of safety is needed for consideration and proper care should be taken around the regularly changed solution and cleaning of the corrosive liquid afterwards. Another drawback of wet etching is the isotropic property. Complex interaction on molecular level is caused during the etching and results in the different shape of the surface. In isotropic etching, the etching rate towards all directions are identical and results in a semi-circular shape. The removed materials are not strictly defined by the mask. Meanwhile, undercuts of the mask are usually formed and wet etching are thus considered to be not accurate. Anisotropic etching is desired in the fabrication to achieve the accurate mask pattern transfer, as the material cut out is only perpendicular to the surface. Dry etch techniques are employed to remove a masked pattern of semiconductor material with a tendency toward anisotropism in a quite flexible process. High kinetic energy beams in plasma phase are used to

knock off atoms on substrate and reacted material is removed in the evaporation form. Performance parameters such as etching rate, selectivity, uniformity, and anisotropy can be modified depending on the technique used and conditions such as gases categories and distance to the substrate. Encompassed chambers are assembled in dry etching equipment and the safety risks are considered rather low.

There are two techniques included in our narrow ridge laser fabrication: reactive ion etching (RIE) and inductively coupled plasma reactive ion etching (ICP-RIE). For RIE etching, chemical reactive species are accelerated by the high-frequency electrode and directed toward the etching surface. Its directionality can be controlled by adjusting the pressure and electric intensity inside the chamber. More control is allowed in ICP-RIE by adding the RF-powered magnetic field on the top of RIE system. The plasma state is created in this case and shattering ionised gas molecules are propelled towards the substrate. In semiconductor markets for device manufacturing, both wet etching and dry etching technologies are employed. The wet etching provides high selectivity with simpler equipment, while dry etching offers strong anisotropic control with greater precision and safer operation. The ICP etching is used to form the shallow etched narrow ridge, while the wet etching is used for the smoothing purpose.

Followed by laser fabricated, connections via metal layer deposited on the wafer forms conductive pathways. The formation of electrode is important in determining the performance of most semiconductor devices. Different types of contact between metal and semiconductor, Schottky and Ohmic contact schematically depicted in Figure 2.8, are formed due to the Fermi energy mismatch. When the potential barrier height between the Fermi energy of the two materials is relatively large, a Schottky barrier contact is formed. Generally, Schottky barriers could lead to rectifying characteristics and when the current flowing through the Schottky contact, it shows a current-voltage characteristics similar to those of pn-junction. Materials such as Titanium Silicide and Platinum Silicide can be used to form Schottky contact with both p- and n-type semiconductors.
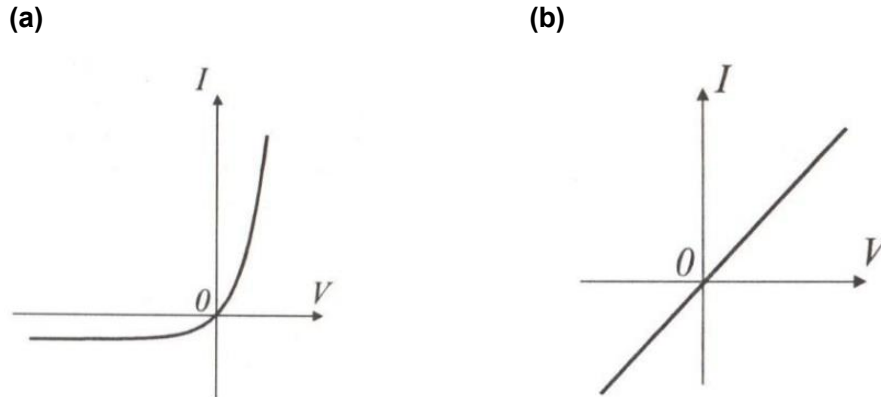
Figure 2.8: Schematic IV characteristics of (a) Schottky and (b) Ohmic contact.

The desired metal contact for laser diode is the Ohmic contact. Under this situation, no potential barrier is formed and the current can be conducted in both directions as shown in above figure. Ideally, low resistance and non-rectifying junction Ohmic contact is desired. Generally, the Ohmic contact for III-V compounds are deposited by sputtering or evaporation processes while the contact layers are high doped to narrow the depletion region. For Ohmic contact to GaAs, Ti/Pt/Au, PdGe, and NiGeAu are usually used. Additionally, several techniques are employed to reduce Schottky barrier height: plasma surface pretreatment and buffer layer with low bandgap alloy [6, 7].

In our works, the contact layers are doped at a level of $10^{18}/cm^3$ by MBE to achieve low contact resistances. A Ti/Pt/Au (20 nm/50 nm/ 400nm) layer was used as a anode and deposited by sputtering. To perform sputtering, the plasma of inert carrier gases is formed in a low-pressure circumstance. The ionised atoms with the applied electric field are drawn to the target source that will be deposited. The target atoms are dislodged as ions strike and will then be deposited in a thin film on substrate. In our metal contact scheme, the Ti layer was used to prevent the diffusion and increase the adhesion between the semiconductor and metal, while the Pt layer can also avoid Au diffusion [8, 9]. For the n-type contact layer, Ni/GeAu/Ni/Au (10 nm/100 nm/30 nm/200 nm) was designed and deposited by the thermal evaporator with annealing afterwards. The first Ni layer was used to improve the adhesion while the second layer works as a barrier layer [10, 11]. GeAu alloy forms a heterostructure barrier, and the final layer is provided for the contact [12].

The schematic plot and scanning electron microscopy (SEM) image of the cross section of laser is shown in Figure.2.9. The device structure employed in this research is narrow ridge shallow

etched above active region with top-bottom metal. Human eyes can distinguish two points in space down to 0.2 mm. As dimensions of the subjects and materials are shrinking, electron microscope was developed to provide higher resolution to detect the nanostructure in samples. The SEM projects and scans a focused electron beam over the sample surface, and the topography and composition of specimen are obtained from the produced signals. As the electrons penetrate and interact with the sample, secondary electrons, backscattered electrons and X-rays are produced. These signals are then collected by detectors, and the corresponding figures reveal information about external morphology, chemical deposition and crystalline structure. The maximum resolution of SEM is increased to less than 20 nm.
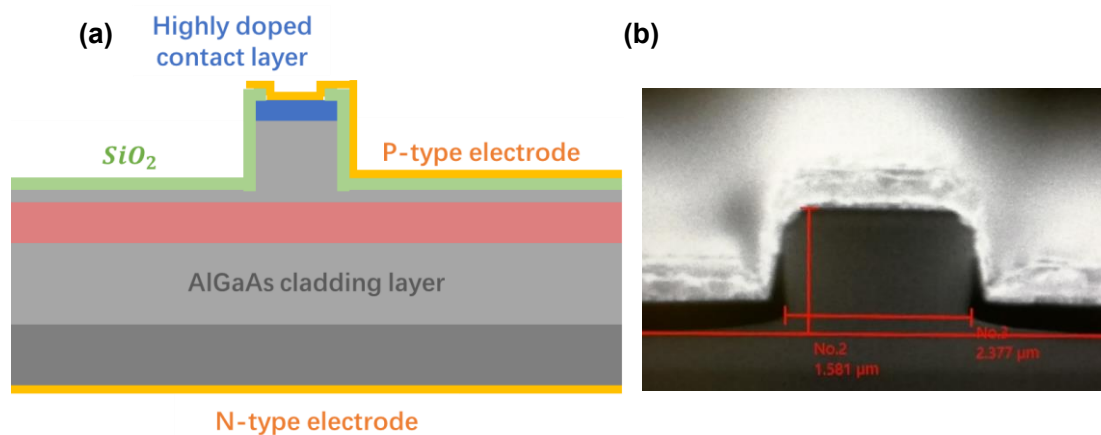
Figure 2.9: (a)Cross section diagram of narrow-ridge FP laser and (b) SEM of the cross section of fabricated device.

In Fabry-Perot (FP) laser, the cleaved facets could be served as mirrors with specific reflectivity. In principle, laser emits radiation from the front as well as the back facet. However, only the optical output from one facet is desired in many applications. The output power can be enhanced by modifying the facet reflectivity through anti-reflection (AR) and high-reflection (HR) coating, which at the same time serve as a role of protection and passivation. The characteristics, including threshold current, output power, efficiencies, feedback resistance and even dynamical properties, can be impacted and improved with the different coating conditions. HR coating with reflectivity greater than 90% at the rear facet is widely applied, as for most of the practical applications, a little bit amount of output power from rear end is needed for monitoring purpose. The deposition of HR coating works on the constructive interference, which can be achieved by

alternate stack of Si and Al_2O_3. The light is reflected from successive boundaries of multilayer dielectric films and gathers in phase. On the other hand, AR coating, based on the complete cancellation of the reflected light at the upper and lower surfaces of a single layer of dielectric material, is desired in some cases such as the amplifier and external cavity systems. The optical thickness of the coated dielectric is calculated to be one quarter of the lasing wavelength.

2.2 Experimental setup

After fabrication of the laser devices, their properties are first characterised. Laser bars with different length and coating conditions are tested by measuring the light output and voltage as a function of current to derive various properties.

One of the most important characteristics of laser devices is the light output as a function of current density. The basic setup for light current (LI) measurement is shown in Figure 2.10, with LabVIEW software used to communicate between the instruments and record the result. The mounted device under test (DUT) was placed on metal plate with a temperature controller and thermoelectric cooler to keep temperature constant during testing. Keithley 2400 was used as a continuous-wave (CW) current source, and electrical contact to laser was made via probes. The optical header interface without any lenses was placed as close to the lasing facet as possible to collect the output light, and the power was measured via the lightwave multimeter. The resulting LI graph shows the transition of the laser output from spontaneous emission to stimulated emission and the increase in stimulated emission intensity with current.
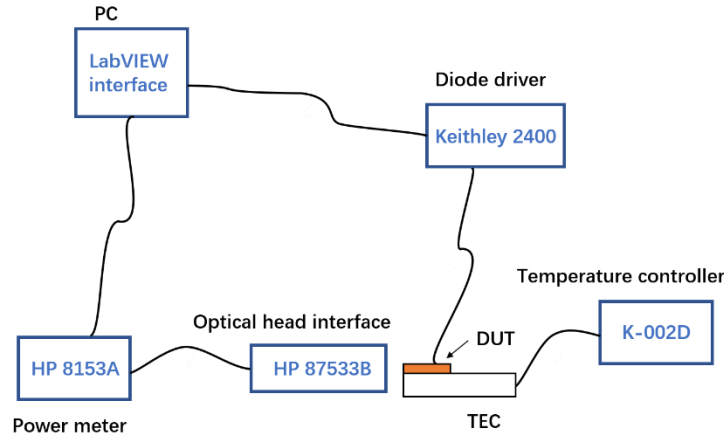
Figure 2.10: LI setup

Based on the above setup, the different LIV characteristics regarding the optical and the electrical properties under different temperature can be derived. To further obtain the efficiencies and internal loss, it is common to measure the LI curves of different cavity length and plots the inverse slope efficiency (SE) versus the length. However, this method neglects the enhanced loss mechanism with short cavity length. Advanced laser simulation software such as PICS3D was employed to self-consistently reproduce and study the impact of the lengths on internal loss and internal efficiency [13]. In addition, compared to quantum well (QW), the increased mean dot carrier occupancy results in early onset of gain saturation [14]. This gain saturation also means that careful consideration of length dependent results must be undertaken to form an accurate picture of QD lasing characteristics. As a result, when extracting data, the shorter length samples tended not to be considered.

2.3 Rate equation

Before the measurements carried out, an important analysis tool needs to be introduced, rate equations, which describes the operation between carriers and photons inside the active region. Based on this group of equations, the most common static characteristic and even dynamic performance can be theoretically predicted. We first analyze the carrier concentration N_e by separately considering the generation and consumption terms.

$$\frac{dN_e}{dt} = G_{gen} - R_{rec} \qquad \text{Equation 2.1}$$

$$G_{gen} = \frac{\eta_i I}{qV} \qquad \text{Equation 2.2}$$

$$R_{rec} = R_{sp} + R_{st} + R_{nr} + R_l \qquad \text{Equation 2.3}$$

where η_i is the injection efficiency defined as the ratio of terminal current that generates electron-hole pairs in the active region to the total injected current I, q is the elementary electron charge and V is the volume of the active region. The recombination processes, which includes spontaneous emission rate R_{sp}, stimulated emission rate R_{st}, nonradiative recombination rate R_{nr}, and current leakage rate R_l, are more complicated

The lifetime τ of particles is often used to describe its decay rate with the definition of,

$$N(t) = N(0)e^{-\frac{t}{\tau}} \qquad \text{Equation 2.4}$$

N denotes for both the carrier and photon density. We first consider the simplest circumstance when there are no injected carriers ($G_{gen} = 0$) and photons ($R_{st} = 0$). The rate equations for the carrier density and carrier lifetime are derived as,

$$\frac{dN_e}{dt} = -\frac{N_e}{\tau_e} \qquad \text{Equation 2.5}$$

$$\frac{N_e}{\tau_e} = R_{sp} + R_{nr} + R_l \qquad \text{Equation 2.6}$$

Similar to the rate equation for carriers, when constructing the rate equation for photons, we need to include the generation and loss terms.

$$\frac{dN_p}{dt} = \Gamma R_{st} + \Gamma \beta_{sp} R_{sp} - \frac{N_p}{\tau_p} \qquad \text{Equation 2.7}$$

where ΓR_{st} is the fraction of photons generated by stimulated recombination. For the spontaneous emission, photons are emitted in all directions over a wide spectral range, and only a small fraction could resonate along the cavity, contributing to the lasing. Thus, the contribution of spontaneous emission should be multiplied by the coupling factor β_{sp}. The depletion of photons mainly relates to the cavity loss and mirror loss which could be described as,

$$N_p(t) = N_p(0)e^{-\frac{t}{\tau_p}} \qquad \text{Equation 2.8}$$

$$\tau_p = \frac{1}{v_g(\alpha_{mir} + \alpha_i)} \qquad \text{Equation 2.9}$$

The growth of photon density can also be described in terms of the gain g over small length Δz. When Δz is sufficiently small, $e^{g\Delta z} \approx 1 + g\Delta z$ and $\Delta z = v_g \Delta t$ (v_g is the group velocity).

The R_{st} can be represented as,

$$R_{st} = v_g g N_p \qquad \qquad \textit{Equation 2.10}$$

Overall, the coupled rate equations are rewritten as,

$$\frac{dN_e}{dt} = \frac{\eta_i I}{qV} - v_g g N_p - \frac{N_e}{\tau_e} \qquad \qquad \textit{Equation 2.11}$$

$$\frac{dN_p}{dt} = \Gamma v_g g N_p + \Gamma \beta_{sp} R_{sp} - \frac{N_p}{\tau_p} \qquad \qquad \textit{Equation 2.12}$$

These rate equations will be solved to analyze the steady and dynamic responses of the lasers in the following sections.

2.4 Static characteristics

Static CW measurement of length dependent characterisation, and characteristics temperature T₀ measurements are carried out in this section. Since the facet reflectivity will impact the performance of lasers regarding its threshold, output power and essentially, the feedback sensitivity. The detailed studies of the static characteristic of QD laser comprises of FP lasers with 8 different lengths with and without coating.

2.4.1   Basic light-current-curve characteristics

The basic LIV characteristics of FP lasers with different length are presented in this section. The illustration of LI curve provides the most fundamental relationship between the input current and output optical power. It is generated by plotting the power out from the facet as a function of the drive current. From the LI curve, the threshold current and SE could be easily derived. In addition, several other complex efficiencies can be determined by length-dependent calculation.

As the current is injected into the laser, carriers will initially accumulate in the active region and the photon concentration increases gradually. When the carrier density exceeds the threshold value to compete the loss and spontaneous emission, stimulated emission becomes dominant and output power surges. The first parameter of interest is the point onset of laser action, typically referred to as the threshold current denoted by the symbol I_{th}. Lower threshold current is much

desirable from the power consumption aspect. From the physical view, the change in injection current and optical output corresponds to the variation in the carrier and photon density. Thus, the LI curve can be analytically expressed by rate equations. When the injected current has not reached threshold, both the stimulated emission rate and photon density are negligible ($N_p = 0$). The generation term in steady-state carrier rate equation equals recombination term, and Equation 2.11 reduces to

$$\frac{\eta_i I_{th}}{qV} = \frac{N_{e\_th}}{\tau_e} \qquad \text{Equation 2.13}$$

Above threshold, the carrier population is clamped at the threshold value, since all additional carriers further injected to the active region contribute directly to the generation of photons into the lasing mode. By solving Equation 2.11, Equation 2.12, and Equation 2.13, the linear relationship between the injection current and the output optical power is mathematically proved.

$$N_p = \frac{\eta_i(I - I_{th})}{qV v_g g} \qquad \text{Equation 2.14}$$

$$P_{out} = 2\Gamma v_g \alpha_{mir} h\upsilon V N_p \qquad \text{Equation 2.15}$$

The primary benefit of the QD laser is the ultra-low threshold current. Due to the size quantisation in QDs, the injected non-equilibrium carriers concentrate in a narrow energy band range near the band edge. The increase of density of state leads to a much steeper dependence of optical gain on the injection current, and the deep confinement potentials led to efficient ground state (GS) emission [15-18]. All of these contribute to the lower threshold current density of QD laser. In addition, due to the rapid filling of the charge carriers into the working states, population inversion is achieved with fewer injected carriers and thus lower transparency current density.
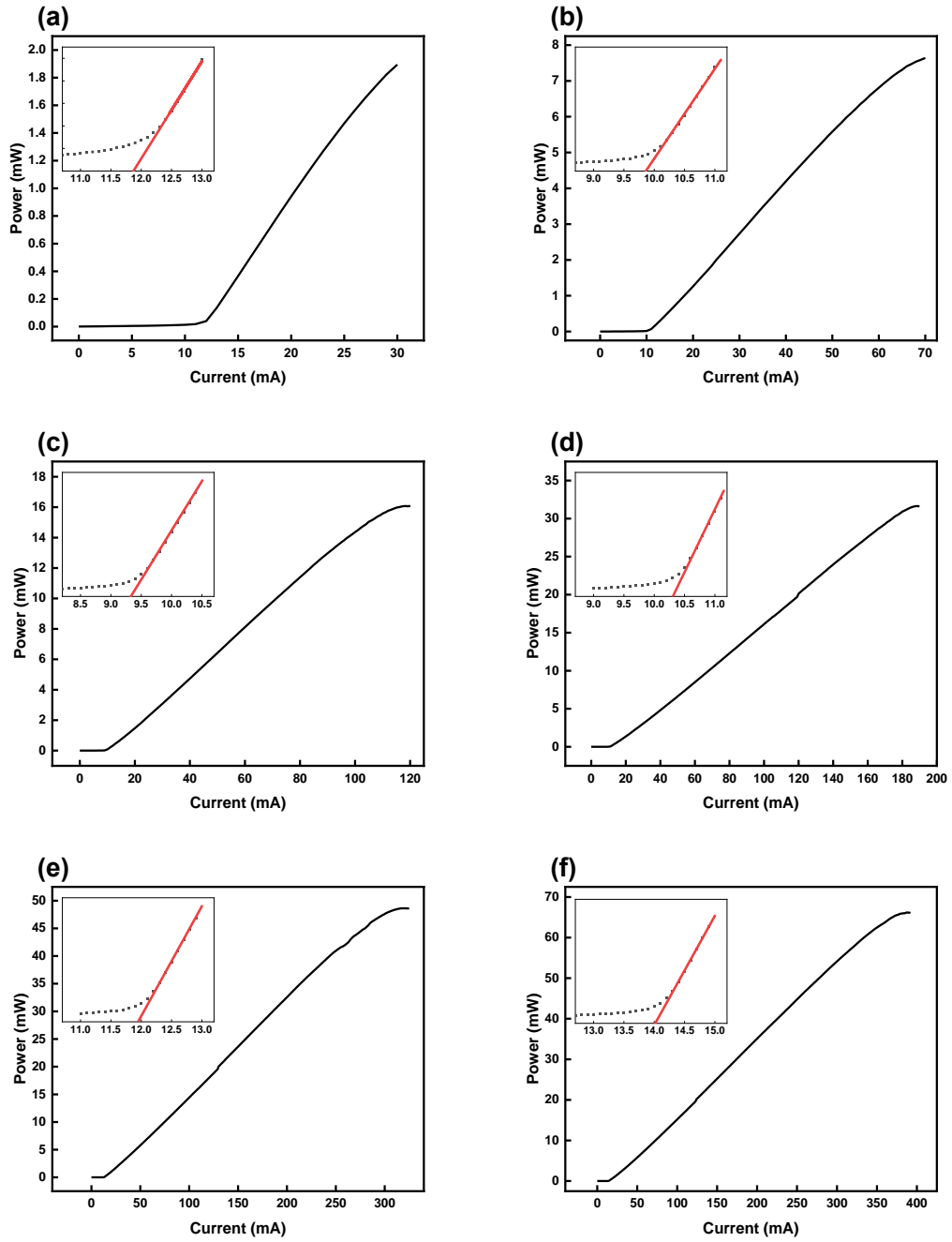
Figure 2.11: LIV curves of different caivty lengths (a) 300 μm, (b) 350 μm, (c) 400 μm, (d) 600 μm, (e) 800 μm and (f) 1000 μm.

As-cleaved FP lasers with 2.2 μm width and 6 different cavity length (300, 350, 400, 600, 800, and 1000 μm) were fabricated and measured. The 300 μm long as-cleaved laser exhibited a maximum CW output power of $1.9 \, mW$ per facet at an injection current of $30 \, mA$, as shown in Figure 2.11. From the inset, a threshold current of $11.72 \, mA$ was obtained at room temperature. Based on the ridge width and cavity length provided, the corresponding threshold current density

is derived to be $1.7\ kA/cm^2$. The performance of QD devices are not that ideal due to the size fluctuation and low dot density since the self-organisation technique inevitably induces some variation of the size and shape of dots. The inhomogeneous broadening of QDs deviates from the ideal structure, leading to a spread of localisation energy within a dot ensemble and the gain spectrum. Eventually, the maximum peak gain is reduced and the threshold current density becomes higher.

Table 2-1 Basic parameters derived from LI curve

Cavity length (μm)	Threshold current (mA)	Threshold current density (A/cm²)	Maximum output power (mW)
300	11.72	1699	1.9
350	9.87	1226	7.6
400	9.33	1014	16.1
600	10.31	747	31.6
800	11.95	649	48.6
1000	14.02	610	66.1

Similar parameters for other devices with different cavity lengths can be derived from the LI curves, and the results are summarised in Table 2-1. Since the threshold current is dependent on the size of the laser cavity, it is more sensible to use the threshold current density to compare the performance of laser devices of different sizes. It is found that threshold current density decreases monotonically from $1.7\ kA/cm^2$ for $L = 300\ \mu m$ to $0.6\ kA/cm^2$ for $L = 1000\ \mu m$. The lower threshold current density in longer cavity laser is clearly the results of the diminishing mirror losses based on the definition in Equation 1.2. With cavity lengths of $300\ \mu m$, the CW output power saturates at a power level of only several milliwatts. Then the total output power continues to increase as the cavity becomes longer and reaches $\sim 70\ mW$ for $1000\ \mu m$ length devices.
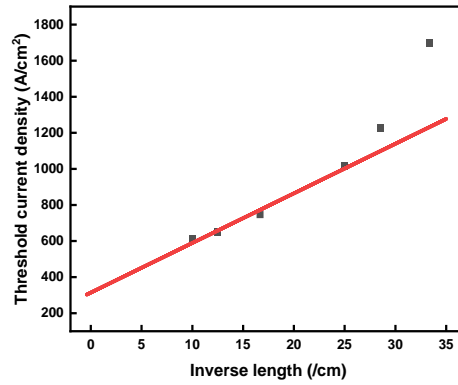
Figure 2.12: Threshold current density as a function of inverse cavity length.

Plotting J_{th} versus $\frac{1}{L}$ yields a straight line. The dependence of J_{th} on $\frac{1}{L}$ follows this line very well until $L = 400 \, \mu m$. The transparency current density obtained from the intercept of the line with the vertical axis gives the threshold current density of $313 \, A/cm^2$. However, it can be seen in Figure 2.12 that at short cavity length, the current density value diverges from the linearly fitting. This is due to the assumed linear relationship between gain and carrier density is only valid under low injection. For the short cavity length with higher threshold current density, the differential gain decreases with increasing carrier numbers [19, 20]. Thus, with the higher current density, a logarithmic function should be employed.

2.4.2   Length dependent characteristics

Length-dependent characterisation as described before was carried out based on the LI curves of the as-cleaved FP lasers. Based on the measured threshold current density for lasers with different cavity length, the transparency current density can be calculated. It is mentioned before that the value of the transparency current helps to determining the ultimate available threshold current for the material [21, 22]. Efficiency is a measurement of how well a device can convert the input current to lasing light power out of the laser. To assess the radiation efficiency of laser diodes, the SE, a quantity of practical interest, could be directly derived from the LI graph. It is defined as the ratio of the increase in light intensity ΔP_{out} to the increase in injection current ΔI.

$$SE = \frac{\Delta P_{out}}{\Delta I} \ (W/A) \qquad\qquad \textit{Equation 2.16}$$

It is mentioned before that lower threshold current is usually desirable from the power consumption consideration. Higher SE is preferred as well, which means that more light output is derived with less expenditure of current.

From the calculation of this gradient of the LI slope, the differential external quantum efficiency (DEQE, η_d), describing the conversion efficiency between the carriers and photons, could be further derived.

$$\eta_d = \frac{\Delta P_{out}/h\upsilon}{\Delta I/q} \qquad\qquad \textit{Equation 2.17}$$

The SE and calculated DEQE is list in table below. At relatively long cavity lengths (above 400 μm), the slope efficiency is reduced as the cavity length becomes longer. However, the short length devices show opposite tendency. This is due to the saturation limitations of QD laser.

<p align="center"><i>Table 2-2 Efficiencies calcualted from the LI curve</i></p>

Cavity length (µm)	Slope efficiency (W/A)	Differential external quantum efficiency
300	0.111	0.232
350	0.121	0.253
400	0.152	0.318
600	0.143	0.299
800	0.140	0.293
1000	0.135	0.283

The DEQE is usually used to evaluate the entire conversion from electrons to photons, while the internal quantum efficiency (IQE, η_{int}) phenomenologically indicates the transformation rate inside the active region. When deducing the IQE from DEQE, the output coupling efficiency should be considered. The total loss inside active region mainly falls into internal loss α_i and mirror loss α_{mir} while the output power is generated by the photon escape from the cavity. The η_{int} can be derived as,

$$\eta_{int} = \frac{\alpha_{mir} + \alpha_i}{\alpha_{mir}} \eta_d \qquad\qquad \textit{Equation 2.18}$$

Based on the SE directly derived from LI curve, DEQE and mirror loss can be calculated, provided the wavelength and cavity length are known. However, the internal loss and internal quantum efficiency, which are direct indicators of the quality of the semiconductor crystal material, cannot be derived from a single laser. In order to obtain these two parameters, it is required to measure the lasers with different cavity length but the same reflectivity. The DEQE and mirror loss in Equation 2.18 can be measured and calculated. By varying the cavity length, other two knowns α_i and η_{int} can be derived as,

$$\frac{1}{\eta_d} = \frac{1}{\eta_{int}}[1 + \frac{\alpha_i}{\ln(\frac{1}{R})}L]$$ *Equation 2.19*

The internal optical losses are dominated by carrier density dependent absorption while the differential internal efficiency above threshold is found to be mainly restricted by carrier recombination losses [14]. In lasers with short cavity length, relatively high threshold current density, corresponding to higher carrier density, will enhance both the loss mechanisms described above. As a result, in the following calculation, it is more accurate to use the thresholds of longer length lasers as they are still in the linear region from 400 μm. It is assumed that these devices are operating in the linear region, so that η_i and α_i do not depend on the laser length.

Figure 2.13 plots the relation between the reciprocal of external quantum efficiency and cavity length. The differential external quantum efficiency reaches a value of 31.8% for a cavity length of 400 μm and decreases to 28.3% at a cavity length of 1000 μm. The internal efficiency of 34.3% was derived from the reciprocal of intercept point. The value of the internal loss coefficient calculated from the gradient is 2.53/cm.
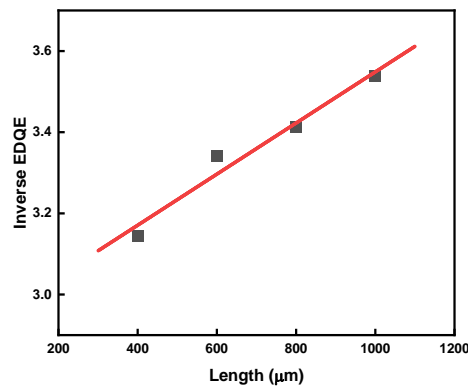
Figure 2.13: Inverse external differential quantum efficiency as a function of cavity length

With the internal loss known, the overall modal gain can be calculated by the sum of internal loss and mirror loss. At each cavity length, the corresponding modal gain for the threshold current density can be obtained and plotted as follows. We further fitted this relationship with logarithmic function [23].
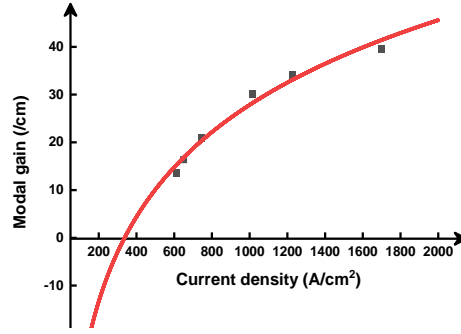
Figure 2.14: Gain as a function current density.

In Figure 2.14, the logarithmic relationship between modal gain and injection current is obvious and reasonable. This is the results of both the gain saturation in subbands and impact of Auger recombination. The curve also demonstrates a trend toward saturation at a current above $2\ kA/cm^2$ as predicted. The gain current relation can be mathematically approximated,

$$g = g_0 \ln \left(\frac{J}{J_{tr}} \right) \qquad\qquad \textit{Equation 2.20}$$

Solid curve is given for quantities calculated from the theoretical model. From the fitted curve, the transparency current density can be estimated as $337\ A/cm^2$, which is slightly higher than the previous linear estimation.

2.4.3 Temperature dependent characteristics

Having successfully achieved the breakthrough regarding the QD growth and related device fabrication, much effort has been made to realise the theoretical expectation of the superior temperature characteristics in lasers. In real applications, both the high temperature resistance and temperature insensitivity are required. According to the resource findings such as mineral in deep underground or mobile applications, temperature of the ambient can reach as high as 200 °C,

which is destroying for common laser operation. Additionally, the starting temperature may be quite low even in the negative degree range.

Fundamentally, due to the discrete electronic levels brought forth by the decreased dimensionality of the free electron motion and deep confinement potentials, QD lasers under ideal conditions should offer high T_0 [24]. This predicted high characteristic temperature in QD lasers has opened new markets [25]. However, temperature sensitivity still occurs due to inhomogeneous broadening and small separation between energy levels in valence band. When the barrier height is too low, thermionic emission of carriers from the confined region to the barriers will lead to an increase of the threshold current because of leakage currents [26]. Such variations have impact on the crucial parameters, such as the emission wavelength, efficiencies, and threshold conditions. Temperature dependent loss effects have been intensively discussed in the literature [27]. The temperature dependence of threshold current density is sensitive to both the form of the density of states and the carrier distribution functions [28].

Generally, as temperature increases, the threshold current increases and efficiencies decrease. Several mechanisms result in the degraded performance of laser at high temperature, such as Auger recombination, free carrier absorption (FCA), thermal hole spreading, etc. The threshold current density can be empirically expressed as an increased exponential function with temperature, that is,

$$J_{th} = J_0 \exp\left(\frac{T}{T_0}\right) \qquad \text{\textit{Equation 2.21}}$$

T_0 is a characteristic temperature, which is used to indicate the temperature sensitivity of device. A higher T_0 results in a smaller dJ_{th}/dT, namely, better thermal insensitivity. To determine T_0, LI curves of laser were illustrated over a range of temperatures. The threshold current density obtained from these measurements are plotted logarithmically against the temperature. The characteristic temperature is then determined by the slope of the linear fit line. For InGaAsP/InP lasers, T_0 is typically in the range of 50-70 K (25 °C-65 °C). The low T_0 and thus poor temperature stability require the complex and costly system, including thermoelectric cooler, power monitoring and feedback indispensable. By contrast, T_0 exceeds 160 K (25 °C-80 °C) for AlGaAs/GaAs lasers. With this temperature insensitivity, operation can be extended into the temperature range required for commercial devices (-40 °C-85 °C). Indeed, several techniques

have been investigated to improve the temperature characteristic, including modulation p-doping and band offset adjustments.

As mentioned in previous chapter, 6 nm GaAs layer with Be modulation doping is employed in the GaAs spacer layer. The LI curves for the fabricated devices with cavity length above 400 μm were measured over a range of temperatures under CW operation.
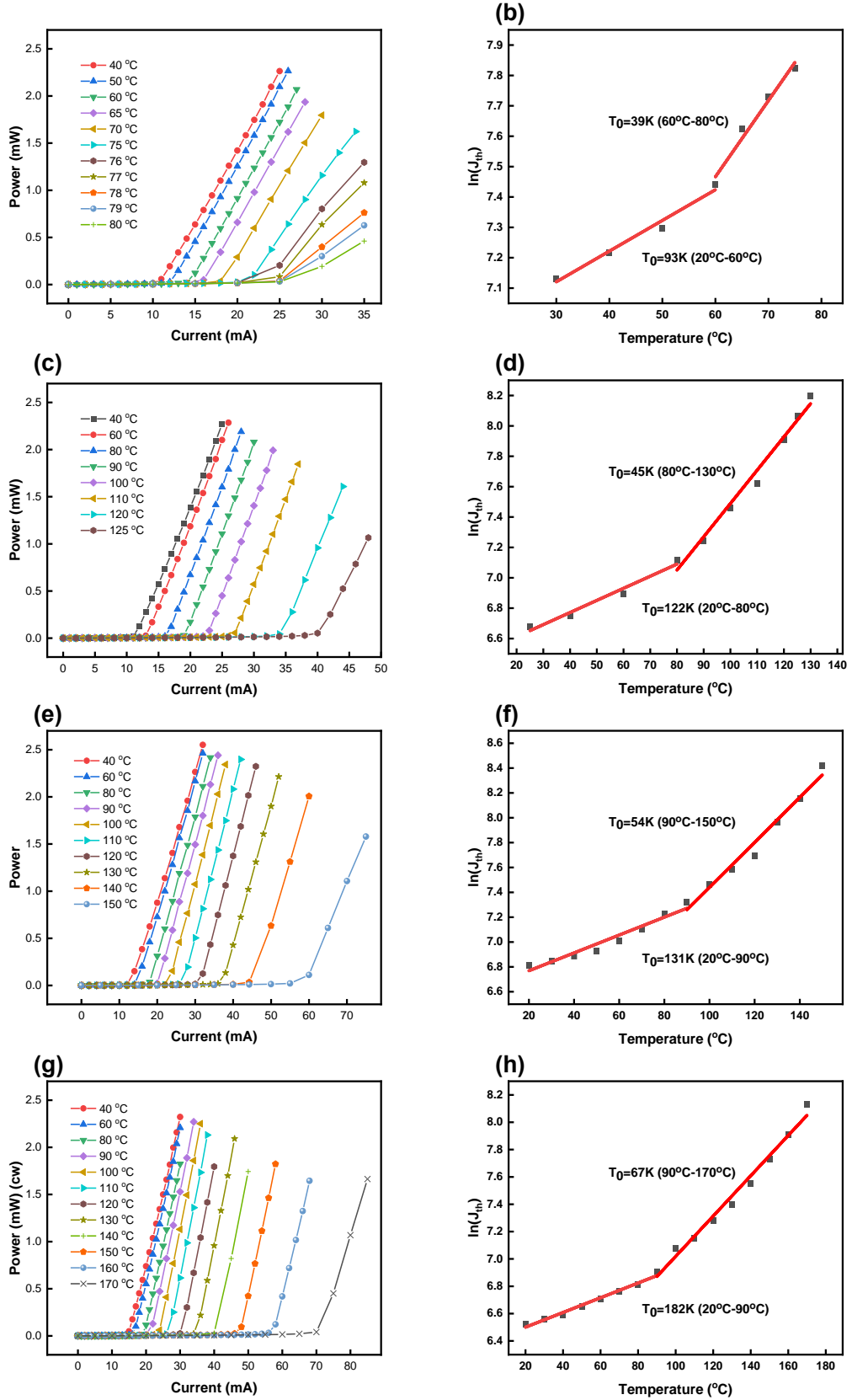
Figure 2.15: Tempreature dependent light current curve and characterstics temperature of different cavity length (a) (b) 400 µm, (c) (d) 600 µm, (e) (f) 800µm and (g) (h) 1000 µm.

Figure 2.15 shows the LI characteristics as a function of heat-sink temperature in CW mode of operation of different length lasers. In general, the longer devices show better temperature insensitivity, regarding both the maximum operation range and the characteristic temperature. At room temperature, the threshold current for 400 μm length laser is around 10 mA with a slope efficiency of 0.152 W/A. These values remain stable up to 60 °C with slight increase in threshold current and reduced efficiency. However, further elevation in operating temperature exceeding 75 °C brings degradation in efficiency while the threshold current doubles the value compared with the room temperature operation. The relative low characteristic temperature is obtained from Figure 2.15 (b) as only 93 K from 20 °C to 60 °C. For the devices with 1000 μm length, the threshold currents were measured to be 15 mA and 30 mA at the temperature of below 60 °C and 120 °C, respectively, as shown in Figure 2.15 (g). Figure 2.15 (h) reveals that the characteristic temperatures are 182 K (up to 90 °C) and 67 K (from 90 to 170 °C). The maximum operating temperature, slope efficiency and characteristic temperature are summarised in Table 2-3.

Table 2-3 Temperature characterisitcs

Cavity length (μm)	Max. operating temperature (°C)	Slope Efficiency (W/A)	Characteristic temperature
400	80	0.152 @ 20 °C	93K (20-60 °C)
		0.113 @ 75 °C	39K (60-80 °C)
600	125	0.143 @ 20 °C	122K (20-80 °C)
		0.139 @ 125 °C	45K (80-125 °C)
800	150	0.140 @ 20 °C	131K (20-90 °C)
		0.125 @ 150 °C	54K (90-150 °C)
1000	170	0.135 @ 20 °C	182K (20-90 °C)
		0.119 @ 170 °C	67K (90-170 °C)

The maximum operation temperature for devices with different lengths are 80 °C (400 μm), 125 °C (600 μm), 150 °C (800 μm), and 170 °C (1000 μm) and their slope efficiencies decrease gradually from room temperature to higher operating temperature. This reduction in quantum efficiency is mainly due to the thermally activated carriers from the ground energy state to the wetting layers and barrier potentials [29]. Furthermore, the nonradiative Auger recombination and

free carrier absorption increase the internal loss as well [30].

Due to the limited surface density of single-layer QD, gain saturation or excited state lasing occurs at high injection and high temperature [31, 32]. One of the solutions is the multiple stacking of the QDs. However, the accumulated high strain will cause degradation in practice [33]. The ability to incorporate large number of QD layers without compromising other performance of lasers remains as a formidable challenge. Another technique that could improve the temperature characteristic of QD materials is p-doping [34-36]. With the injection of extra holes in valence band, the thermally escaped holes can be compensated, and therefore the QD laser performance is improved.

It is verified theoretically and experimentally that lasers with longer cavity has a better performance at high operation temperature. The LI curve of 1000 μm length device at a large injection current range up to 300 mA as a function of heat-sink temperature is presented.
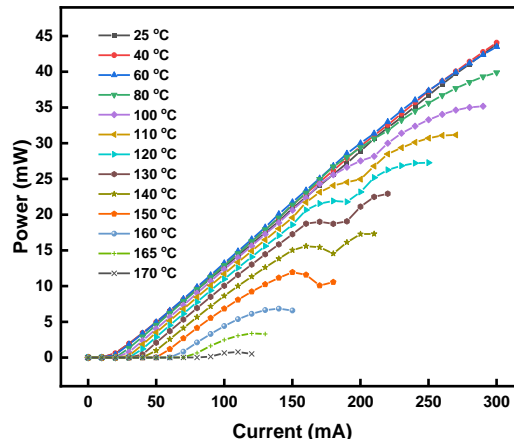
Figure 2.16: LI characteristic as a function of heat-sink temperature for 1000 μm as-cleaved FP QD laser.

Up to 60 °C, the output power reaches 45 mW at an injection current of 300 mA. Then, the maximum output power decreases, and the rollover starts to appear with maximum power of 40 mW at 80 °C. For even higher temperature, the lasing of ES occurs, corresponds to the kink in the LI curve. At 100 °C, the output power slightly decreases at around 210 mA and then continuously increases, eventually reaching 35 mW at 300 mA. The maximum output power of 10 mW is achieved with QD laser operating at relatively high temperature of 150 °C.

A larger T_0 can be achieved by engineering the energy separation between the GS and first ES.

In fact, the energy separation of the electron energy is enough to achieve high temperature operation with a typical value around 75 to 80 meV [37]. In contrast, the separation between hole levels remains a limitation. Although the injected electrons may reside in the GS in the CB, the holes are thermally broadened to the high energy levels in the VB. As a result, the superior insensitivity of temperature in QD lasers is inhibited. Theoretically, p-type modulation doping can substantially increase the GS gain in QD laser by providing excess holes in the active region[38, 39]. Then, the closely spaced hole energy levels, filled with extra holes, provide the ground states transition [40].

Another source of temperature dependent operation is the inevitable inhomogeneous broadening arising from the size fluctuation of the QD [41]. A sizable fraction does not contribute to the useful lasing. It is also supposed that the degradation of temperature stability results from the internal loss brought by FCA and Auger recombination related to defects and impurities. The superlattice barriers may be used to increase the carriers confinement and improve the temperature characteristics of QD laser [42]. The carriers are reflected by the superlattice due to an increased effective barriers height. When the barrier height is too low, the thermionic emission of carriers from the QW to the barriers will lead to an increase of the threshold current because of leakage current.

2.5 Conclusion

In this section, the measurement and description of the static characteristics of QD laser is given. Based on the LI curve, the threshold current, slope efficiency and external quantum efficiency can be read or calculated directly. More intrinsic physical properties include the internal loss, internal quantum efficiency, gain characteristics and transparency current can be derived by measuring the LI curve of lasers with different cavity length. QD laser has a low threshold current and low transparency current on the whole. Its modal gain can be improved by increasing the number of the layer and dot density.

We also measured the LI curve at different temperatures and the characteristic temperature are derived by plotting the logarithmic threshold current density versus the operating temperature.

It is obvious that lasers with longer cavity lengths have a better temperature stability while it gives larger maximum output power, high maximum operating temperature and greater characteristic temperature value.

Reference

1.   Farrow, R.F., *Molecular beam epitaxy: applications to key materials*. 1995: Elsevier.

2.   Pan, S., et al., *Quantum dot mode-locked frequency comb with ultra-stable 25.5 GHz spacing between 20°C and 120°C.* Photonics Research, 2020. **8**(12): p. 1937-1942.

3.   Lu, Y., et al., *Analysis of the regimes of feedback effects in quantum dot laser.* Journal of Physics D: Applied Physics, 2022. **55**(48): p. 484003.

4.   https://www.nist.gov/programs-projects/scanning-probe-microscopy-advanced-materials-and-processes. *Scanning Probe Microscopy for Advanced Materials and Processes*.

5.   University, R.A., *Atomic Force Microscopy -An advanced physics lab experiment.* 2014.

6.   Kittel, C., *Introduction to solid state physics Eighth edition.* 2021.

7.   Scimeca, T., et al., *Surface oxidation of selenium treated GaAs (100).* Journal of Vacuum Science & Technology B: Microelectronics and Nanometer Structures Processing, Measurement, and Phenomena, 1994. **12**(6): p. 3090-3094.

8.   Baca, A. and C. Ashby, *Fabrication of GaAs Devices*. 2005: Institution of Engineering and Technology.

9.   Malina, V., et al., *Non-alloyed Ti/Au and Ti/Pt/Au ohmic contacts to p-type InGaAsP.* Thin Solid Films, 1993. **223**(1): p. 146-153.

10.   Cox, R.H. and H. Strack, *Ohmic contacts for GaAs devices.* Solid-State Electronics, 1967. **10**(12): p. 1213-1218.

11.   Kim, T.J. and P.H. Holloway, *Ohmic contacts to GaAs epitaxial layers.* Critical Reviews in Solid State and Materials Sciences, 1997. **22**(3): p. 239-273.

12.   Shih, Y.C., et al., *Effects of interfacial microstructure on uniformity and thermal stability of AuNiGe ohmic contact to n-type GaAs.* Journal of Applied Physics, 1987. **62**(2): p. 582-590.

13.   Piprek, J., P. Abraham, and J.E. Bowers, *Cavity length effects on internal loss and quantum efficiency of multiquantum-well lasers.* IEEE Journal of Selected Topics in Quantum Electronics, 1999. **5**(3): p. 643-647.

14.   Ustinov, V.M., et al., *Quantum dot lasers*. Vol. 11. 2003: Oxford University Press on Demand.

15.   Asada, M., Y. Miyamoto, and Y. Suematsu, *Gain and the threshold of three-dimensional quantum-box lasers.* IEEE Journal of Quantum Electronics, 1986. **22**(9): p. 1915-1921.

16.   Asada, M., Y. Miyamoto, and Y. Suematsu, *Gain and the threshold of three-dimensional quantum-box lasers*.

17.   Asada, M., Y. Miyamoto, and Y. Suematsu, *Theoretical Gain of Quantum-Well*

Wire Lasers. Japanese Journal of Applied Physics, 1985. **24**(Part 2, No. 2): p. L95-L97.

18.   Kim, J.K., et al., *Design parameters for lateral carrier confinement in quantum-dot lasers.* Applied Physics Letters, 1999. **74**(19): p. 2752-2754.

19.   Arakawa, Y. and A. Yariv, *Theory of gain, modulation response, and spectral linewidth in AlGaAs quantum well lasers.* IEEE Journal of Quantum Electronics, 1985. **21**(10): p. 1666-1674.

20.   Derry, P.L., et al., *Ultralow threshold graded-index separate-confinement heterostructure single quantum well (Al,Ga)As lasers.* Journal of Vacuum Science & Technology B: Microelectronics Processing and Phenomena, 1988. **6**(2): p. 689-691.

21.   Chen, T.R., et al., *Experimental determination of transparency current density and estimation of the threshold current of semiconductor quantum well lasers.* Applied Physics Letters, 1990. **56**(11): p. 1002-1004.

22.   Yariv, A., *Scaling laws and minimum threshold currents for quantum-confined semiconductor lasers.* Applied Physics Letters, 1988. **53**(12): p. 1033-1035.

23.   Wilcox, J.Z., et al., *Gain- and threshold-current dependence for multiple-quantum-well lasers.* Journal of Applied Physics, 1988. **64**(11): p. 6564-6567.

24.   Arakawa, Y. and H. Sakaki, *Multidimensional quantum well laser and temperature dependence of its threshold current.* Applied physics letters, 1982. **40**(11): p. 939-941.

25.   Schäfer, F., et al., *High-temperature properties of GaInAs/AlGaAs lasers with improved carrier confinement by short-period superlattice quantum well barriers.* Applied Physics Letters, 1998. **73**(20): p. 2863-2865.

26.   Hu, S.Y., et al., *Temperature-dependent threshold and modulation characteristics in InGaAs/GaAs quantum-well ridge-waveguide lasers.* Applied Physics Letters, 1995. **66**(16): p. 2040-2042.

27.   Menzel, U., et al., *Modelling the temperature dependence of threshold current, external differential efficiency and lasing wavelength in QW laser diodes.* Semiconductor Science and Technology, 1995. **10**(10): p. 1382-1392.

28.   Hess, K., et al., *Temperature dependence of threshold current for a quantum-well heterostructure laser.* Solid-State Electronics, 1980. **23**(6): p. 585-589.

29.   Ozgur, G., A. Demir, and D.G. Deppe, *Threshold Temperature Dependence of a Quantum-Dot Laser Diode With and Without p-Doping.* IEEE Journal of Quantum Electronics, 2009. **45**(10): p. 1265-1272.

30.   Gupta, N., et al., *Temperature-Independent Performance of an 8-Layer λ ~1.3 µm InAs/GaAs Quantum-Dot Laser.* Journal of Russian Laser Research, 2020. **41**(1): p. 86-93.

31.   Xiaodong, H., et al., *Very low threshold current density room temperature continuous-wave lasing from a single-layer InAs quantum-dot laser.* IEEE Photonics Technology Letters, 2000. **12**(3): p. 227-229.

32.   Liu, H.Y., et al., *High-performance three-layer 1.3-µm InAs-GaAs quantum-dot lasers with very low continuous-wave room-temperature threshold currents.* IEEE Photonics Technology Letters, 2005. **17**(6): p. 1139-1141.

33.   Shimizu, H., et al., *Comparison between multilayered InAs quantum dot lasers with different dot densities.* Applied physics letters, 2006. **88**(24): p. 241117.

34.   Shchekin, O.B. and D.G. Deppe, *Low-threshold high-T_0 1.3-μm InAs quantum-dot lasers due to p-type modulation doping of the active region.* IEEE Photonics Technology Letters, 2002. **14**(9): p. 1231-1233.

35.   Liu, H., et al., *p-doped 1.3 μm In As ∕ Ga As quantum-dot laser with a low threshold current density and high differential efficiency.* Applied Physics Letters, 2006. **89**(7): p. 073113.

36.   Sandall, I., et al., *The effect of p doping in InAs quantum dot lasers.* Applied physics letters, 2006. **88**(11): p. 111113.

37.   Shchekin, O.B., et al., *Discrete energy level separation and the threshold temperature dependence of quantum dot lasers.* Applied Physics Letters, 2000. **77**(4): p. 466-468.

38.   Singh, J., *Strain distribution and electronic spectra of InAs/GaAs self-assembled dots: An eight-band study.*

39.   Shchekin, O.B. and D.G. Deppe, *1.3 μm InAs quantum dot laser with To=161 K from 0 to 80 °C.* Applied Physics Letters, 2002. **80**(18): p. 3277-3279.

40.   Shchekin, O.B. and D.G. Deppe, *The role of p-type doping and the density of states on the modulation response of quantum dot lasers.* Applied Physics Letters, 2002. **80**(15): p. 2758-2760.

41.   Asryan, L. and R. Suris, *Inhomogeneous line broadening and the threshold current density of a semiconductor quantum dot laser.* Semiconductor science and technology, 1996. **11**(4): p. 554.

42.   Klotzkin, D. and P. Bhattacharya, *Temperature dependence of dynamic and DC characteristics of quantum-well and quantum-dot lasers: A comparative study.* Journal of lightwave technology, 1999. **17**(9): p. 1634.

3   Dynamic characteristics

Optical gain material based on quantum dot (QD) offers advantages from the discrete delta function-like density of states. The improved static characteristics of low threshold and temperature insensitivity have been verified in previous chapter. In addition to the static characteristics, developing high-speed lasers is of great importance for the application of high-speed digital data transmission [1-4]. In other words, it is crucial to theoretically analyze the dynamical parameters and characterize their performance under small and large signal modulation. In this regards, the use of QDs as a gain material offers superior dynamical properties which stem from the predicted large differential gain and low linewidth enhancement factor (LEF) of QDs [5]. However, the maximum bandwidth reported for QD laser at room temperature is only around 10 GHz, which is inferior to the quantum well (QW) counterparts [6-8].

In order to improve the dynamic characterisation and thus realise the predicted performance of QD lasers, it is necessary to clarify the impacting factors of the modulation bandwidth in QD Fabry Perot (FP) lasers first. The carrier-photon oscillations give an insight to the inherent dynamic speeds of the laser, as they are a measure of the maximum rate at which the material can convert carriers to photons and vice versa via its recombination mechanisms. Moreover, the photon and carrier densities can also be altered due to quantum fluctuations associated to the lasing process[9]. Variations in photon and carrier densities lead to changes in the output power intensity and the frequency/phase of the optical field, respectively. Lowering the intensity noise in optical sources helps reducing the bit error rate (BER) in broadband data systems.

In this chapter, we will first analyze the relative intensity noise (RIN) of QD lasers and predict the limited bandwidth due to the damping factor based on the intensity spectra. Then, the small signal response and eye diagram under large signal modulation are provided. By varying the injection current, the corresponding 3 dB bandwidth and modulation efficiency are derived.

Although it is predicted that laser with shorter cavity should give a better modulation bandwidth, in our measurement, the 200 μm and 600 μm devices show the similar bandwidth as a result of the lack of proper electrical design.

3.1 Fundamentals of dynamic characteristics

The rate equations have been used to analyze the static characteristic in chapter 2. This method can also be employed in the dynamical region. In this section we will first utilise rate equations to theoretical predicted the intrinsic bandwidth of directly modulated laser. Then the basics of intensity noise originated from spontaneous emission is provided.

3.1.1   Directly modulated laser

In the dynamical system, as N_e increases, N_p will increase in time due to enhanced gain. Each stimulated photon consumes an electron-hole pair and thus decreases N_e. With the reduction in N_e, N_p subsequently begins to fall due to the lack of carries, meanwhile the further injected current replenishes the N_e. The cycle between N_e and N_p repeats itself automatically and produces a natural resonance between the input and output. The detailed understanding of the intrinsic frequency response of semiconductor lasers and the effect of the device's electrical parasitics are of considerable interest as an aid to the design of very high-speed lasers. Small signal modulation is a measure of how fast the real laser is capable of operating at. For this measurement, a laser is modulated with small modulation depth, which allows evaluation of the laser's response without non-linear effects, such as thermal heating, gain saturation, and spatial and spectral hole burning.

The inference of small signal response goes back to the basic rate equations as well. Similar to the static circumstances, the dynamical response of carries and photons to the perturbation equals the time derivatives of the generation terms minus the consumption terms.

$$d\left(\frac{dN_e}{dt}\right) = \frac{\eta_i}{qV} dI - \frac{1}{\tau_e'} dN_e - (v_g g dN_p + v_g N_p dg) \qquad \text{Equation 3.1}$$

$$d\left(\frac{dN_p}{dt}\right) = (\Gamma v_g g dN_p + \Gamma v_g N_p dg) + \frac{\Gamma}{\tau_{sp}'} dN_e - \frac{1}{\tau_p} dN_p \qquad \text{Equation 3.2}$$

where τ_e' is the differential carrier lifetime, which is typically two to three times smaller than τ, and τ_{sp}' is the differential lifetime of carriers that radiate photons by spontaneous emission into the lasing mode [10]. Since the gain is known to be impacted by both electron and photon density, its variation can be further expanded as,

$$dg = a dN_e - a_p dN_p \qquad \text{Equation 3.3}$$

$$a = \frac{a_0}{1 + \varepsilon N_p} \qquad \text{Equation 3.4}$$

$$a_p = \frac{\varepsilon g}{1 + \varepsilon N_p} \qquad \text{Equation 3.5}$$

where a_0 is the nominal differential gain and ε is the gain compression factor. The expression of Equation 3.3 is based on the fact that the gain increases as the carriers accumulate, while is compressed with higher photon density.

Under perturbation, both the density of carriers and photons deviate from steady state in relatively subtle value. Sinusoidal functions are usually accommodated to express the small signal response among I, N_e and N_p.

$$I = I_0 + I_1 e^{j\omega t} \qquad \text{Equation 3.6}$$

$$N_e = N_{e0} + N_{e1} e^{j\omega t} \qquad \text{Equation 3.7}$$

$$N_p = N_{p0} + N_{p1} e^{j\omega t} \qquad \text{Equation 3.8}$$

As the direct current (DC) is sufficiently far above threshold, the spontaneous emission can be neglected. Applying these to Equation 3.1, Equation 3.2 and Equation 2.15 can generate frequency domain equations and solve for the transfer function.

$$\frac{P(\omega)}{I(\omega)} = \frac{\eta_d h\upsilon}{q} \cdot \frac{\omega_R^2}{\omega_R^2 - \omega^2 + j\omega\gamma} \qquad \text{Equation 3.9}$$

$$\omega_R^2 \approx \frac{v_g a N_{p0}}{\tau_p} \qquad \text{Equation 3.10}$$

$$\gamma = K f_R^2 + \gamma_0 \qquad \text{Equation 3.11}$$

where ω_R is the natural resonance frequency. Based on the rate equation in dynamical range, the mutual dependence of N_e and N_p is founded as above. Initially, the response increases with frequency and reaches peak with an enhancement existing at the relaxation oscillation frequency. Afterwards, the modulation response is limited and drops off. However, other limitations, including

damping factor and electrical constant, should be considered for the actual modulation response. The real resonance is always less than calculated ω_R, and sometimes there is even no evident peak.

After discussing the static and dynamic characteristics of single laser diode, we could move to the design of the system. The conversion between electrical information and optical signal with the same information plays a prior role in designing the optical communication system [11]. There are mainly two techniques used in generating the corresponding optical bit stream: direct modulation and external modulation. The direct modulation is directly manipulating the input current or biasing the laser with constant current. In contrast, the external modulation is alternating the output separately by external modulator [12].
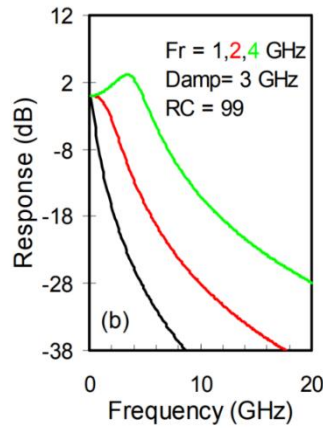
Figure 3.1: Variation in small signal modulation response depending on damping factor.

In the real world, parasitic resistance and capacitance are introduced to the structure, due to the bond pads to a laser for electrical contact, non-zero thickness of device, etc. Excessive resistance-capacitance (RC) transport contacts affect the modulation bandwidth directly. Typically, in the device with high resistance, it usually takes few picoseconds for the injected carrier to make its way to go through the low-doped regions and gets to the active layers. This diffusion gets longer with exceptionally thick cladding. The dynamical performance of laser is limited by the resistance and capacitance (associated with the blocking layers, metallisation layers and junction) and the resultant modulation response could be regarded as a single-pole, low-pass RC-filter.
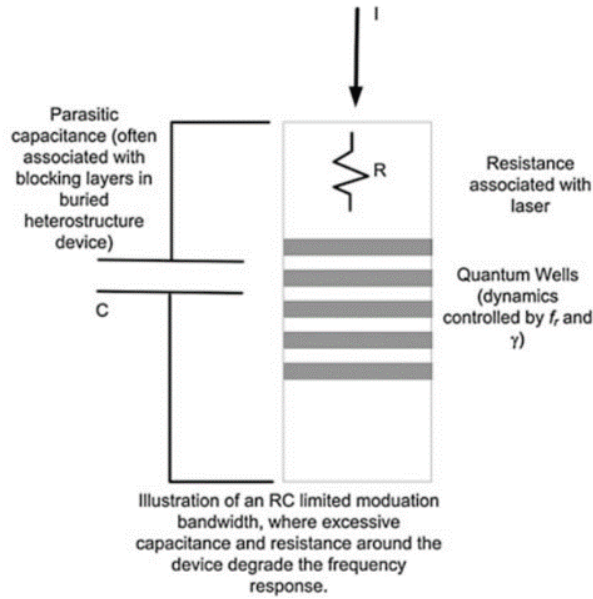
Figure 3.2: Illustration of RC limited bandwidth.

Since the small signal response of semiconductor laser is impacted by both the intrinsic frequency and the electrical properties of the devices such as resistance and capacitance. The frequency response of a laser diode is then modified as

$$|H(\omega)| = \frac{\omega_R^2}{\sqrt{(\omega_R^2 - \omega^2)^2 + \omega^2\gamma^2}} \cdot \frac{1}{\sqrt{1 + (\omega CR)^2}} \qquad \text{Equation 3.12}$$

Due to the impact of RC parasitic, the resistance and capacitance for each device are statically measured before the commencement of small signal modulation. Knowing these parameters allowed deconvolution of their components from the final frequency response to find the true laser response. In this thesis, I focus mainly on the semiconductor materials and the electrical constants cannot be carried out due to the lack of laboratory apparatus.

3.1.2 Relative intensity noise

In steady state where the injected current is constant, the carrier and photon densities should remain stably unchanged. However, even under no deliberate current modulation, random carrier fluctuation, such as spontaneous emission into the lasing mode, produces instantaneous time variations in the carrier and photon densities. The fluctuations lead to undulation in the optical power intensity, which provides a noise floor and brings broadening in spectral characteristics [13].

We also need to consider the optical feedback noise when the laser is applied to systems. Since all these noises degrade the performance of devices and also have impact on the whole transmission systems, the analysis, estimation and improvement of the noise characteristics are important [14].

Spontaneous emission is one of the dominate noises generated in semiconductor lasers due to the random direction of the photons. The coherence field is perturbed both in amplitude and phase by the spontaneously emitted photons. The RIN of the laser is a measure of the ratio of optical intensity noise over a particular bandwidth to the average overall optical intensity [15, 16].

$$RIN = \frac{\langle \Delta P^2 \rangle}{P^2} \ (dB/Hz) \qquad \qquad \textit{Equation 3.13}$$

$\langle \Delta P^2 \rangle$ is the mean squared optical intensity fluctuation and P^2 is averaged optical output power squared. The unique unit dB/Hz is due to the fact that RIN is usually averaged in a limited range of frequency. RIN is regarded as an essential feature to realise high signal-to-noise ratio (SNR) in optical communication systems, community antenna television (CATV) and mobile communication[17]. In laser, RIN can be used to characterize the key parameters[18]. From the noise intensity plotted as a function of frequency, the value of RIN is considerably enhanced around the resonance frequency f_R and drops rapidly for $f \gg f_R$, since the laser is not able to response to the variations at such high frequencies. By increasing the injection current, the carrier intensity and RIN will change. The number of carrier available for the recovery process becomes faster and hence the relaxation resonance peak increases, till the system reaches its intrinsic recovery speed. From more mathematic view, it is found out that RIN decreases with an increase of P^{-3} dependence in power at low frequency and P^{-1} dependence at high powers. The RIN spectrum can further be modelled for the derivation of damping factor [7, 19].

$$RIN = \frac{Af^2 + B}{(f^2 - f_R^2)^2 + f^2 \gamma^2} \ (dB/Hz) \qquad \qquad \textit{Equation 3.14}$$

where A and B are fitting constants and γ is damping factor. RIN calculated from the system is always higher than the laser RIN, due to the presence of other noise, such as thermal noise arising from heating of carriers in electronic systems and shot noise originating from the carrier fluctuations with an applied voltage. As the output of laser consists of several modes, even for the DFB lasers, mode partition noise needs to be considered. It is possible that the total intensity noise remains quite stable while there is large intensity deviation exhibited in the individual modes [20].

3.2 Experimental methods

The measurements of the dynamical properties of QD laser is more complex than the static characteristics. Special submount is needed for the small signal modulation measurement, and in our experiment, commercial submount for 25 GHz distributed feedback (DFB) QW laser is employed. The laser is mounted n-side down on the Au-plated ceramics carriers while the p-side is connected with bond wire, as shown in Figure 3.3.
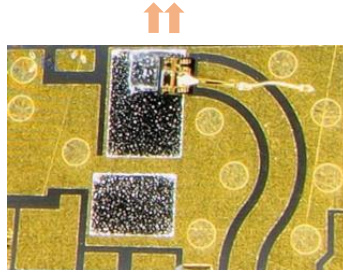
Figure 3.3: Packaged laser for small signal response measurement.

The small signal modulation response of the laser was measured using a Hewlett-Packard 8350B sweep oscillator, low noise amplifier, New Focus high speed detector, and a Hewlett-Packard 8562A spectrum analyzer. Before carrying out the small signal measured, the calibration of measuring system are performed without the connecting the laser. Then the laser is forward biased and applied by the perturbation of the voltage. Its frequency response is determined by measuring the S_{21} scattering parameters.
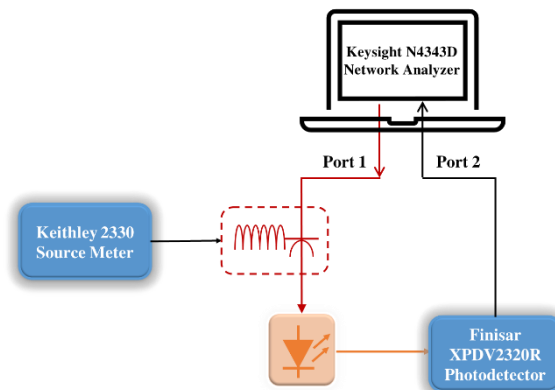
Figure 3.4: Small signal response setup.

The small signal response gives only theoretical estimation of the direction modulation

performance. What is really relevant for most applications and standards is the properties under large signal modulation. Regarding the assessment of high-speed digital signal transmission, eye diagram is employed as a key method to visualize the performance and determine the key parameters.

Figure 3.5: Example of eye diagram and its relationship of BER and decision level [21].

The data eye diagram is constructed by repeatedly folding the waveform and displayed in a single graph. Overlaps of each individual bit '1' and '0' compose the upper and lower eyelid. Ideally, only the time domain waveform is shown in the resemble eye. While in real situation, impai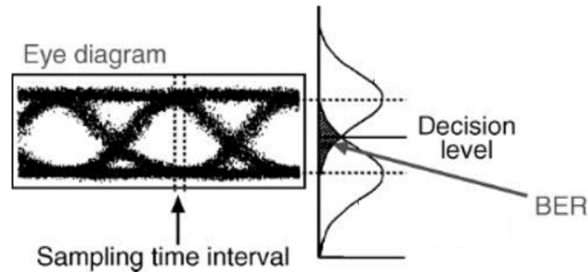rments, such as attenuation, crosstalk and noises, arising from the high-speed digital systems affect the resultant eye diagrams. During the measurements, low-pass filter with bandwidth just below relevant gigabit is used to suppress the inherent ring and overshoot. Additionally, automation of instruments is developed to simplify the test. Measurements of rise times, fall times, jitter, overshoot as well as extinction ratio (ER) are considered important when characterizing an eye. Many other numerical descriptions can be made depending on eye behavior. The small signal parameters could be related to the large signal pattern by these results. Moreover, eye diagram can also reveal the influence of parameters, such as damping factor, capacitance and resistance. As a whole, eye diagram gives an intuitive view of parametric performance together with the numerical data, which helps optimizing the laser transmission. Apart from the accessible visualisation from eye diagrams, the quantity judgement about faithfully passing each bit is pivotal. The BER is a ratio between the number of correctly received bits and transformed bits [22].

The measurement of RIN describes the ratio between the intensity fluctuation and overall output power. The maximum available amplitude range for signal modulation is given by this value. In the RIN measurement systems, the ratio of the optical power is considered equivalent to the detected electrical powers while the value of the output power can be derived straightforward and noise characteristics is more complex.

When measuring the noise, several factors need to be noticed. Typically, the noise at the optical receiver consists of three basic contributions: intensity noise in laser, thermal noise in electronics and shot noise. The shot noise is a function of intensity depending on the photodiode while thermal noise and laser intensity noise vary with frequency. At a given temperature, thermal noise can be considered as a constant value, while very low noise amplifiers are often added after the photodiode to reduce the thermal noise contribution. When dealing with the thermal noise, we could directly regard it as the noise in the turn-off state. However, shot noise is introduced by the quantum nature of photons arriving at the detector and thus is related to the detection statics. The mean-squared noise current from the photodetector is denoted as $\langle i_n^2 \rangle = 2qI_{dc}B$. If the average power is quite low, the thermal noise is the main limiting factor when measuring the RIN while shot noise becomes the measurement limit when the average power is large enough.
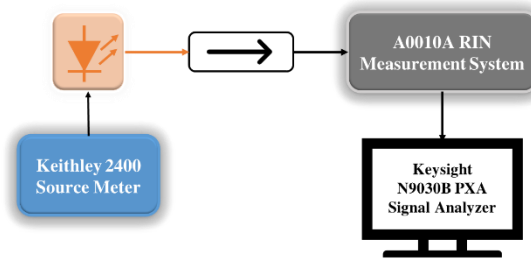
Figure 3.6: Experimental setup of RIN measurement.

The experimental setup is shown in Figure 3.6. The A0010A RIN measurement system was used. It is a quite function-packaged equipment inside which a unique and accurate calibration is included in the device. Thus, there is no need to extract the RIN from the total noise. Laser under test was biased by probes and its output was coupled to the single mode fiber with 80° angle. An isolator was then used to prevent the feedback noise. The radio frequency (RF) output of A0010A was connected to the signal analyzer from which the noise spectrum was displayed.

3.3 Small signal modulation measurements

The large bandwidth is expected in the QD lasers due to its predicted high differential gain [23-26]. In practice, however, the related bandwidth is inferior to their full potential, especially

regarding the dynamic characteristics [8, 27]. To find the strategy for improving the modulation bandwidth compatible with the network's requirement, it is necessary to clarify the origin of limitation in the QD lasers first. It is known that both the inhomogeneous gain broadening and large gain compression in QD contribute to the degradation of modulation bandwidth of QD lasers [28-31]. The impact of p-type doping on enhancing modulation bandwidth of QD lasers has been theoretically analysed and experimentally demonstrated in [32, 33].

In this work, the small signal response of the QD lasers were measured, from which a detailed understanding of the intrinsic frequency response was further analysed. For each cavity length, the small signal response was plotted as a function of injection current. Firstly, the 200 μm length device under different injection current range from 10 mA to 40 mA was measured.
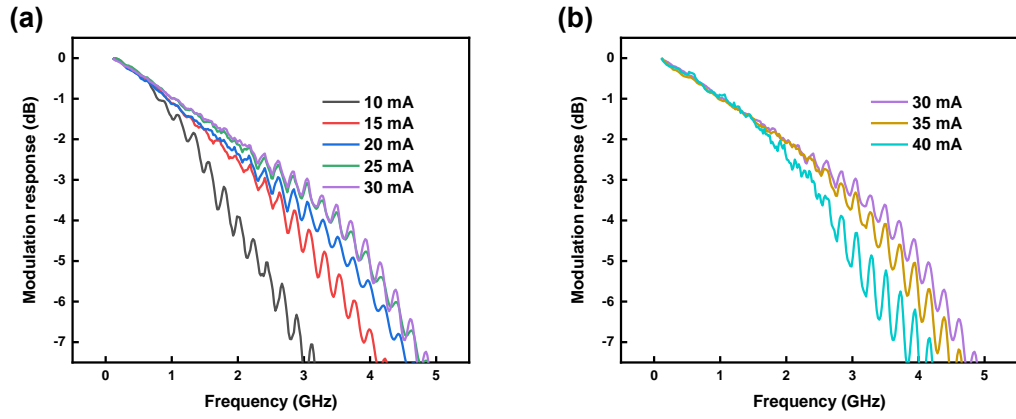
Figure 3.7: Small signal response of QD laser under different injection current with cavity length of 200 μm (a)small injection current and (b) high injection current.

It is common practice to renormalize the frequency response to 0 dB. From the frequency response data, only 1.5 GHz 3 dB-bandwidth is achieved with 10 mA injection. As the bias current increases to 15 mA, the bandwidth almost doubles with the value of 2.5 GHz. A further increasement in bandwidth of $f_{3\,dB} = 3.1\,GHz$ is measured with 25 mA continuous wave biased current. As the electrically pumped current increases from 30 to 40 mA, the 3 dB-bandwidth show a reducing tendency. Such saturation can be understood as a result of the large gain compression factor and low density of states in QD. Additionally, there is obvious fluctuation in the measured transfer function of the 200 μm. It is mainly due to the lack of feedback resistance and parasitics in the laser with short cavity length. It was speculated the slow capture and relaxation rate which are measured on picosecond times scales fundamentally limits the device speed [34-36].

In previous section, the resonant frequency is theoretically analysed to be proportionally related to the square root of the optical power. We then plot the bandwidth as a function of the square root of the relative biased current based on the small signal results.
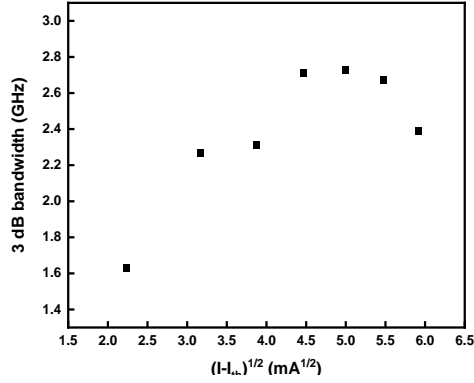
Figure 3.8:Relaxation frequency versus injection current.

From the slope of Figure 3.8, the modulation efficiency $D = f_{3dB}/(I - I_{th})^{1/2}$ between 10 mA up to 25 mA shows a value of $0.7\ GHz/\sqrt{mA}$. The lower D factor derived by the RIN is due to the overall relaxation oscillation frequency which is limited not only by the intensity noise and material quality but also the electrical parameters related to capacitance and resistance. The analysis based on fitted modulation efficiency from small signal response serves as a convenient and direct technique to calculate the differential gain if the dynamical measurements performed on lasers with various cavity length as the variation of $f_r/\sqrt{P}$ is known related to cavity losses.

It was anticipated that the intrinsic bandwidth and modulation efficiency of lasers can be improved by p-type doping which provides more holes and optimizing the mesa dimensions to form better current injection. We will then further check the small signal response of the 600 μm length laser with the identical coating conditions and materials.
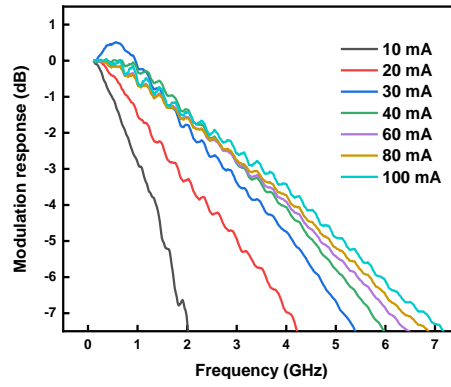
Figure 3.9: Small signal response of QD laser with cavity length of 600 μm.

The normalised modulation response of 600 μm QD laser was obtained with injection current from 10 mA to 100 mA. Under low injection current, relatively low 1.1 GHz 3 dB-bandwidth is achieved. As the bias current increase to 20 mA, the bandwidth doubles with the value of 1.9 GHz. This large rising rate keeps up to 40 mA and reaches a saturation stage up to 90 mA. A final bandwidth of 3.8 GHz is achieved. Additionally, an obvious peak exists for the response under 30 mA. In contrast, the modulation response under relatively high injection current is overdamped with the resonance peak vanished. Compared with the modulation response of 200 μm in Figure 3.9, the feedback-induced fluctuation diminishes as the resistant to the reflected power is enhanced with longer cavity length.

Based on the transfer function, the intrinsic bandwidth is predicted as

$$\omega_R^2 \approx \frac{v_g a N_{p0}}{\tau_p}$$
Equation 3.15

It is predicted that the intrinsic bandwidth should be promoted with decreasing cavity length. However, the 3 dB bandwidth measured from 600 μm is higher than its 200 μm counterpart. From the Equation 3.15, it can be determined that the frequency response depends on the intrinsic frequency, damping rate and also the device's electrical parasitics. These relatively low modulation bandwidth should be mainly limited by the RC roll-off.
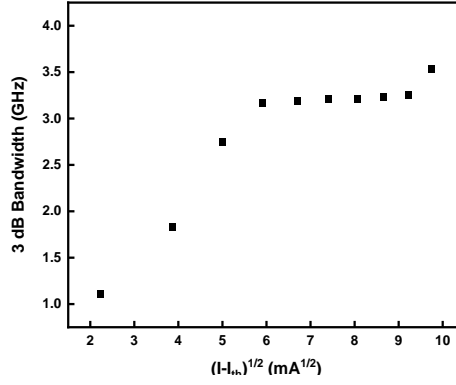
Figure 3.10:Relaxation frequency versus injection current.

A plot of $f_{3\ dB}$ versus the square root of relative injection current is shown in Figure 3.10, from which a modulation efficiency of 0.58 $GHz/\sqrt{mA}$ is fitted between 10 mA to 40 mA. This length variation is caused by the cavity loss and threshold induced differential gain variation. A further increased bandwidth under 100 mA may be the results of the excited state transitions.

From these results, the dynamic response of the QD lasers is far inferior to what is predicted and also the QW counterparts. Except for the mentioned improvement could be realised by optimised electrical properties and larger modal gain, other structural parameters can be considered as well.

It is obvious that modulation bandwidth is increased with higher value of ω_R. In order to understand how the ω_R is determined, we expand the expression of N_p and τ_p in terms of parameters that could be adjusted or measured. Above threshold $g = g_{th}$, the steady state photon density is derived as,

$$N_p = \frac{\eta_i(I - I_{th})}{qv_g g_{th}V}$$

Equation 3.16

Using Equation 3.21 for N_p, with g_{th} given by Equation 2.15, expression of ω_R in Equation 3.20 becomes,

$$\omega_R = \sqrt{\frac{\Gamma v_g a\eta_i(I - I_{th})}{qV}}$$

Equation 3.17

In this form, we observe that it is desirable to enhance the differential gain, internal efficiency, and the current relative to threshold, while minimize the volume of the mode for maximum bandwidth. Obviously, the modulation response increases as the input current increases. While for

the power consumption consideration, it is more desirable to decrease the threshold by optimizing the materials and laser structures, as well as by adjusting the facet reflectivity. The improvement in differential gain is consequential. In detail, the differential gain could be adjusted by manufacturing the material system to achieve large conduction band offset which will result in better electron confinement and thus higher differential gain value. Regarding the design of the small volume of the active region, high reflection coating will help as well. In addition, several cavity structures, including grating and complex cross section structure (BH rather than ridge waveguide), could be employed to improve the intrinsic frequency.

In the low-damping regime, f_{3dB} is usually estimated as

$$f_{3dB} = 1.55 f_r \qquad\qquad \textit{Equation 3.18}$$

At relative high powers, the maximum bandwidth is actually limited by the damping factor as

$$f_{3dB} = \frac{2\sqrt{2}\pi}{K} \qquad\qquad \textit{Equation 3.19}$$

A large K factor prevents high speed modulation, and the mechanism behind the suppression of relaxation oscillation is mainly the gain compression and transport effects. In detail, the reduction of K factor is largely limited by the photon lifetime related to the low mirror losses. From Equation 1.2, it is clear that the cavity length and facet reflectivity substantially determine the photon lifetime. Thus, in designing the high speed directly modulated lasers, it is important to have short cavities. Apart from its proportionality to the photon lifetime, other factors, including smaller intrinsic capture time, higher modal gain and differential gain, and lower gain compression factor, helps decreasing the K factor.

For the RC time constant, we could analyze the resistance and capacitance separately. The resistance increases with reduced area of active region and could be magnified by optimisation of doping profile, decreasing band discontinuity and special design of the electrode contact. However, the capacitance is almost independent of design of active layer and cavity. It is more related to the PN junction and the size of the bonding pad. In practice, semi-insulating current blocking structure and reduced area of upper cladding layer and boding pad size is widely employed.

3.4 Relative intensity noise measurements

Under steady state lasing conditions, the carrier and photon densities are assumed to remain constant. However, in reality, photons with random phases are emitted through random carrier recombination mainly induced by spontaneous emission, which perturbates the lasing modes and results in time variations of both the carrier and photon densities. Even when it is constantly biased by continuous wave injection in a very stable manner, the intensity fluctuation exists in the emitted light beam and, hence, imposes an ultimate limit on optical communication especially in direct detection system. To qualify the impact of intensity noise, RIN in lasers, defined as the ratio of the relative amplitude fluctuation of the optical power to the average output power, is measured. Its value is further normalised by the average power level over a well-defined bandwidth, usually with the unit of dB/Hz.

In the real optical interconnection, the RIN of lasers serves as a major noise source. The resultant degradation in signal quality and bit error rate limits the achievable data transmission rate [37]. Generally, a RIN value as low as -155 dB/Hz is necessary to achieve the required SNR in optical transmission. The increased electrical driving is often used for the compensation to get enough modulation bandwidth [38]. However, this strategy consumes more power and produces a relatively low efficiency. As a result, the reduction of RIN in lasers has attracted extensive interest to design future high-speed and low-noise devices integrated in photonic integrated circuits (PICs).

Both GaAs-based and InP-based QD lasers can produce a RIN as low as -160 dB/Hz while a higher value of -120 dB/Hz was reported in Si-based QD lasers [30, 39]. Further reduction in intensity noise and improved noise stability is envisioned by reducing the carrier noise or p-doping to suppress the hole thermalisation with greater energy intervals [40, 41].

The RIN spectra of different cavity length devices are plotted as a function of frequency with increasing current injection levels.
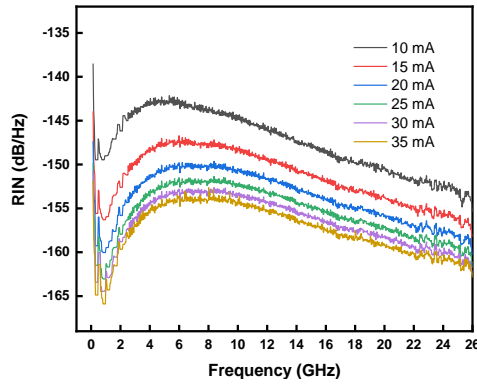
Figure 3.11: RIN for 200 μm cavity length laser biased at different injection current.

The RIN at frequency below 1 GHz is relatively high due to the combined effect of bias current noise, thermal noise and mode partition [42]. For the 200 μm QD laser with 10 mA injection, the RIN first increases with frequency and reaches a strong resonance peak around 5 GHz with a RIN value of -143 dB/Hz. At higher frequency, the RIN keeps reducing to lower than -151 dB/Hz at 26 GHz. As the injection current increases, the whole RIN spectra was down shifted with a peak value of -154 dB/Hz at an injection current of 35 mA. The decreasing value of RIN is due to the fact that the predominant source of intensity noise is generated by spontaneous emission. As the optical output power increases dramatically with the increase of injection current through stimulated emission, the spontaneous emission rate keeps almost unchanged above threshold. As a result, the ratio between the intensity noise and output power is reduced.

Two important figures of merit can be found from the RIN spectrum. The first is the D value, a figure of merit for the increase in RO frequency with square root of facet power out:

$$D = \frac{f_R}{\sqrt{P_{out}}}$$
<div align="right">*Equation 3.20*</div>

From the RIN spectra, the intrinsic bandwidth without the parasitic elements circuit can be derived. The resonance peak shows a trend towards higher frequency from 5 GHz under 10 mA to 7 GHz under 35 mA. In addition, the rate of change is first rapid from 10 to 20 mA while becomes steady afterwards. The D value is proportional to the differential gain of the device is found form the gradient of plotting resonant frequency as a function of square root of facet power.

Figure 3.12: Resonance peak in RIN spectra versus bias conditions.

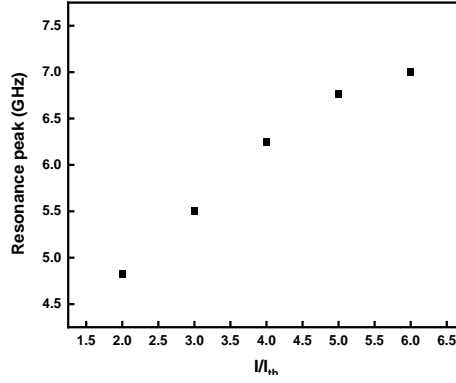Based on the RIN under different injection current and the corresponding resonance peak, the relaxation oscillation frequency is plotted as a function of the drive current. A D-factors of 0.98 GHz/mA$^{1/2}$ is demonstrated. The second key parameter is the k-factor limited bandwidth, namely the fastest intrinsic speed of the device at which recombination can occur and a measure of how fast the system responds after perturbation

$$\gamma = Kf_R^2 + \gamma_0 \qquad\qquad \textit{Equation 3.21}$$

where K is the damping time from which K-factor limited bandwidth is found, and γ_0 is a measure of electron decay time. From Equation 3.16, the damping rate is proportional to the square of the resonant frequency while the offset associates with the inverse of differential carrier lifetime. Thus, we could analyse the damping rate on laser with single cavity length as it is independent of device geometry and facet reflectivity. Plotting damping as a function of relaxation oscillation frequency squared, the gradient of the graph is a measure of the intrinsic k-factor damping of the laser without parasitics.

A profile of the RIN as a function of frequency allows determination of key intrinsic behaviors of a laser without the degradations of parasitics such as resistance and capacitances in the device. By modelling the RIN spectra, the damping and k-factor limited bandwidth can be found.

$$RIN = \frac{A\omega^2 + B}{(\omega^2 - \omega_R^2)^2 + \omega^2\gamma^2} \qquad\qquad \textit{Equation 3.22}$$

where A and B are fitting constants, ω is frequency at which the response is measured, ω_R is resonant relaxation oscillation frequency, and γ is damping parameter. Based on the fitting parameter, we can further predict the intrinsic frequency response. If we consider only the

limitation of the intrinsic properties of material and damping effects while neglecting the electrical parasitics, the 3 dB bandwidth can be simplified as

$$\frac{f_r^2}{(f_{3\,dB}{}^2 - f_r^2)^2 + f_{3\,dB}{}^2 \gamma^2/(2\pi)^2} = \frac{1}{2} \qquad \textit{Equation 3.23}$$

$$f_{3\,dB} = \frac{2\sqrt{2}\pi}{K} \qquad \textit{Equation 3.24}$$

From the above theoretical inference and the RIN spectra, we derive a K factor of 1.7 ns. This value is consistent with most of the simulated and experimentally measured level. The high damping factor in QD lasers is considered as a dominant limiting factor for high modulation bandwidth. It is also reported that the K factor and thus the intensity noise decrease with the p-doping concentration to a certain range [43]. Other strategies to further optimize the damping effects include choosing the optimum photon lifetime, reducing the intrinsic capture time and maximizing the modal gain [30, 44, 45].

3.5 Conclusion

In this chapter, the intensity noise and dynamic performance of QD lasers were discussed to pave the way for high-speed low-noise laser source for PICs. Due to the spontaneous emission, even under CW operation, intensity noise is generated in the output of lasers. The RIN of 200 μm QD FP laser under different injection current was measured. An obvious resonance peak appeared around 5 GHz with a low RIN value of -143 dB/Hz. As the injection current increases, the peak frequency is shifted slightly with a reduced noise intensity. Based on the RIN spectra, the intrinsic frequency of QD laser can be estimated, and the modulation efficiency is derived. The QD laser is proved to have a relatively low RIN of -155 dB/Hz, which is desirable for optical communication system.

After checking the intensity noise characteristics, we then directly modulated the QD laser and verified the corresponding small signal response. It is predicted that the modulation bandwidth is affected by the cavity length, and we thus measured the small signal response of both 200 μm and 600 μm length devices. However, two devices give a similar and limited performance of 3dB bandwidth below 5 GHz, which is far inferior to the predicted results. It is analysed that the oscillation frequency is degraded mainly due to the lack of proper electrical design. Both the

commercial copper substrate and top-down chip structure are not suitable for high-speed operation. The 600 μm length device was also measured, as the laser with longer cavity normally gives better feedback resistance and temperature stability. Its modulation efficiency 0.58 $GHz/\sqrt{mA}$ is fitted between 10 mA to 40 mA.

From all these dynamic performances of QD lasers, it is concluded that QD laser provide low noise operation which satisfies the requirement of -155 dB/Hz in optical communication systems and has the potential to give a high direct modulation bandwidth. Although the small signal response of the laser is limited by the electrical properties and modal gain, a wide digital modulation can be achieved. QD lasers thus can be considered as a promising candidate for future high-speed PICs with an optimised electrical and wafer design.

Reference

1.   Lau, K. and A. Yariv, *Ultra-high speed semiconductor lasers*. IEEE Journal of Quantum Electronics, 1985. **21**(2): p. 121-138.

2.   Tucker, R.S., *High-speed modulation of semiconductor lasers*. IEEE transactions on electron devices, 1985. **32**(12): p. 2572-2584.

3.   Su, C. and V. Lanzisera, *Ultra-high-speed modulation of 1.3-μm InGaAsP diode lasers*. IEEE journal of quantum electronics, 1986. **22**(9): p. 1568-1578.

4.   Bowers, J., et al., *High-speed InGaAsP constricted-mesa lasers*. IEEE journal of quantum electronics, 1986. **22**(6): p. 833-844.

5.   Kirstaedter, N., et al., *Gain and differential gain of single layer InAs/GaAs quantum dot injection lasers*. Applied Physics Letters, 1996. **69**: p. 1226-1228.

6.   Matsui, Y., et al., *30-GHz bandwidth 1.55-μm strain-compensated InGaAlAs-InGaAsP MQW laser*. IEEE Photonics Technology Letters, 1997. **9**(1): p. 25-27.

7.   Ishida, M., et al., *Photon lifetime dependence of modulation efficiency and K factor in 1.3μm self-assembled InAs / GaAs quantum-dot lasers: Impact of capture time and maximum modal gain on modulation bandwidth*. Applied Physics Letters, 2004. **85**(18): p. 4145-4147.

8.   Saito, H., K. Nishi, and S. Sugou *Low chirp operation in 1.6 μm quantum dot laser under 2.5 GHz direct modulation*. Electronics Letters, 2001. **37**, 1293-1295.

9.   Petermann, K., *Laser diode modulation and noise*. Vol. 3. 1991: Springer Science & Business Media.

10.   *Dynamic Effects*, in *Diode Lasers and Photonic Integrated Circuits*. 2012. p. 247-333.

11.   Keiser, G., *Optical fiber communications*. Vol. 2. 2000: McGraw-Hill New York.

12.   Zhu, N.H., et al., *Directly Modulated Semiconductor Lasers*. IEEE Journal of Selected Topics in Quantum Electronics, 2018. **24**(1): p. 1-19.

13.   Govind, P.A. *Noise in semiconductor lasers and its impact on optical communication systems*. in *Proc.SPIE*. 1991.

14.   Kallimani, K.I. and M.J.O. Mahony, *Relative intensity noise for laser diodes with arbitrary amounts of optical feedback*. IEEE Journal of Quantum Electronics, 1998. **34**(8): p. 1438-1446.

15.   Hui, R. and M. O'Sullivan, *Chapter 3 - Characterization of Optical Devices*, in *Fiber Optic Measurement Techniques*, R. Hui and M. O'Sullivan, Editors. 2009, Academic Press: Boston. p. 259-363.

16.   Joindot, I., *Measurements of relative intensity noise (RIN) in semiconductor lasers*. Journal de Physique III, 1992. **2**: p. 1591.

17.   Olshansky, R., V.A. Lanzisera, and P.M. Hill, *Subcarrier multiplexed lightwave systems for broad-band distribution*. Journal of Lightwave Technology, 1989. **7**(9): p. 1329-1342.

18.   Sheikhey, M.M., et al., *Analytical investigation of relative intensity noise*

properties of injection-locked mid-IR quantum cascade lasers. Journal of the Optical Society of America B, 2016. **33**(11): p. D57-D64.

19.   Tatham, M.C., et al., *Resonance frequency, damping, and differential gain in 1.5 mu m multiple quantum-well lasers.* IEEE Journal of Quantum Electronics, 1992. **28**(2): p. 408-414.

20.   Henry, C., *Theory of the phase noise and power spectrum of a single mode injection laser.* IEEE Journal of Quantum Electronics, 1983. **19**(9): p. 1391-1397.

21.   Lee, S. and A.E. Willner, *OPTICAL COMMUNICATION SYSTEMS | Basic Concepts*, in *Encyclopedia of Modern Optics*, R.D. Guenther, Editor. 2005, Elsevier: Oxford. p. 376-387.

22.   Maximov, M.V., et al., *InGaAs/GaAs Quantum Dot Lasers with Ultrahigh Characteristic Temperature.* Jpn. J. Appl. Phys, 1997. **36**: p. 4221-4223.

23.   Kirstaedter, N., et al., *Gain and differential gain of single layer InAs/GaAs quantum dot injection lasers.* Applied Physics Letters, 1996. **69**(9): p. 1226-1228.

24.   Kamath, K., et al., *Small-signal modulation and differential gain of single-mode self-organized In0.4Ga0.6As/GaAs quantum dot lasers.* Applied Physics Letters, 1997. **70**(22): p. 2952-2953.

25.   Bhattacharya, P., et al., *In (Ga) As/GaAs self-organized quantum dot lasers: DC and small-signal modulation properties.* IEEE Transactions on Electron Devices, 1999. **46**(5): p. 871-883.

26.   Bimberg, D., et al., *InGaAs-GaAs quantum-dot lasers.* IEEE Journal of Selected Topics in Quantum Electronics, 1997. **3**(2): p. 196-205.

27.   Ishida, M., et al., *Photon lifetime dependence of modulation efficiency and K factor in 1.3 μ m self-assembled InAs ∕ GaAs quantum-dot lasers: Impact of capture time and maximum modal gain on modulation bandwidth.* Applied physics letters, 2004. **85**(18): p. 4145-4147.

28.   Qasaimeh, O., *Effect of inhomogeneous line broadening on gain and differential gain of quantum dot lasers.* IEEE Transactions on Electron Devices, 2003. **50**(7): p. 1575-1581.

29.   Dery, H. and G. Eisenstein, *The impact of energy band diagram and inhomogeneous broadening on the optical differential gain in nanostructure lasers.* IEEE Journal of Quantum Electronics, 2005. **41**(1): p. 26-35.

30.   Capua, A., et al., *Direct correlation between a highly damped modulation response and ultra low relative intensity noise in an InAs/GaAs quantum dot laser.* Optics Express, 2007. **15**(9): p. 5388-5393.

31.   Fiore, A. and A. Markus, *Differential Gain and Gain Compression in Quantum-Dot Lasers.* IEEE Journal of Quantum Electronics, 2007. **43**(4): p. 287-294.

32.   Zhang, Z., et al., *Effects of modulation p doping in InAs quantum dot lasers on silicon.* Applied Physics Letters, 2018. **113**(6): p. 061105.

33.   Shchekin, O.B. and D.G. Deppe, *The role of p-type doping and the density of states on the modulation response of quantum dot lasers.* Applied Physics Letters, 2002. **80**(15): p. 2758-2760.

34.   Klotzkin, D., et al., *Enhanced modulation bandwidth (20 GHz) of In/sub 0.4/Ga/sub 0.6/As-GaAs self-organized quantum-dot lasers at cryogenic temperatures:*

role of carrier relaxation and differential gain. IEEE Photonics Technology Letters, 1998. **10**(7): p. 932-934.

35.   Deppe, D.G. and D.L. Huffaker, *Quantum dimensionality, entropy, and the modulation response of quantum dot lasers.* Applied Physics Letters, 2000. **77**(21): p. 3325-3327.

36.   Zhang, L., et al., *Excited-state dynamics and carrier capture in InGaAs/GaAs quantum dots.* Applied Physics Letters, 2001. **79**(20): p. 3320-3322.

37.   *Photonic Integrated Circuits*, in *Diode Lasers and Photonic Integrated Circuits*. 2012. p. 451-507.

38.   Li, H., et al., *Relative intensity noise of temperature-stable, energy-efficient 980 nm VCSELs.* AIP Advances, 2017. **7**(2): p. 025107.

39.   Liao, M., et al., *Low-noise 1.3 μm InAs/GaAs quantum dot laser monolithically grown on silicon.* Photonics Research, 2018. **6**(11): p. 1062-1066.

40.   Duan, J., et al., *Carrier-Noise-Enhanced Relative Intensity Noise of Quantum Dot Lasers.* IEEE Journal of Quantum Electronics, 2018. **54**(6): p. 1-7.

41.   Duan, J., et al., *Effect of p-doping on the intensity noise of epitaxial quantum dot lasers on silicon.* Optics Letters, 2020. **45**(17): p. 4887-4890.

42.   Zhou, Y.-G., et al., *Relative intensity noise of InAs quantum dot lasers epitaxially grown on Ge.* Optics Express, 2017. **25**(23): p. 28817-28824.

43.   Duan, J., et al. *Relative intensity noise of silicon-based quantum dot lasers.* in *2019 Compound Semiconductor Week (CSW)*. 2019.

44.   Deppe, D.G., H. Huang, and O.B. Shchekin, *Modulation characteristics of quantum-dot lasers: the influence of p-type doping and the electronic density of states on obtaining high speed.* IEEE Journal of Quantum Electronics, 2002. **38**(12): p. 1587-1593.

45.   Kovsh, A.R., et al., *InAs/InGaAs/GaAs quantum dot lasers of 1.3μm range with enhanced optical gain.* Journal of Crystal Growth, 2003. **251**(1): p. 729-736.

4 Feedback noise characteristics

After giving the brief introduction to the three main devices employing quantum dot (QD) structure, the practical issue caused by facet reflection in the integrated circuits will be discussed in the following section.

The on-chip photonic integration in Si photonics platform brings many innovative properties while the development of extremely low-cost laser sources is especially in great demand. Nowadays, the improved material quality together with the mature fabrication techniques allows for the massive production. However, in the photonic integrated circuits (PICs), reflections are produced from facets of each component, which will cause perturbation in the photon density. The weak external feedback can sometimes enhance the longitudinal mode selection and reduce the distortion in modulation [1-3]. However, the useful range of feedback effects is restricted to a very narrow range. In most general situations, serious problems, such as an increase in intensity and frequency noise and degradation of modulation, arise in practice from the unintentional reflection [4-7]. Detailed understanding of the mechanism of the fluctuation has been provided in many researches [8, 9]. The optical field is perturbed with the light reflected back into the cavity from the unlinked fiber facets and other reflective surfaces. Due to the fluctuation in photon density, the carrier density and the gain profile will be consequently affected. As a result, a variety of significant changes take place even with a minute fraction of reflection, including threshold current change, excess noise, linewidth broadening, high and low frequency components to the intensity noise, un-damped relaxation oscillation, or even coherence collapse accompanying abrupt increase of noise and linewidth [9-14]. This situation is even more complex in semiconductor laser due to its broad gain spectrum and sensitive refractive index which depends on the temperature and carrier density [15].

Despite the well-developed integration of III-V lasers on Si-based PICs, the stability of the

integrated lasers still has a critical issue caused by the combination of the internal and external reflections from the passive and active interfaces on the circuits. The inclusion of optical isolators was thus indispensable to block the reflections from each on-chip component and keep the transmitter working in the stable condition with low noise state. However, the cost of an isolator is usually equivalent or even higher than the laser chip itself [16]. Even worse, optical isolators are sometimes not available under specific circumstances. There are three basic categories of integrated isolators: based on nonlinear effect, spatiotemporal modulation, and magneto-optic effects. However, up to now, the applicable integrated isolator with strong isolation and negligible insertion loss has not been demonstrated. Therefore, the isolator-free transmitter with stable performance remains a major objective that can revolutionize the core technology of the physical layer.

In practical optical fiber communication systems, optical connectors act as a periodic reflector with the maximum value of as much as 13.2% [17]. Under such high-level feedback, the performance of the widely used quantum well (QW) lasers is severely destabilised. Several methods have been employed to promote the feedback resistant, such as the corrugated waveguide and gain-coupling structures [18-20]. However, inherent sensitivity to feedback in QW structure makes the realisation of feedback-insensitive lasers challenging.

At the communication band around 1.3 μm, QD lasers on the GaAs substrates have been considered as a promising alternative to the extensively used InP-based QW lasers [21]. Regarding the feedback sensitivity, QD laser also demonstrates better performance due to its relatively small linewidth enhancement factor (LEF) around zero or even negative value. The symmetric gain curves and very small resultant coupling between phase and amplitude are generated in QD devices. This relationship is quantitively evaluated by LEF, which governs the sensitivity of semiconductor to external feedback. Based on the extra insensitivity, it is possible to design directly modulated lasers operating without isolator. A 2.5 Gb/s modulation was demonstrated with QD distributed feedback (DFB) laser with the signal-to-noise ratio starts to degrade at -30 dB feedback while the critical level for coherence collapse was verified by spectral broadening as -14 dB. Recently, the feedback tolerance of QD lasers has been improved to -8 dB. 10 Gb/s 20 km feedback-resistant transmission was demonstrated by 1.3 μm directly modulated QD laser. Although from the optical and RIN spectra, the critical feedback level was extracted to be -9 dB, the degradation in eye

119

diagram and BER is limited. As a result, both the fabrication complexity and cost in Si photonics will be reduced, and smaller footprint is achieved. This new merit attracts wide attentions in recent years and the noise feature of QD lasers has been improved by various methods.

In our measurements, we investigate QD lasers with external feedback, concerning the transition to the coherence collapse and transmission performance. Experiments have been performed with QD lasers with stripe width of 2.2 μm and cavity length ranged between 600 and 1200 μm. In details, the stability of QD lasers under strong feedback level is observed through threshold current changes, intensity noise, optical spectra and dynamic performances [22, 23]. The primary purpose is to examine carefully the mechanisms and characteristics of the coherence collapse state. Apart from this intrinsic theoretical significance, the eradication and exploitation of coherence collapse can be further determined. The theoretical analysis and experimental setup are briefly reviewed in the first place. Then, the interference effects between the reflected light and optical filed inside laser is verified with respect of the optical spectrum, noise characteristics, small signal modulation and large signal transmission performance. Based on the transition of the static and dynamic performances of laser, several regimes are confirmed, which offers a convenient way of designing and predicting the operation of the optical communication system. However, the influences of the static and dynamic performance are not always identical. This work also aims at further evaluating and systematically comparing the potential impact of optical feedback in different characteristics.

4.1 Theory

The effect of feedback light is first theoretical analysed, from which the critical feedback level is mathematically calculated. When analyzing the effects of reflected light, an external feedback term is accounted for adding a term to the standard laser equation in complex form corresponding to the re-injection of output light back to the cavity with a delay of an external cavity round trip time.

$$\frac{d}{dt}E(t)e^{j\Omega t} = \left\{ j\omega_N(N_e) + \frac{1}{2}[G(N_e) - \alpha_i] \right\} E(t)e^{j\Omega t}$$
$$+ \kappa E(t-\tau)e^{j\Omega(t-\tau)}$$

Equation 4.1

Here, $\omega_N(N_e)$ is the longitudinal mode resonant frequency defined with an integer $\omega_N = N\pi c/nL_d$, α_i is the cavity loss and c is the light velocity. The last term represents the noise source added by the external feedback. The coupling strength relates to the cavity parameters between the two cavities with coefficient κ is described as

$$\kappa = c(1 - R_2)\sqrt{\frac{R_3}{R_2}}(2nL_d)^{-1} \qquad \textit{Equation 4.2}$$

Starting from a usual form the rate equation, the carrier density under feedback can be expressed as:

$$\frac{d}{dt}N_e = \frac{\eta_i I}{qV} - \frac{N_e}{\tau_e} - G(N_e)|E|^2 \qquad \textit{Equation 4.3}$$

In stationary lasing, E should be set constant with the real and imaginary part separately expressed as,

$$G(N_e) - \alpha_i + 2\kappa\cos(\Omega\tau) = 0 \qquad \textit{Equation 4.4}$$

$$\omega_N(N_e) - \Omega - 2\kappa\sin(\Omega\tau) = 0 \qquad \textit{Equation 4.5}$$

The onset point of stability relates to the difference in gain and oscillation frequency. We could first consider the simple single mode operation case. If the solution of these oscillation condition becomes multivalued under feedback noise and a set of external cavity modes are generated around the original solitary mode, coherence collapse is theoretically formed [24]. By analyzing the coupling between gain and oscillation frequency, equations for the change in steady state gain and oscillation frequency under reflection are then changed as:

$$\Delta G = -\kappa\cos(\Omega\tau) \qquad \textit{Equation 4.6}$$

$$\Delta\omega = -\kappa[\sin(\Omega\tau) + \alpha\cos(\Omega\tau)] \qquad \textit{Equation 4.7}$$

From the application aspect, the dynamic characteristics with optical feedback need to be addressed as well [25]. Based on the rate equations, the numerical analysis of the modulation response simply starts from the transfer function of single mode laser. In the small signal domain, the transfer function can be evaluated, based on the ratio between modulation current and modulated optical power [26, 27],

$$H'(j\omega) = [1 - K(j\omega)] \cdot \frac{H(j\omega)}{1 - K(j\omega)H(j\omega)} \qquad \textit{Equation 4.8}$$

$$K(j\omega) = j\frac{2(1 - R)\sqrt{(1 + \alpha^2)f_{ext}}}{2\sqrt{R}\tau_l\omega}[1 - \exp(j\omega\tau_{ext})] \qquad \textit{Equation 4.9}$$

$$C = \frac{1 - R}{2\sqrt{R}}$$

<div align="right">Equation 4.10</div>

where τ_L is the cavity round-trip time, and C is the coupling coefficient of the laser's front facet. $H(j\omega)$ corresponds to the normalised transfer function without optical feedback as $K(j\omega) = 0$. The feedback level f_{ext} of a semiconductor laser is defined as the critical ratio between the re-injected power and the original emitted power. At a certain feedback level, this transfer function exhibits unstable poles, which could be used to theoretically predict the critical feedback coefficient expressed as[28, 29],

$$f_{crit} = \frac{\tau_L^2 \gamma^2}{16C^2} \left(\frac{1 + \alpha_H^2}{\alpha_H^4} \right)$$

<div align="right">Equation 4.11</div>

In theory, this critical value gives the maximum ratio between the feedback and output power that can be tolerated for the stable operation for both device operation and communication system.

It is clear that except for several factors contribute to determine the value of critical feedback conditions includes the damping factor and LEF which are determined by the material quality, but also on the geometry of the laser cavity and external cavity parameters.

4.2 Experimental setup

The device under study is a QD Fabry-Perot (FP) laser emitting at 1.3 μm grown on a (001) GaAs substrate by solid source molecular beam epitaxy (MBE). The active layer contains a seven-fold stack of InAs QDs, and the length of the device is 600 μm with a stripe width of 2.2 μm. The asymmetrical coating with 90% HR coating on the back end and 30% AR coating on the near facet was applied for the high efficiency and protection purposes.

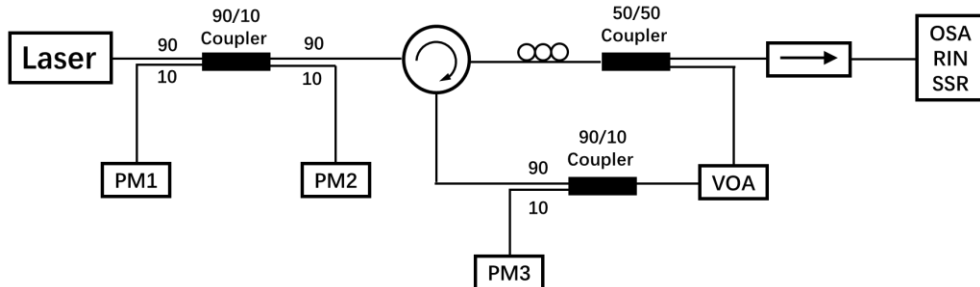<div align="center">Figure 4.1: Feedback resistance setup.</div>

As shown in Figure 4.1, the setup consists of the laser, a coupling circuit, a feedback circuit and a monitor system. The laser output is split into feedback and monitor paths by a 90/10 optical fiber coupler directed to the feedback loop. An optical circulator is used to direct part of the output light back into the laser cavity while a variable optical attenuator is used to adjust the feedback ratio. Additionally, a polarisation controller is inserted to maintain the transverse electric polarisation of the feedback light and thus maximize the effects of the optical feedback. The feedback ratio is defined as the optical power ratio between feedback light and incoming light at the fiber of the laser. By adjusting the value of variable optical attenuator (VOA), feedback strength was varied from 0% up to 100% and monitored by optical powermeters connected to the coupler. The power in the 10% arm is fed into the power meter to monitor the forward and backward power which are used to estimate the external feedback ratio defined as $\Gamma_{dB} = P_1 - P_0 + C_{dB}$, where P_1 is the reflected power, P_0 is the output power of the laser, C_{dB} is the coupling loss from the semiconductor laser to the fiber. Power meter 1 and 2 were used to experimentally calculate the amount of reflection. The feedback loop contains a circulator which directs the output power back into the cavity. The polarisation controller is adjusted to guarantee the same polarisation between the reflected light and emitted light from laser. Then, a 3 dB coupler is used to couple a portion of the light to a VOA which sends it back to the circulator and then to the cavity. To avoid excess uncontrolled reflection, all the loops are connected by the angle-polished fiber ends. Optical coupling losses of the system was about -4dB.

The external cavity length of the feedback is kept around 5 meters to create the most stringent feedback conditions as the corresponding external feedback frequency is 30 MHz ($f = c/L_{ext}$), far below the laser's relaxation oscillation frequency.

Another half of the power is coupled through an isolator to the diagnostic instruments to observe the optical and electrical spectra, modulation and transmission characteristics. In order to avoid extraneous feedback, an isolator is positioned before the monitor systems. The optical spectrum is simply measured by using the high-resolution optical spectrum analyzer, while the noise spectra is measured by the microwave spectrum analyzer. Regarding the modulation properties, the small signal response was detected by p-i-n photodetector, and the frequency response is determined by measuring the S_{21} scattering parameter with a network analyzer.

4.3 Static characteristics

Similar to the research about the characteristics of QD laser without feedback, we will first examine the simple static case under feedback. The electric and optical properties are measured, which corresponds to the change in noise spectra and longitudinal mode. With these results, the critical feedback level, based on the onset of transitions, is determined.

4.3.1 Electrical spectrum

The electrical spectrum demonstrates the intensity noise. Generally, the intensity noise derived from radio-frequency spectrum includes the noises generated by the device under test and the related measuring equipment. We subtracted the ground intensity noise from the radio frequency spectrum of the overall system and plotted it under different feedback ratio. The threshold for coherence collapse was determined by the sudden increasement and large fluctuation in the laser intensity noise.
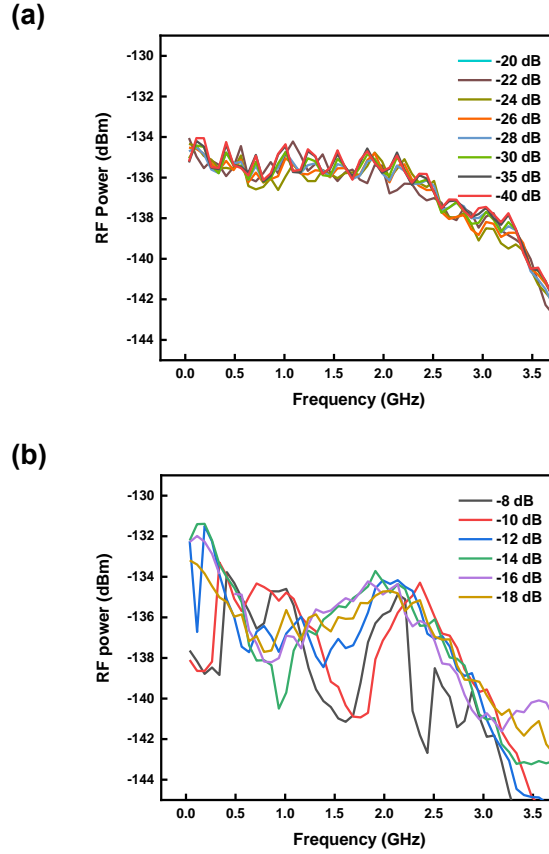
Figure 4.2: Spectral density of 600 μm length laser under different feedback levels (100 mA injection current) (a) weak feedback up to -20 dB and (b) strong feedback from -18 dB.

Figure 4.2 shows the evolution of the noise spectra of QD laser with feedback above and below coherence collapse threshold. In the curve of weak optical feedback ratio up to -20 dB, the microwave spectrum below 3 GHz is simple broadband noise and remains around -135 dBm. In this regime, our QD laser is stable against the optical feedback as there is no obvious sign of nonlinear oscillations in the radio frequency (RF) map. For the higher reflected power, intense chaotic oscillation starts in the RF response. For the curve with higher reflected power, sharp increases and fluctuations over 10 dB between -130 to -140 dBm in the low-frequency range are shown, and groups of large spikes in the noise spectrum are exhibited. At this stage, any further increase of the reflected strength will lead to a more complex chaos. A drastic destabilisation is shown with further increase of the optical feedback intensity above -14 dB, which can be considered as a critical feedback level based on the electrical spectra. This value is much higher than that of commercial QW lasers of which a critical level is usually expected to be around only -30 dB.
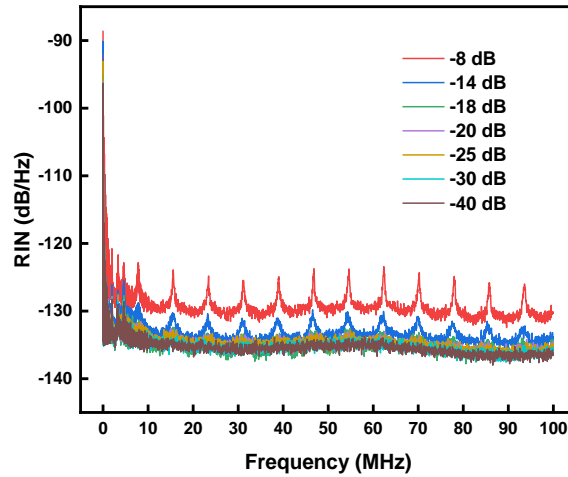
Figure 4.3: RIN in the low frequency range of 600 μm length laser under different feedback levels (100 mA injection current).

A critical feedback level is first verified by the electric spectra over a large frequency range. We will then focus on low frequency range below 100 MHz with high resolution and greater accuracy. The relative intensity noise (RIN) at low frequency of QD laser under different reflected strength is depicted above, in which a more precise determination is made. Similar to the observation in the noise spectra, for a reflected ratio below -18 dB, the RIN remains flat and stable. As the feedback increases up to -14 dB, the satellite modes at roughly multiples of the resonance of the external cavity start to appear. The peak-to-valley extinction ratio is around 5 dB/Hz for -14 dB feedback level and increases to 10 dB/Hz for -8 dB. Except for the sharp transition in the value of intensity noise, we can further derive the properties of external cavity based on the RIN in low frequency.

4.3.2 Optical spectrum

In previous measurement, the adverse effect of reflected light on intensity noise is observed and the critical feedback level is determined. We then check the impact on the optical spectra. It is theoretically predicted that under strong optical feedback, destabilisation of the longitudinal modes will be formed with undesired side modes, wavelength shift and fluctuation in the mode amplitude.

Optical spectra of the QD FP laser under different feedback levels are shown in Figure 4.4.

While the pump current is held constant at 100 mA and the external cavity loop is fixed, the feedback fraction is increased from -40 dB. At room temperature, multimode lasing operation centred at 1303 nm was observed at an injection current of 100 mA. At the lowest feedback levels, the envelope of the FP laser spectrum is stable, with only a slight fluctuation in the intensity. The apparent destabilisation starts to appear at feedback level of -18 dB and deteriorates dramatically from -14 dB.
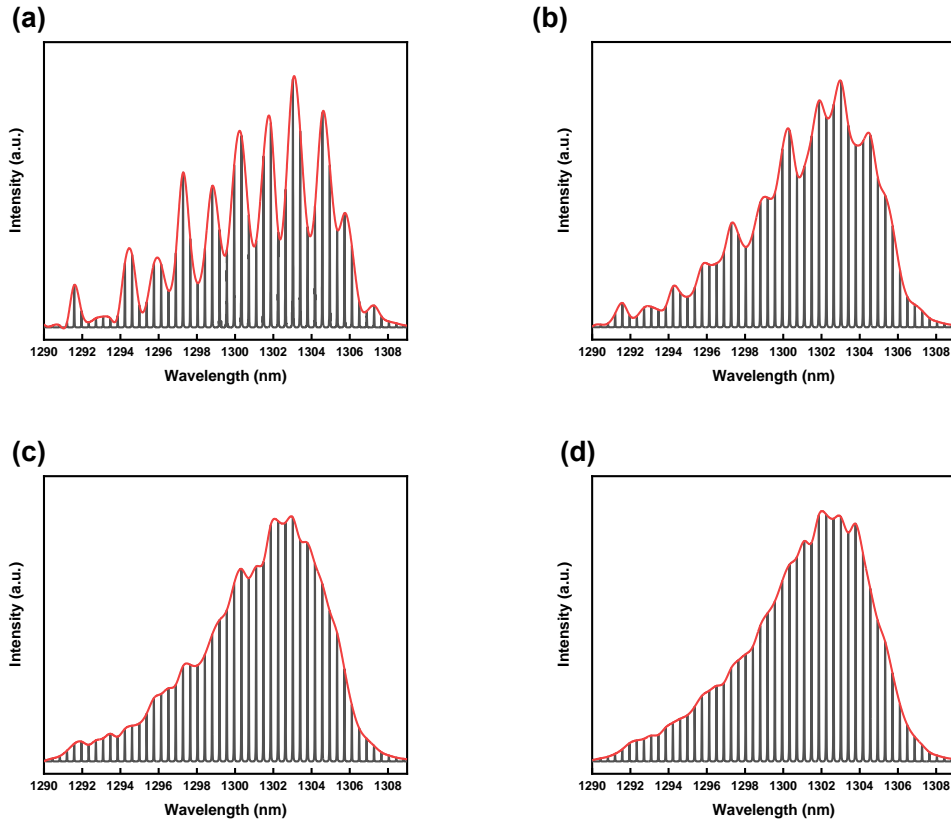

Figure 4.4: Optical spectra of 600 μm length laser (30% facet coating) under different feedback levels (100 mA injection current) (a) -8 dB, (b) -14 dB, (c) -20 dB and (d) -40 dB.

Comparing the spectrum under -20 dB feedback with the -40 dB counterpart, the light intensity remains perfectly stable and centre modes remain close to the solitary laser frequency. For weak feedback below the critical level, the modification in gain and oscillation is quite small. Thus, the solitary laser frequency keeps unchanged without obvious intensity fluctuation. With a higher feedback level, a clear fluctuation in the amplitude of mode exists. Similar to the impact on intensity noise, feedback ratio higher than -14 dB is considered as the beginning of the coherence collapse regime from the transition of optical spectra. Due to the multimode property of FP cavity,

the wavelength shift cannot be distinguished from the low-resolution spectra with large wavelength range. As shown in Figure 4.4, the highest mode was found to be 1.25 times larger than the nearest neighboring mode and reaches as much as twice the amplitude under -8 dB feedback ratio. The splitting at the top of laser spectrum is attributed to mode hopping with a separation of 1.152 nm.
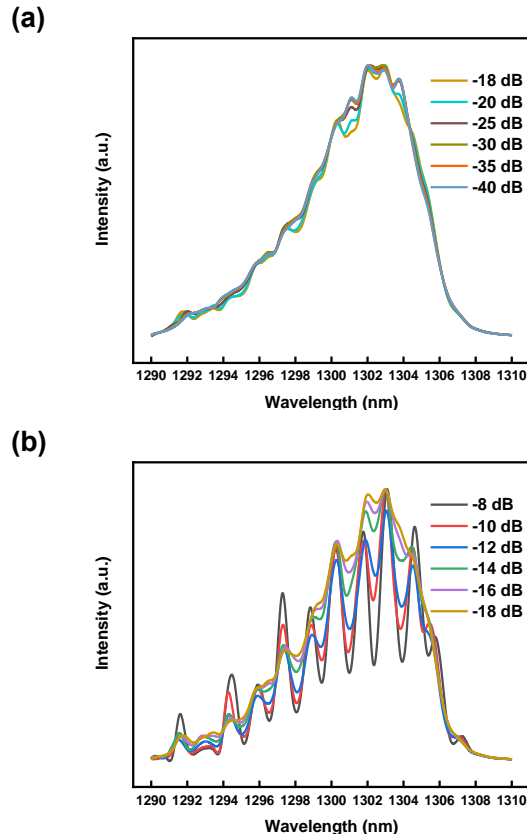

Figure 4.5: Envelope of the optical spectra of 600 µm length laser (30% facet coating) under different feedback levels (100 mA injection current) (a) weak feedback up to -20 dB and (b) strong feedback from -18 dB.

The envelopes of the optical spectra are then further compared. As shown in Figure 4.5, for the feedback level lower than -20 dB, the envelope of the optical spectra is nearly superposed. As the feedback strength increases above -14 dB, the occurrence of the beating which corresponds to the external cavity modes increases. It is pointed out in [30] that the phase fluctuations are indeed an dominant process, leading to the coherence collapse. Up to the point of chaotic phenomenon, the coherence is maintained as light propagates in the external cavity system [31]. The dominance of the well-defined external cavity modes has important implications as the appearance of the emission line splitting is evidenced as the transition of the feedback regimes. With increasing

feedback intensity, the perturbation in the spectrum becomes severer.
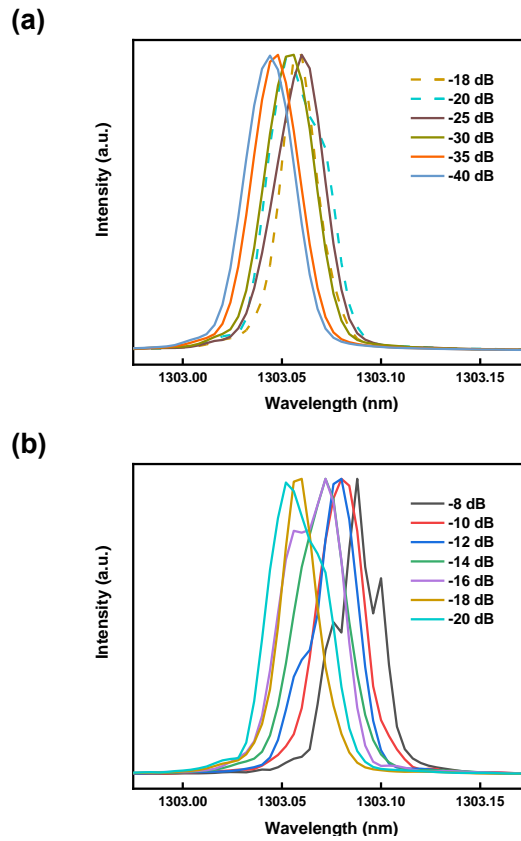
(a)

(b)

Figure 4.6: High resolution optical spectra of the central mode of 600 μm length laser (30% facet coating) under different feedback levels (100 mA injection current (a) weak feedback up to -18 dB and (b) strong feedback from -20 dB.

Further precise spectral measurement with higher resolution is depicted in Figure 4.6. There are marked differences in the spectral behavior of central mode depending on the feedback levels. For a feedback ratio below -20 dB, the mode intensity distribution is slightly shifted with no sign of obvious spectral broadening. The change in laser field oscillation is the result of the altered modal gain induced by optical feedback, and the corresponding frequency is shifted to satisfy the conditions for steady state operation in laser. Moreover, the change in gain is accompanied by the redshift in the cavity resonance frequency due to incoherent optical feedback applied.

As the reflection becomes severe, the continuous red-shift is interrupted and down shifted when the reflected ratio increases from -25 to -20 dB. Then red-shift tendency recovers. Additionally, the chaos in spectrum arises and the linewidth is broadened, which denotes the onset of coherence collapse range. This regime occupies a range of feedback power ratio. In Figure 4.6

(b), the line continues to broaden with increasing feedback intensity, corresponding to the various stages of the coherence collapse beginning at -16 dB. The quantity estimation is not provided in our description due to the resolution limit of the optical spectrum analyzer (OSA).

The results of the optical and electrical spectra are quite compatible, with a typical value of -14 dB based on these measurements of 600 μm length QD laser under 100 mA injection current. This value is far higher than that of common QW lasers where -30 dB can be expected. The stable operation of QD lasers can be partly attributed to their relatively low linewidth enhancement factor and high damping rate, which stems from the existence of high gain compression. The optical spectrum shows a more visually clear variation and tendency with the modified feedback levels. We will then check the feedback sensitivity of different operating condition and different devices based on the optical spectrum characteristics.

4.3.3   Variation of feedback sensitivity under different injection current

It is mentioned before that the LEF is one of the most distinguished parameter of semiconductor laser and the characteristic behavior under optical feedback depends greatly on its value. In previous research, it is found that the LEF is enhanced with increasing bias current. Consequently, the feedback sensitivity of QD laser will be dramatically affected by the injection current. We then vary the bias conditions to 50 mA and 150 mA, and check the impact up to -18 dB reflected light based on envelope of the optical spectra.
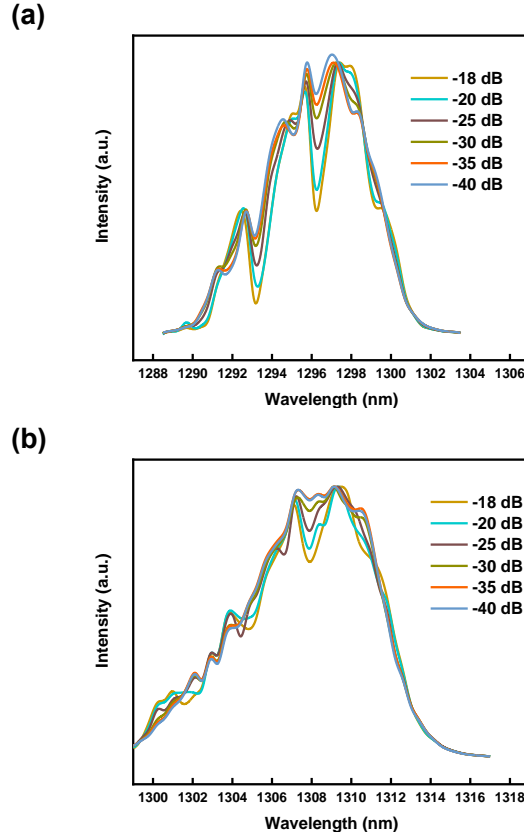
(a)

(b)

Figure 4.7: Optical spectra of 600 μm length laser under different feedback levels (a) 50 mA injection current and (b) 150 mA injection current.

The output power coupling into the fiber is measured to be 3.384 mW and 10.93 mW under 50 mA and 150 mA, respectively. The ground state (GS) emission remains stable for this range of currents with red shift of the gain peak from 1297 nm at 50 mA to 1309 nm at 150 mA, and no sign of spectral broadening exists. At 50 mA, the laser is found to be insensitive to optical feedback up to -30 dB. This relative reduced feedback resistance is attributed to the lower relaxation oscillation and thus decreased damping rate. Under -18 dB feedback ratio, the fluctuation in optical spectrum is obvious with the ratio between the highest mode and nearest valley which increased to more than twice. As the injection current increase to 150 mA, the destabilisation is retarded, but the tolerance to feedback is inferior to the performance with 100 mA injection current. As shown in Equation 5.11, the coherence collapse is accelerated due to the strong enhancement of LEF with increasing bias current. Consequently, the control of both LEF and damping factor remains as the most important issue for designing isolator-free lasers.

In contrast to DFB lasers in which a better stability against optical feedback is observed at

larger bias current, the destabilisation of FP lasers was proved to be more complex due to modal competition [27, 32, 33]. Additionally, it is verified that the appropriate operation condition determines the feedback sensitivity performance.

4.3.4   Variation of feedback sensitivity in longer device

The onset of the coherence collapse regime can be theoretically evaluated based on the expression shown in Equation 4.11, where τ_L is the internal round trip time in laser cavity. Obviously, the critical value increases with the longer cavity length. The envelope of spectra and high-resolution spectra of the 1200 μm length FP laser are shown below. The coating condition remains the same as 90 % high reflection coating on rear facet and 30 % on the other. To maintain the same output power, the laser is biased at 200 mA.
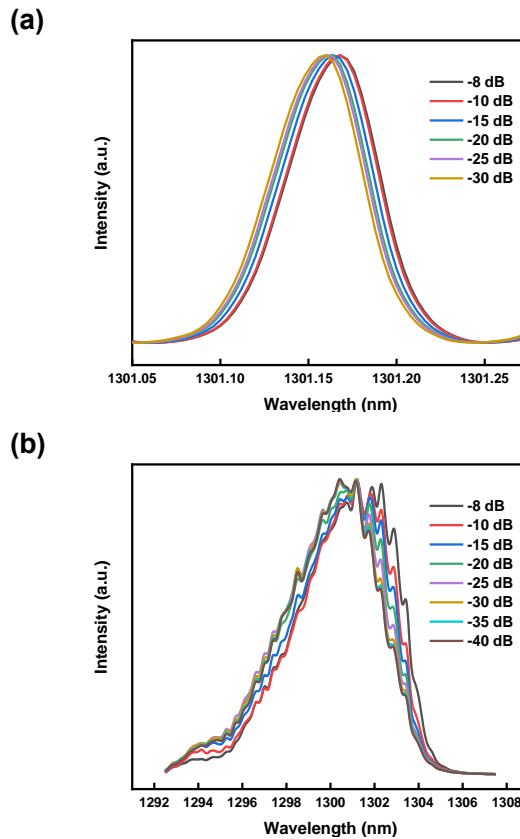
(a)

(b)

Figure 4.8: Spectral density of 1200 μm length laser under different feedback levels (a) high resolution spectra and (b) normal resolution spectra.

Based on these spectra, this 1200 μm length QD laser exhibits a stronger stability against

optical feedback. In the above figure, the central mode keeps quite stable with the increased feedback level. There is no sign of spectral broadening while the peak wavelength is equally red shifted up to -8 dB feedback ratio. From the envelope of the whole spectra, as the reflection increases, the 1200 μm length QD laser remains almost unperturbed for the whole range feedback strength, with slight red-shift in both the low-resolution envelope and high-resolution single mode view. The enhancement of the robustness to the feedback results from the longer cavity length and thus cavity round-trip time. From the mathematical expression, the critical feedback level is proportional to the squared cavity length. However, excessive long cavity length poses a limitation to the modulation capability of lasers. In order to increase both speed and reflection tolerance, 600 μm QD FP laser is chosen for the dynamic measurements in the following sections.

4.4 Small signal response with feedback

In previous sections, the feedback was kept static, generated by circulating the output power back into the cavity. The results of the optical and electrical spectra are quite identical with different resolutions. However, the feedback robustness of laser in dynamic condition and real application is more complicated. Even though the laser keeps stable against continuous wave (CW) output, the pattern-dependent noise is added to the signal during re-injection of the modulated output. The evaluation of the stability of directly modulated QD laser under dynamic modulated feedback is necessary. In most real isolator-free applications, the modulated feedback signal is almost the only source of injection, where the back-travelling modulated signal is the actual source of injection to the laser source. The small signal transfer function has been discussed, yielding large deviations in the amplitude and phase due to optical feedback [25, 34, 35]. We then verified the optical resistance of small signal response of the 600 μm length laser with asymmetric coating of 30/90 at an injection current of 100 mA.
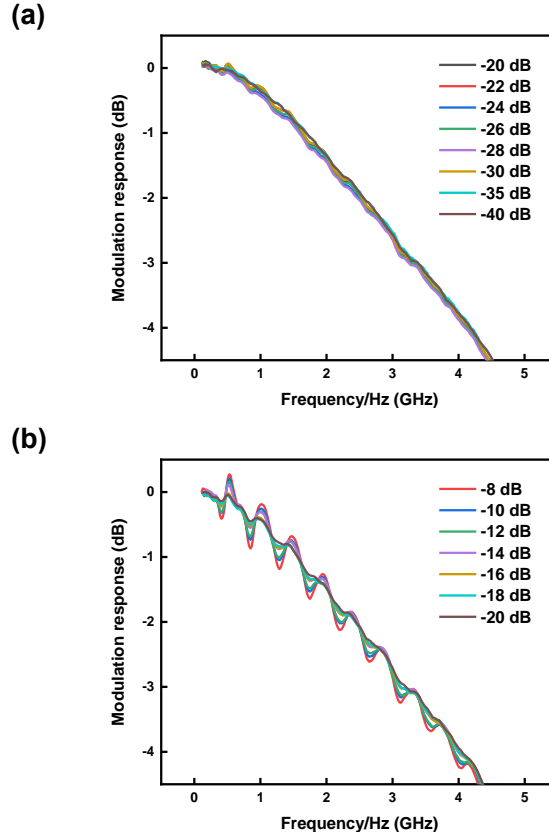
(a)

(b)

Figure 4.9: Small signal response of 600 μm length laser under different feedback levels (a) weak feedback up to -20 dB and (b) strong feedback from -20 dB.

Figure 4.9 shows the measured amplitude of the transfer function. For the feedback ratios lower than -20 dB, the small signal response remains stable with a 3 dB bandwidth around 3.5 GHz. As the feedback strength increases, the overall transfer function does degrade much with a constant slope and 3 dB bandwidth. Above the critical feedback level, the transmission performance produces large variations in $|S_{12}|$ of more than 0.3 dB. From these results, it is found that the QD laser provides a consistent critical feedback level for both static operation and small signal modulation. The experiment is then performed on the testbed environment to derive the upper limit in the real digital modulation.

4.5 Conclusion

In this chapter, we have estimated the effect of unintentional optical feedback on the high-speed digital optical communication system. Although the impact of the reflection starts at around

-18 dB feedback level, the existence of such fluctuation does not necessarily mean that coherence collapse occurs. Both static performance and direct modulation are considered for the 600 μm length QD FP laser. It is found that above -14 dB reflection, the chaotic behavior, which could be regarded as the onset of coherence collapse regime, is obvious in the optical and electrical spectra and small signal modulation.

Reference

1.   Bogatov, A., et al., *Study of the single-mode injection laser.* IEEE Journal of Quantum Electronics, 1973. **9**(2): p. 392-394.

2.   Voumard, C., R. Salathé, and H. Weber, *Resonance amplifier model describing diode lasers coupled to short external resonators.* Applied physics, 1977. **12**(4): p. 369-378.

3.   KOBAYASHI, K., *Improvements in direct pulse code modulation of semiconductor lasers by optical feedback.* IEICE TRANSACTIONS (1976-1990), 1976. **59**(12): p. 8-14.

4.   Broom, R., et al., *Microwave self-modulation of a diode laser coupled to an external cavity.* IEEE Journal of Quantum Electronics, 1970. **6**(6): p. 328-334.

5.   Chinone, N., K. Aiki, and R. Ito, *Stabilization of semiconductor laser outputs by a mirror close to a laser facet.* Applied Physics Letters, 1978. **33**(12): p. 990-992.

6.   Ikushima, I. and M. Maeda, *Self-coupled phenomena of semiconductor lasers caused by an optical fiber.* IEEE Journal of Quantum Electronics, 1978. **14**(5): p. 331-332.

7.   Morikawa, T., et al., *Return-beam-induced oscillations in self-coupled semiconductor lasers.* Electronics Letters, 1976. **12**(17): p. 435-436.

8.   Hirota, O. and Y. Suematsu, *Noise properties of injection lasers due to reflected waves.* IEEE Journal of Quantum Electronics, 1979. **15**(3): p. 142-149.

9.   Fujiwara, M., K. Kubota, and R. Lang, *Low-frequency intensity fluctuation in laser diodes with external optical feedback.* Applied Physics Letters, 1981. **38**(4): p. 217-220.

10.   Alam, M.F. and M.A. Karim, *External Optical Feedback Effects in Distributed Feedback Semiconductor Lasers*, in *Advances in Imaging and Electron Physics*, P.W. Hawkes, Editor. 1999, Elsevier. p. 73-120.

11.   Sigg, J., *Effects of optical feedback on the light-current characteristics of semiconductor lasers.* IEEE journal of quantum electronics, 1993. **29**(5): p. 1262-1270.

12.   Tkach, R. and A. Chraplyvy, *Regimes of feedback effects in 1.5-μm distributed feedback lasers.* Journal of Lightwave technology, 1986. **4**(11): p. 1655-1661.

13.   Temkin, H., et al., *Reflection noise in index-guided InGaAsP lasers.* IEEE journal of quantum electronics, 1986. **22**(2): p. 286-293.

14.   Li, H., J. Ye, and J.G. McInerney, *Detailed analysis of coherence collapse in semiconductor lasers.* IEEE journal of quantum electronics, 1993. **29**(9): p. 2421-2432.

15.   Lang, R. and K. Kobayashi, *External optical feedback effects on semiconductor injection laser properties.* IEEE Journal of Quantum Electronics, 1980. **16**(3): p. 347-355.

16.   He, Y., et al., *10-Gbps 20-km Feedback-Resistant Transmission Using Directly Modulated Quantum-Dot Lasers.* IEEE Photonics Technology Letters, 2020. **32**(21): p. 1353-1356.

17.   Park, K.H., et al., *The effects of external optical feedback on the power penalty of DFB-LD modules for 2.5Gbs−1 optical transmission systems.* Optical and Quantum Electronics, 1998. **30**(1): p. 23-31.

18.   Huang, Y., et al. *External optical feedback resistant characteristics in partially corrugated-waveguide laser diodes*. Electronics Letters, 1996. **32**, 1008-1009.

19.   Yidong, H., et al., *External optical feedback resistant 2.5-Gb/s transmission of partially corrugated waveguide laser diodes over a -40℃ to 80℃ temperature range*. IEEE Photonics Technology Letters, 1999. **11**(11): p. 1482-1484.

20.   Favre, F. *Sensitivity to external feedback for gain-coupled DFB semiconductor lasers*. Electronics Letters, 1991. **27**, 433-435.

21.   Ribbat, C., et al., *Complete suppression of filamentation and superior beam quality in quantum-dot lasers*. Applied Physics Letters, 2003. **82**(6): p. 952-954.

22.   Liu, A.Y., et al., *Reflection sensitivity of 1.3 μm quantum dot lasers epitaxially grown on silicon*. Optics Express, 2017. **25**(9): p. 9535-9543.

23.   Huyet, G., et al., *Quantum dot semiconductor lasers with optical feedback*. physica status solidi (a), 2004. **201**(2): p. 345-352.

24.   Tromborg, B., J. Osmundsen, and H. Olesen, *Stability analysis for a semiconductor laser in an external cavity*. IEEE journal of quantum electronics, 1984. **20**(9): p. 1023-1032.

25.   Helms, J. and K. Petermann, *Microwave modulation characteristics of semiconductor lasers with optical feedback*. Electronics Letters, 1989. **25**(20): p. 1369-1371.

26.   Schunk, N. and K. Petermann, *Numerical analysis of the feedback regimes for a single-mode semiconductor laser with external feedback*. IEEE Journal of Quantum Electronics, 1988. **24**(7): p. 1242-1247.

27.   Helms, J. and K. Petermann, *A simple analytic expression for the stable operation range of laser diodes with optical feedback*. IEEE Journal of Quantum Electronics, 1990. **26**(5): p. 833-836.

28.   Favre, F., *Theoretical analysis of external optical feedback on DFB semiconductor lasers*. IEEE Journal of Quantum Electronics, 1987. **23**(1): p. 81-88.

29.   Olshansky, R., et al., *Frequency response of 1.3 µm InGaAsP high speed semiconductor lasers*. IEEE Journal of Quantum Electronics, 1987. **23**(9): p. 1410-1418.

30.   Cohen, J.S. and D. Lenstra, *Spectral properties of the coherence collapsed state of a semiconductor laser with delayed optical feedback*. IEEE Journal of Quantum Electronics, 1989. **25**: p. 1143-1151.

31.   Lenstra, D., B. Verbeek, and A.D. Boef, *Coherence collapse in single-mode semiconductor lasers due to optical feedback*. IEEE Journal of Quantum Electronics, 1985. **21**(6): p. 674-679.

32.   Spencer, P., P. Rees, and I. Pierce, *Theoretical Analysis*, in *Unlocking Dynamical Diversity*. 2005. p. 23-54.

33.   Huang, H., et al., *Multimode optical feedback dynamics of InAs/GaAs quantum-dot lasers emitting on different lasing states*. AIP Advances, 2016. **6**(12): p. 125114.

34.   Way, W.I. and M.M. Choy, *Optical feedback on linearity performance of 1.3-mu m DFB and multimode lasers under microwave intensity modulation*. Journal of Lightwave technology, 1988. **6**(1): p. 100-108.

35.   Helms, J. and K. Petermann, *Microwave modulation of laser diodes with optical feedback*. Journal of Lightwave Technology, 1991. **9**(4): p. 468-476.

5 Large signal modulation and Si photonics module

The static and dynamic properties of QD FP lasers have been comprehensively measured and discussed. For the real application, large signal modulation should be considered, based on the eye diagram. When it comes to commercial optical module, more complicated structure and measurements need to be carried out. In this chapter, the practical performance of the QD laser will be estimated under the large signal modulation with and without feedback. Moreover, the isolator-free Si photonics module employed QD laser as the light source will be measured.

5.1 Large signal modulation of 600 μm quantum dot Fabry-Perot laser

It is common to use small signal bandwidth as an indicator for large signal modulation performance. For a given bandwidth of 1 GHz, more than 1.43 GHz in large signal bandwidth could be obtained in the case of several optical devices [1]. This effect is also considered inherently in semiconductor lasers, regarding the dynamical performance. However, this type of characterisation does not provide sufficient information, and it is reported that in some QD lasers, the digital modulation properties are vastly underestimated, in terms of its digital modulation, especially in the QD laser with high gain compression and large gain value [2]. The eye diagram under large signal modulation (0.8Vpp) is described as follows.
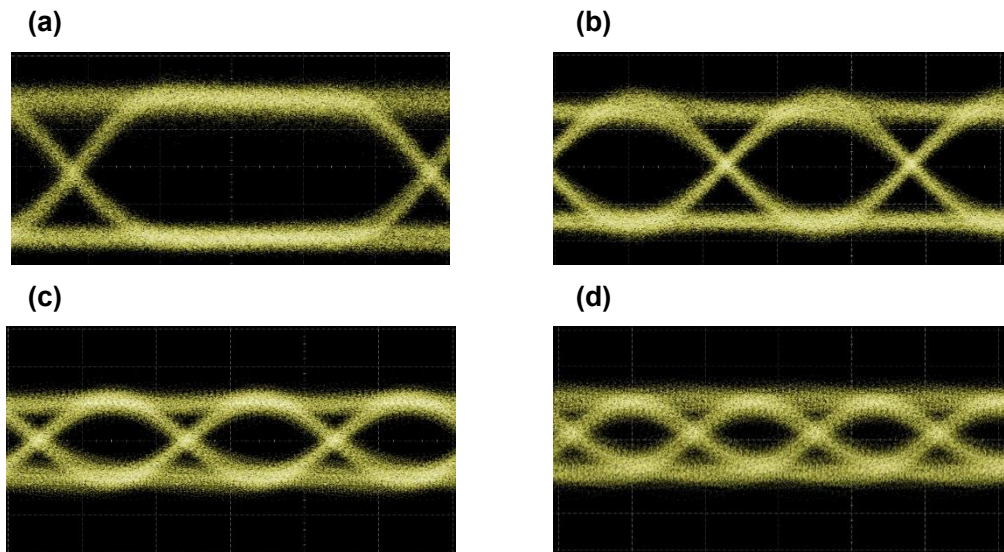
Figure 5.1: Eye diagram of QD laser under 100 mA injection current with cavity length of 600 μm (a) 5Gbps, (b) 10 Gbps, (c) 25 Gbps and (d) 30 Gbps.

From the 5 Gbps to as high as 30 Gbps, the 600 μm QD laser exhibits a clear open eye with an extinction ratio above 3 dB, as shown in Figure 3.13. This wide digital modulation, compared with its small signal response, is ascribed to the large gain value and high gain compression of QD [2]. It is well known that the intrinsic frequency of laser diode is limited by both the gain compression factor and modal gain. There was impressive improvements in the gain of QD lasers while the gain compression remains large, which stems from the basic material nonlinearity and long transport times [3-5]. For instance, the 1.3 μm GaAs QD laser gave a bandwidth of 11 GHz and was modulated at 25 Gbps, which can be ascribed to a relatively high modal gain of 46/cm measured from 8 QD layers in this laser [6].
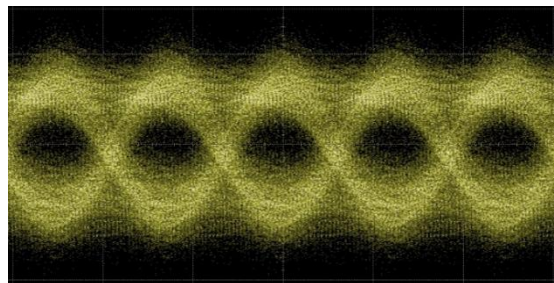

Figure 5.2: Eye diagram of QD laser at 20 Gbps under 30 mA injection current with cavity length of 200 μm.

The similar performance of 200 μm QD laser of 20 Gbps large signal modulation is also shown in Figure 5.2. The ability of modulating the laser with limited small signal bandwidth at large bit rates with sufficiently large modal gain and large compression factor is only obtainable in practice with QD structures [2].

5.2 Transmission characteristic with feedback

Based on the results of optical spectrum, noise intensity and small signal response under the same reflected light, the onset of the coherence collapse is estimated to be -14 dB. Although the impact of the reflection starts at around -18 dB feedback level, the existence of such fluctuation does not necessarily mean that the coherence collapse occurs. The 600 μm length QD laser provides a 3 dB bandwidth of 3.5 GHz under -14 dB feedback. Generally, the real digital modulation of QD laser usually far exceeds the predicted bandwidth based on small signal response, and the coherence collapse in dynamic process is quite complicated. We would then further examine the feedback resistance in data transmission. The effects of intensity modulation on the chaotic behavior in the laser output are examined, and performance estimation for 10 and 25 Gb/s systems are made.

The laser is modulated by non-return-to-zero format, and the loss of the fiber connection and systems is calibrated and compensated. Eye diagrams under 10 Gb/s modulation back-to-back transmission are shown in Figure5.3 (a) – (d) for feedback levels of -8 dB, -14 dB, -20 dB and without feedback, respectively.
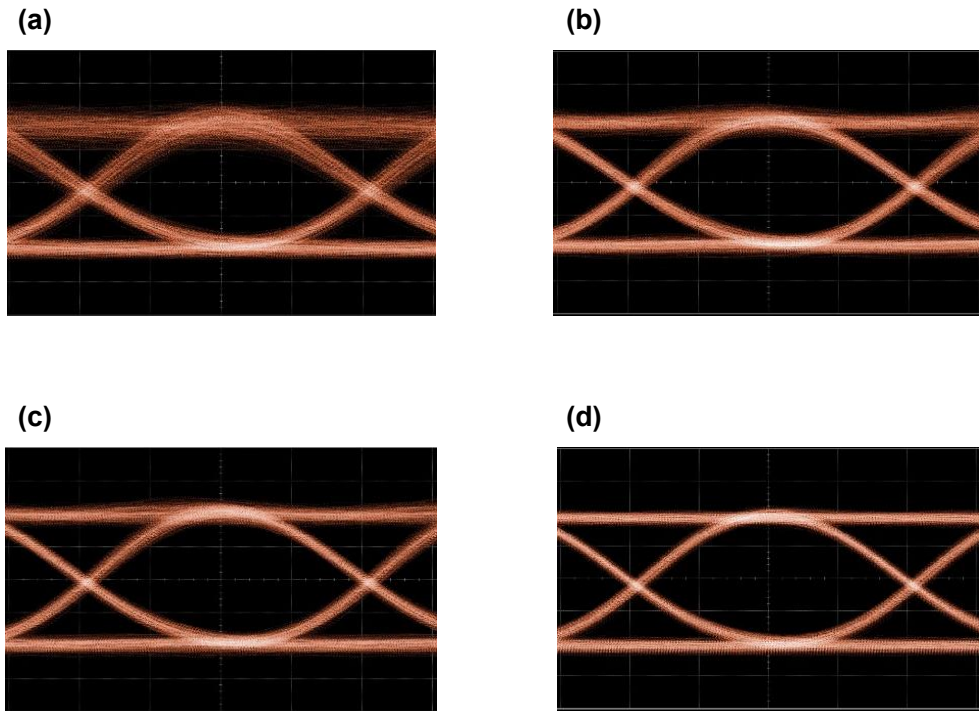
Figure 5.3: 10 Gb modulation eye diagram of 600 μm length laser under 100 mA injection current with different feedback level (a) -8 dB, (b) -14 dB, (c) -20 dB and (d) without feedback.

Whatever the feedback level is, no chaotic oscillations are observed on the eye diagram, and these results remain clear with extinction ratio more than 4 dB. In general, it is well known that the data transmission is theoretically no longer possible in the coherence collapse regime. However, from the eye diagram in Figure 5.3, the transmission performance slightly degrades only with the upper level broadened at the feedback level of -14 dB, corresponding to '1' bits of the eye diagram. Distributions of the '0' level and timing jitters, including rise and fall time, were not affected by external optical feedback. The broaden of level one signal becomes worse as the reflected power gets stronger, but the whole eye diagram still remains quite stable. In previous research, five distinct regimes of feedbacks are identified and the transitions between the regimes are well defined[7].

For the 802.3ae 10 Gb/s Ethernet standard, the laser must be tolerant up to -12 dB feedback from the network. Although the critical level of -14 dB is confirmed by the static and dynamic characteristics, based on the clear eye diagram of the QD laser under -8 dB together with the coupling losses, the QD FP laser should still be able to tolerate network feedback without an isolator.
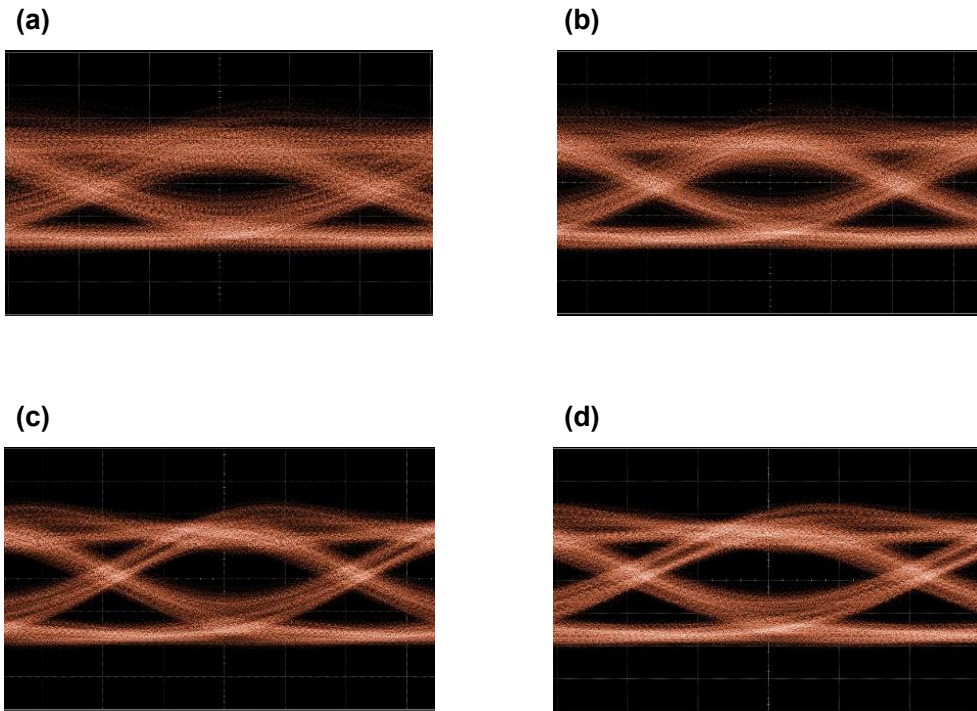
Figure 5.4: 25 Gb modulation eye diagram of 600 μm length laser under 100 mA injection current with different feedback level (a) -8 dB, (b) -14 dB, (c) -20 dB and (d) without feedback.

With an advanced compensation and digital processing techniques such as forward error correction (FEC) and 4 level pulse amplitude modulation (PAM4), the large signal modulation could be further pushed to 25 Gb/s. This high-speed operation is achieved by digital processing and compensation for the connection and facilities. As shown in small signal response, due to the lack of proper designment in electrical parameters and large damping in QD materials, there is no clear relaxation oscillation peak. Although the 3 dB bandwidth is limited to below 5 GHz, through the digital processing, the loss caused by links and connections could be compensated for more than 10 dB. The result eye diagrams for different feedback level are shown above. Compared with the 10 Gb/s transmission, the extinction ratio (ER) decreases to relatively lower value of around 1 dB and the chaotic oscillation becomes severe especially in the upper level due to the impact of feedback and also the limited bandwidth.

5.3 100G Si photonic module

The module measurement setup and the corresponding commercial test board are shown in Figure 5.5. In commercial DR1 Si photonics transmitter, distributed feedback (DFB) laser, Mach-Zehnder modulator and other passive optical components are heterogeneously integrated. We replaced the complex high-cost quantum well (QW) DFB laser in DR1 module with our 1000 μm QD FP laser with 30/90 coating and removed isolator connected to the laser.

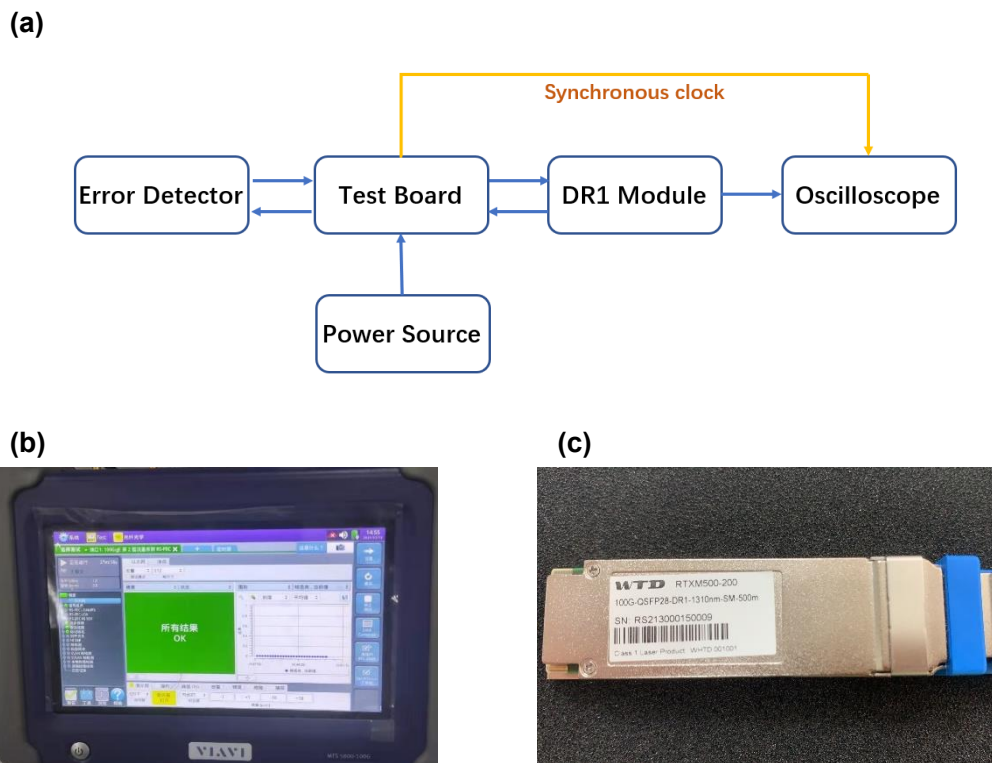**(a)**

(b)

(c)

Figure 4.10: (a) The schematic diagram of the setup of module measurements, (b) The screen of the test board and (c) Image of 100G QSFP28-DR1 1310nm module .

The applied voltage of the test board was set as 3.3V, and 56 Gb PAM4 signal was sent from the bit error rate (BER) tester. The back-to-back eye performance was displayed by the oscilloscope with the (TDECQ) of 1.78 dB, ER of 4.657 dB and optical modulation amplitude (OMA) of -4.417 dBm.
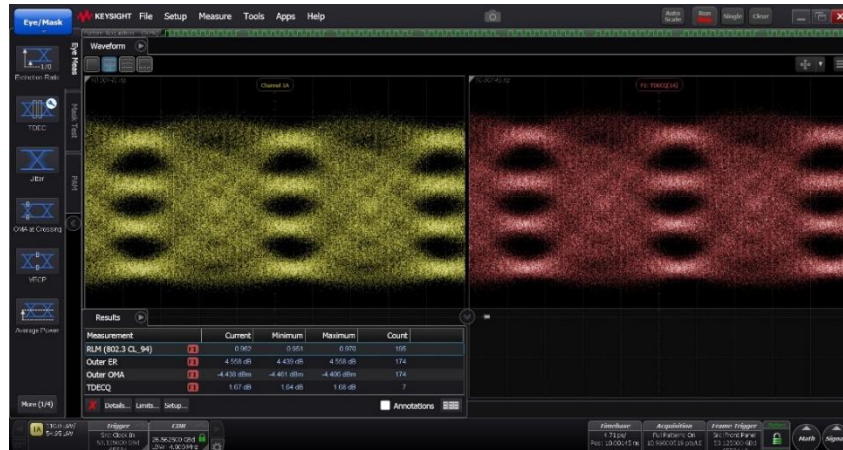
Figure 4.11: 53 Gbps PAM4 eye diagram of the 100G QSFP28-DR1 1310 nm module .

The sensitivity of this transmitter was also measured, which gives a BER of 2e-4 under -10.5 dBm optical output. This demonstrated DR1 module gives a comparable performance with commercial module and well meets the requirement for 100 G data centre applications.

5.4 Conclusion

From the 5 Gbps to as high as 30 Gbps, the laser exhibits a clear open eye with an extinction ratio above 3 dB. This wide digital modulation compared with its small signal response is postulated due to the large gain value and high gain compression.

The feedback resistance is further examined in the transmission system. Especially for direct modulated QD laser, higher damping means lower overshoot and lower intensity noise, which are essential to the transmission system. Eye diagrams under 10 Gb/s modulation back-to-back transmission are shown, and relatively clear results are shown with feedback power higher than the critical level of -14 dB confirmed by the static characteristics. Due to the gain compression in QD, the high-speed operation of 30 Gb/s eye diagram is demonstrated before. As we impose a -8 dB feedback strength, the eye diagram degrades to limited extent with the chaos generated mainly on the upper lid. As the gain compression has impact on both the feedback resistance and modulation performance, especially in QD laser, a superior feedback-resistant high-speed modulation is achieved for the digital modulation. Based on the transmission result, this QD laser should still be able to tolerate the standard network feedback without an isolator.

Lastly, the high-performance, low-cost property of QD laser is verified in the commercial Si

photonics DR1 modules. Over 100 Gbps transmission was successfully demonstrated by the isolator-free QD FP laser based module with its performance compatible to the QW DFB laser module with indispensable isolator.

Reference

1.   Hentschel, C., *Fiber optic test and measurement.* 1998: Prentice-Hall.

2.   Gready, D., et al., *On the relationship between small and large signal modulation capabilities in highly nonlinear quantum dot lasers.* Applied Physics Letters, 2013. **102**(10): p. 101107.

3.   Grillot, F., et al., *Gain Compression and Above-Threshold Linewidth Enhancement Factor in 1.3-<formula formulatype="inline"><tex Notation="TeX">$\mu\hbox{m}$</tex> </formula> InAs–GaAs Quantum-Dot Lasers.* IEEE Journal of Quantum Electronics, 2008. **44**(10): p. 946-951.

4.   Kovsh, A.R., et al., *InAs/InGaAs/GaAs quantum dot lasers of 1.3μm range with enhanced optical gain.* Journal of Crystal Growth, 2003. **251**(1): p. 729-736.

5.   Gilfert, C., et al., *High gain 1.55 μ m diode lasers based on InAs quantum dot like active regions.* Applied Physics Letters, 2011. **98**(20): p. 201102.

6.   Xu, J., L. Xu, and Y. Tang, *Proc. Lasers and Electro-Optics (CLEO) and Quantum Electronics and Laser Science Conference (QELS).* 2010, IEEE.

7.   Tkach, R. and A. Chraplyvy, *Regimes of feedback effects in 1.5-μm distributed feedback lasers.* Journal of Lightwave technology, 1986. **4**(11): p. 1655-1661.

6 Conclusion and future work

This chapter provides a summary of the work and result derived in previous chapters regarding the statics, dynamical, and feedback resistance of quantum dot (QD) laser. The achievements are highlighted and conclusions are given. Finally, the suggestions for the future Si photonic module are presented. Additionally, the related transmission and module performance based on our device are also demonstrated.

6.1 Conclusion

The realisation of high-performance laser on GaAs substrate plays a prior role in the integrated Si photonics module. This thesis aims to make an evaluation of the QD Fabry Perot (FP) laser on GaAs and its application in optical communication.

In chapter one, the motivation and development of Si photonics are presented first. QD structure has been considered as a promising solution and its application in each component is briefly discussed. Semiconductor laser has attracted the most exploration due to its sensitivity to defects and required high gain value. The temperature insensitive QD laser with low threshold current, high efficiency and reasonable large bandwidth has been realised. Another important feature needs to be noticed in integrated circuit is the feedback tolerance. The reflection resistance of the QD laser was first theoretically analysed and feedback-resistant QD laser in 1.3 μm was reviewed. Except the background of the above substance provided in chapter one, the fundamentals of semiconductor laser and QD devices are also reviewed.

In chapter two, experimental methods are discussed. The fabrication process and related techniques are first provided. Brief description about the lithography, etching, metallisation and

facet coating is presented. Material characteristics, including atomic force microscope (AFM), photoluminescence (PL) and scanning electron microscope (SEM), are shown. The measurement setup of the static, dynamic and feedback sensitivity are then displayed.

Chapter three gives the static performance of QD FP lasers. Light-current-voltage (LIV) curve is regarded as the most basic result, from which the threshold current, slope efficiency, turn-on-voltage and resistance can be derived. Wall plug efficiency (WPE) and differential external quantum efficiency (DEQE) can be further calculated from the LIV curve of single laser. By varying the cavity lengths, the physical parameters of material such as internal quantum efficiency, internal loss and transparency current are mathematically fitted. Moreover, the static performance under different temperatures is measured. From all these results, the advantages of high efficiency, temperature stable and low threshold current of QD lasers are verified.

The dynamical performances are demonstrated in chapter four. Due to the low linewidth enhancement factor and large damping, QD laser shows a relative intensity noise (RIN) value less than -150 dB/Hz. The modulation efficiencies and K factor are calculated based on the RIN spectrum under different injection current. Then, the small signal response of 200 and 600 μm length QD laser are measured. The 3 dB bandwidth was mainly limited by the electrical constant with a relatively low value around 5 GHz.

It is found that above -14 dB reflection, the chaotic behavior which could be regarded as the onset of coherence collapse regime. Under feedback ratio above -14 dB, the impact of optical reflection on optical/electrical spectra and small signal modulation is obvious. The excellent feedback-resistant performance of the QD laser can be attributed to the low linewidth enhancement factor (LEF) and strong relaxation oscillation damping.

Finally, the large signal modulation is provided. A clear open eye with extinction ratio above 3 dB is exhibited from 5 Gbps up to 30 Gbps. This large digital modulation speed compared with the predicted intrinsic bandwidth is postulated due to the combination of large value and nonlinearity of the gain in QD. For the large signal application, the stable performance under 10 Gbps modulation with -8 dB feedback is exhibited. It is verified that although the critical feedback level is estimated of -14 dB by the static and small signal performances, in the real applications, the feedback tolerance of QD laser is much higher. We also further push the large signal modulation up to 25 Gbps, and the extinction ratio (ER) of the eye diagram is degraded while the chaotic

oscillation exists especially in the upper level.

6.2 Future work

With continuously increasing bandwidth demand between the server ranks and switches in data centres, Si photonics transmitter has been considered as a key enabling technology to meet the requirements of high-speed connectivity [1]. Its exponentially scaling have been achieved by increasing the bitrate and number of physical lane per package [2]. Based on our measurements and results, we will discuss the improvements in both QD lasers and transmitters.

Firstly, we have achieved low threshold, high temperature stable, low noise and feedback insensitive QD lasers. However, QD lasers have not fulfilled the initial expectation of the large modulation bandwidth. Several physical mechanisms which mainly affect the small signal response are proposed in previous research: carrier capture from the wetting layer, slow relaxation results from the state filling effects, limited differential gain and large gain compression [3-5]. It is pointed out in [6] that although hole spreading and carrier hopping in QD have adverse effects on the differential gain and gain compression, their impact on the modulation bandwidth is not significantly or only for a relatively small range. The ultimate limiting factor is the intra-dot relaxation, which determines both the differential gain and gain saturation, and tunneling injection is considered as one of the possible routes. Another answer is the reduction of inhomogeneous broadening in QD, which leads to increasement in relaxation oscillation frequency without higher damping rate.

With the laser on native substrate providing promising performance in static, dynamic and feedback sensitivity, we could further focus on the photonic integrated circuit on Si by direct epitaxial. The monolithic method offers advantages of substantial manufacturing cost and scalability, while the main challenge is the introduction of crystalline defect that will limit the device quality and reliability. QD is given as a solution due to its discrete density of states and unique electrical confinement. With the well-performed separate devices including lasers, amplifiers, modulators and photodetectors based on QD structure achieved, integration is the next step.

From the module aspect, the scaling of the bandwidth of switch and electrical channel are not at the same rate as shown in Figure 6.1. Moreover, with the increasing electrical line speed, the loss in channel scales resulted in a significant increase in power consumption [7].
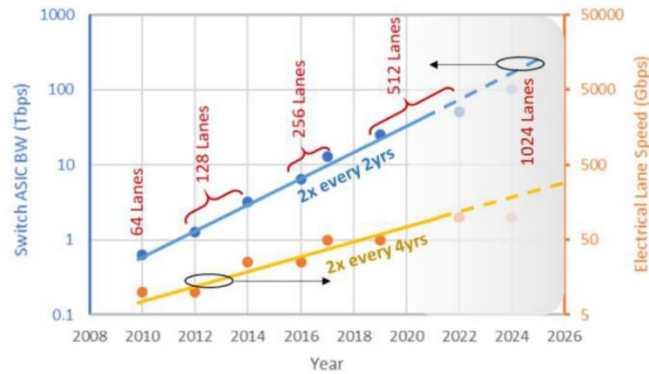

Figure 6.1:Progression of switch and electrical bandwidth[8].

One of the solutions is co-packaging the optics with the switch over low loss electrical channels [9, 10]. The next generation switch is estimated to have 106 Gb/lane electrical interfaces and requires the connection between copper cables to optical transceiver modules at the faceplate. In the co-packaged architecture, highly integrated dense optical modules replace the original front plate pluggable module. Co-packaged optical transceivers and switch application specific integrated circuit (ASIC) share a single organic package with a limited footprint. As a result, the electrical interface power consumption is reduced by bringing optical transceivers inside the chassis closer to processors. In [8], the fully integrated 1.6 Tbps silicon photonics integrated transmitter with co-packaged optics is demonstrated [8, 9]. It consists of sixteen 1310 nm centred optical channels compliant with DR4 IEEE wavelength grid. The co-packaging technique brings the challenges of package size, bandwidth density, energy consumption and reliability to optical transceivers.

Reference

1.   Chang, F., *Datacenter Connectivity Technologies: Principles and Practice*. 2018: River Publishers.

2.   Kuchta, D., et al. *Multi-wavelength optical transceivers integrated on node (MOTION)*. in *2019 Optical Fiber Communications Conference and Exhibition (OFC)*. 2019. IEEE.

3.   Uskov, A., et al., *Theory of a self-assembled quantum-dot semiconductor laser with Auger carrier capture: quantum efficiency and nonlinear gain*. Applied physics letters, 1998. **73**(11): p. 1499-1501.

4.   Ishida, M., et al., *Photon lifetime dependence of modulation efficiency and K factor in 1.3μm self-assembled InAs∕GaAs quantum-dot lasers: Impact of capture time and maximum modal gain on modulation bandwidth*. Applied Physics Letters, 2004. **85**(18): p. 4145-4147.

5.   Markus, A. and A. Fiore, *Modeling carrier dynamics in quantum-dot lasers*. physica status solidi (a), 2004. **201**(2): p. 338-344.

6.   Fiore, A. and A. Markus, *Differential Gain and Gain Compression in Quantum-Dot Lasers*. IEEE Journal of Quantum Electronics, 2007. **43**(4): p. 287-294.

7.   Liu, C., *Options for copper beyond 112 Gbps*. Signal Integrity Journal, August, 2020.

8.   Fathololoumi, S., et al., *1.6 Tbps Silicon Photonics Integrated Circuit and 800 Gbps Photonic Engine for Switch Co-Packaging Demonstration*. Journal of Lightwave Technology, 2021. **39**(4): p. 1155-1161.

9.   Fathololoumi, S., et al. *1.6 Tbps silicon photonics integrated circuit for co-packaged optical-IO switch applications*. in *Optical Fiber Communication Conference*. 2020. Optical Society of America.

10.   Minkenberg, C., N. Kucharewski, and G. Rodriguez, *Network architecture in the Era of integrated optics*. Journal of Optical Communications and Networking, 2019. **11**(1): p. A72-A83.